The Dissertation Committee for Igal Bucay
certifies that this is the approved version of the following dissertation:

Surface Ionization of Metastable Calcium and Ytterbium Atoms

Committee:

Mark Raizen, Supervisor

Alex de Lozanne

Sonia Paban

Greg Sitz

SV Sreenivasan

Surface Ionization of Metastable Calcium and Ytterbium Atoms

by

Igal Bucay

DISSERTATION

Presented to the Faculty of the Graduate School of
The University of Texas at Austin
in Partial Fulfillment
of the Requirements
for the Degree of

DOCTOR OF PHILOSOPHY

THE UNIVERSITY OF TEXAS AT AUSTIN
August 2019

Acknowledgments

I have many people to thank for the work outlined in this dissertation and for the support they have given me throughout my time in graduate school. First, I must thank my advisor, Mark Raizen. When I was selecting a graduate school, it was my initial meeting with Mark and his research group in February of 2015 that motivated me to attend UT Austin. I was riveted by Mark's passion for science and his pursuit of novel research projects with compelling applications. I admire Mark's willingness to engage in challenging and interdisciplinary experiments with meaningful applications. Nonetheless, major reasons that also piqued my interest in Mark's group were his relationship with his students, his reliable communication skills, and his vested interest in the success of his students. Throughout my time in Mark's group, I routinely benefited from our frequent interactions. Many times throughout the past few years, I had somehow managed to convince myself that the experiment I was working on was in some way doomed to fail. However, Mark always managed to bring me back to reality while noting that it would hardly be scientific research if we implemented an experiment that was practically guaranteed to succeed. Without fail, I left our meetings more motivated and excited about our research project. Lastly, I commend Mark for his non-academic and humanitarian endeavors, namely The Pointsman Foundation, which aims to provide enriched isotopes for medical applications. I am grateful for the opportunity I had to pursue my graduate studies with Mark as my advisor and to work in a group filled with outstanding people and remarkable scientists.

When I joined Mark's group, I was initially paired with Georgios Stratis[1]. A fermented foods and olive oil aficionado, Georgios hails from the land of Cyprus, where all things are great, or so I have been told. During my first year of graduate school, Georgios and I worked together on a project aimed at developing a novel spectroscopic tool using metastable noble gas atoms to complement an atomic beam focusing effort spearheaded by Erik Anciaux, Jamie Gardner, and Rodrigo Castillo-Garza. I would wager to say that my pairing with Georgios was perhaps one of the most fortunate things to have happened to me throughout graduate school, and not because of the seemingly endless stream of free Greek language and Cyprus factoids. Georgios and I shared an office, worked on the same optical table, and frequently detoxed from moments of frustration and despair over lunch. Even though I began to work on a different experiment (that is, the one outlined in this dissertation) within a year, Georgios became a great friend and remained a steadfast system of support for my subsequent years in graduate school, particularly since Memorial Day of 2015. I have a monumental amount of respect for Georgios for he is working on one of the most challenging experiments in the lab and has been doing so with a prodigious degree of resilience and determination – a feat which I think few others (certainly including myself) could accomplish considering how, for a number of years, Georgios was engaged in this project independently and some of the equipment at his disposal is simultaneously poorly documented and intensely sophisticated. Georgios has succeeded in teaching himself an outsized

---

[1] It is pronounced ʝeòrɣios straːtis and you must never forget it!

amount of information and skills and has demonstrated an aptitude for engaging in technological problems with a thoroughly analytical approach. Outside of the lab, Georgios has also participated in a number of commendable efforts. For three years, Georgios was one of the few people sincerely committed to improving the experience of students within the graduate program of the physics department at UT Austin as a representative on the graduate wellfare committee. In the recent years, he expanded this effort as a founding member of Underpaid at UT, a university-wide effort to improve conditions for graduate student workers. Georgios is also an active participant in the Texas Prison Education Initiative. Since meeting him, Georgios has repeatedly proven to be an outstanding researcher in the lab and a formidable member of the community.

After working with Georgios, I began a research project on an ionization mechanism known as field ionization with David Dunsky, a truly extraordinary scientist and human being in every regard. It was an absolute honor for me to have had the opportunity to work with David – he is highly motivated and skilled researcher with an exceptional aptitude for experimental and theoretical physics. At the time, I was a second-year graduate student and David was a senior undergraduate. By convention, one would expect information and training to flow top-down, that is, from the graduate student to the undergraduate. However, this convention was largely blurred when I worked with David as I often found myself learning a substantial amount of information from him. Despite being an exceptionally proficient experimental physicist, David ultimately pursued his graduate studies in theoretical physics at UC Berkeley, applying his expertise to theories beyond the Standard Model. I am confident that David will succeed in any task or challenge he undertakes and his current and future coworkers are fortunate to have him. I also enjoyed many discussions with David concerning books he has read and I am grateful to him for resuscitating my interests in reading.

For the entirety of the ytterbium experiment, I had the great fortune to work with Lukas Gradl. Lukas began in the lab by working on "the slower project," a large research endeavor intending to ultimately demonstrate a more general cooling method than laser cooling in order to attain higher fluxes and densities of cold atoms. Since we began working together, I came to admire Lukas's integrity and diligence. Through seemingly endless attempts of igniting the ytterbium discharge, Lukas remained relentlessly focused and motivated. His attitude was persistently optimistic and level headed, even after the nth time we were forced to break vacuum and extract the oven from the chamber in a single week. Lukas's uncanny ability to systematically troubleshoot a problem, in conjunction with his mastery of the minutiae of experimental physics, made him an incredibly auspicious lab partner and I am very grateful for having had the opportunity to work with him.

There are two post-docs with whom I worked closely in graduate school: Rodrigo Castillo-Garza and Ahmed Helal. Rodrigo supervised the focusing and metastable atom spectroscopy projects and infused the lab with an atmosphere of optimism, kindness, and ambition. I am grateful to Rodrigo for training me in various aspects of experimental atomic physics research, particularly in vacuum science. I would also like to thank Ahmed for several contributions to the surface ionization experiment, namely the calibration of the photomultiplier we used for quantifying the fluorescence of the calcium discharge, the setup of the initial ECDL and optical system for pumping a transition in calcium, as well as an abundance of helpful technical and scientific input.

For about four years of graduate school, my desk was next to that of Erik Anciaux. A Youtube connoisseur, Erik has a remarkable ability to elucidate most life occurrences and milestones with a simple video clip from the internet. Although it is difficult to say with certainty whether Erik speaks exclusively or only partially in puns and movie references, I can confidently say that due to his being a quick learner and an intensely diligent worker, Erik reached many milestones during graduate school. Erik worked on the focusing project largely with Jamie Gardner and together they accomplished many breakthroughs pertaining to the brightening and focusing supersonic atom beams. I am grateful to Erik and Jamie for fostering a pleasant work environment in our office and for providing me with a surplus of valuable scientific input and for training me on various experimental techniques, such as locking a laser, leak testing, and machining, to name a few.

Over the past few years, I have shared my office space and many thought-provoking conversations with Jordan Zesch. Jordan, a self-styled “coding god”, has had the opportunity to participate in most of the experiments in the lab and has recently made extensive contributions to the microscope project. I greatly admire Jordan for his reflective and contemplative nature as well as his uniquely deferential approach in regard to various discussions – even when finding himself in stark disagreement with other parties, Jordan is readily able to maintain his composure in instances where many others would react emotionally. I am grateful to Jordan for many impressive games of ‘nanas and book recommendations.

Kevin Melin, Yu Lu, Logan Hillberry, Yi Xu, Pavel Nagornykh, and Harry Ha, and previously including Karl Burkhardt and Isaac Chavez, worked on the slower project and were each an incredibly valuable and impressive resource. I am in awe of Kevin’s seemingly endless list of skills and the high standard of quality with which he approached all tasks; additionally, he has been a particularly valuable asset for knowing the location of virtually every item in the lab. Yu was the only other person to join our lab from my class and, being an incredibly hardworking individual, he managed to develop a profundity of skills in data science in scientific computation outside of the lab, in addition to finishing his Ph.D. in record time. Logan and Yi did inspiring work on the slower project and have recently made major contributions to the tweezer project with Diney Ether. Logan and Yi are both remarkably motivated and inspiring researchers. I am amazed by the high quality of their work as well as the extensive breadth and depth of their physics knowledge. Harry and Pavel were both post-docs who brought an extensive range of knowledge and skill to the lab and were both very helpful.

Diney Ether joined the group nearly a year ago and has been a pillar of positivity, optimism, and kindness. During moments of frustration in the lab, Diney was uniquely understanding and a very helpful resource. He is currently supervising the tweezer experiment where he brings a versatile skill set in experimental and theoretical physics and has quickly become an asset to the lab. I have tremendous respect for the thoroughness and thoughtfulness with which Diney approaches research and life in general. Diney, Logan, and Yi constitute an incredibly talented team and will surely have many major accomplishments. I am grateful for the time Diney and I shared in the lab and I am confident he will become a formidable and outstanding professor.

I have also had the good fortune to overlap with many other talented graduate students. Jianyong Mo worked for many years on the Brownian motion experiment and lastly on the slower project and approached all of his work with a commendable degree of rigor. Jianyong was a very helpful coworker and I am grateful for his commitment to thoroughly help anyone seeking his assistance. Karl Burkhardt joined the lab in the same year as me and quickly became a very helpful resource, particularly in chemistry. Though we only overlapped briefly, Isaac Chavez, Tom Mazur, and Simon Kheifets made substantial progress on different experiments and, in doing so, set a very high standard of quality for the rest of us.

In addition to the remarkable graduate students and post-docs that I am fortunate to have worked with, I also overlapped with many extraordinary undergraduate students. Zoe de Beurs is an incredibly talented researcher who made significant contributions to the focusing and microscope experiments. Julia Orenstein and Gabe Alvarez worked concurrently on the Brownian motion experiment and managed to learn vast ranges of information and skill remarkably quickly. Recently, Sebastian Miki-Silva has brought an insatiable enthusiasm and commendable work ethic and integrity to the lab.

Throughout graduate school, I received bountiful assistance from Olga Vera, whose understanding of the university bureaucracy and policies is unmatched. I am grateful for our many discussions and the patience with which Olga reminded me to fill out my paperwork every semester.

I must also voice my appreciation and admiration for the machine shop staff, without whom most of the work we wish to do in the lab would be impossible. Allan Schroeder, the machine shop supervisor, never turned any of us away and, regardless of the convoluted designs we submitted, always managed to create what we had in mind. Each of the machinists built a part for my experiment at some point and I found the exceptional quality of their work to be both refreshing and inspiring. I am also grateful for Ed Baez for leak-testing all of my vacuum equipment and servicing countless rouging pumps, as well as for Robert Hasdorff for his assistance regarding electronics. Additionally, Jack Clifford, the supervisor of the student machine shop, has been an incredible teacher to me over the years and I am indebted to him for the help he has provided me in machining parts and improving designs. I have enjoyed talking with Jack about woodworking, traveling, and cooking.

I am immensely grateful to all of the aforementioned people for fostering a pleasant work environment for me in the lab and the machine shop throughout my time in graduate school. I have an immense amount of respect for all them and I am very appreciative of all of the information they have given me and all of the skills they have taught me.

Finally, I thank my parents, my sister, and Brooke for all of their endless love and support, without which I would not be where I am today. All of my work throughout graduate school and in writing this dissertation was aimed at accomplishing something worthy of their esteem.

Surface Ionization of Metastable Calcium and Ytterbium Atoms

Publication No. ___________________

Igal Bucay, Ph.D.
The University of Texas at Austin, 2019

Supervisor: Mark Raizen

This dissertation presents an experiment demonstrating the surface ionization of metastable atoms on a tungsten surface. Surface ionization refers to the thermionic ionization of adsorbates with low ionization potentials on hot, high-work function metal surfaces. The efficiency of surface ionization is exponentially dependent on the difference between the atom ionization energy and the surface work function. Since the work functions of metals are, at most, $\sim 6\,\text{eV}$, surface ionization is limited to elements with low ionization energies and is frequency exploited for detecting alkali and alkaline earth metal beams.

We use an electric discharge to excite a fraction of atoms in separate calcium and ytterbium beams to metastable states. In doing so, we effectively lower their ionization energy by about $2\,\text{eV}$. On a polycrystalline tungsten surface, with a work function measured to be $5.18\,\text{eV}$, surface ionization is theoretically more likely for metastable calcium and ytterbium atoms than for their ground state counterparts.

However, the elementary theory of surface ionization does not take into account various de-excitation or neutralization processes that may preclude the formation of ions. We report findings that metastable calcium and ytterbium atoms undergo surface ionization at significantly higher rates than corresponding ground state atoms.

Table of Contents

List of Tables

List of Figures

Chapter 1

Introduction

1.1 Efficient ionization on a large scale

Ionization, the process wherein a neutral atom or molecule acquires a charge by gaining or losing electrons, is the underlying process behind a variety of devices used in fundamental science (e.g., mass spectrometry [13], ion beam sources) and industry (e.g., ion pumps, reactive ion plasma etching of semiconductors, ionization chambers for medical radiotherapy dose calibration, ion thrusters for spacecraft propulsion). In this document, ionization will refer solely to the creation of positive ions with a charge $+e$ through the removal of a valence electron of an atom.

Electrons are bound to an atom by the Coulomb potential of the nucleus and the energy required to remove a bound electron is termed the ionization energy of the atom, I, ranging from $3.89\,\mathrm{eV}$ in cesium to $24.59\,\mathrm{eV}$ in helium. This energy may be supplied to the atom through inelastic interactions with other particles (i.e., subatomic particles or other atoms or ions), through the absorption of a photon, or through the suppression of the Coulomb barrier of an atom by an external electric field. Here, the general properties of four principal ionization mechanisms will be considered (the latter two of which are the focus of this document): **a)** electron impact ionization, **b)** photoionization, **c)** surface ionization, and **d)** field ionization. As will be addressed in Section 1.2, two particular properties of interest regarding the aforementioned processes are *efficiency* (i.e., the percentage of target atoms which can be deliberately ionized) and *scalability* (i.e., the potential to implement an ionization method on an arbitrarily large scale, barring extrinsic limitations). *Selectivity* (i.e., between different atomic species or different isotopes) and *universality* (i.e., applicability to different atomic species) will also be addressed.

Electron impact ionization A free electron inelastically collides with a target atom and converts it to a positive ion:

$$\mathrm{A} + e^- \rightarrow \mathrm{A}^+ + 2e^-. \tag{1.1}$$

For a free electron with energy E_e, upon impact with an atom, elastic scattering is always a viable collision pathway. Every excited state in the atom of energy $E_{\mathrm{ex}} < E_e$ constitutes a possible pathway for an inelastic collision. Likewise, for $E_e > I$, ionization becomes possible, at which point the total collision cross section consists of contributions from elastic, excitation, and ionization cross sections:

$$\sigma_{\mathrm{tot}} = \sigma_{\mathrm{el}} + \sigma_{\mathrm{ex}} + \sigma_I. \tag{1.2}$$

The ionization cross section, σ_I, is typically on the order of $\sim 1 \times 10^{-16}\,\mathrm{cm}^2$. The electron energy dependence of the ionization cross section is approximately [14]

$$\sigma_I \propto \begin{cases} \frac{E_e}{I} - 1 & E_e \approx I \\ \frac{\ln E_e}{E_e} & E_e \gg I \end{cases}$$

The current of ions, I^+, produced is proportional to the ionization cross section [15]:

$$I^+ = nl\sigma_I I_e, \tag{1.3}$$

where $n = \frac{P}{k_B T}$ is the number density of target atoms, l is the ionizing pathlength, and I_e is the incident electron current. Eq. 1.3 is a valid simplification of an expression analogous to the Beer-Lambert Law since $nl\sigma_I \sim 10^{-3}$ [16].

There is no fundamental limitation on the scale over which one may implement electron impact ionization: an atomic or molecular beam of arbitrary size can be fractionally ionized by an appropriate electron beam of sufficient current and energy. The electron source is conventionally a thermionic (hot cathode) or field electron (cold cathode) source with an output electron current that can be easily modulated by varying the filament temperature or source extraction voltage, respectively. The efficiency of electron impact ionization is predominately limited by the small magnitude of the ionization cross section. Furthermore, the outcome of an electron-atom collision can never be exclusively ionization due to the finite elastic scattering and excitation cross sections. The ionizing pathlength may be enhanced by incorporating a magnetic field to impel the electrons on a spiral path but the electron current must be kept sufficiently low in order to preclude space charge repulsion effects. Lastly, when an electron undergoes an ionizing collision, the incident electron loses approximately 30 eV of its energy [17], thereby changing the electron energy distribution. Doing so changes the relative contributions of different collision cross sections in Eq. 1.2. Over a long ionization pathlength, or at high pressures, this distortion of the electron energy distribution will affect the ionization efficiency, unless the target atom density can be kept sufficiently low to guarantee conditions for single collisions [18, 19].

Photoionization Photoionization is a very broad term encompassing various distinct processes governing the ionization of atoms or molecules when interacting with electromagnetic radiation. We can distinguish between different photoionization regimes with the Keldysh parameter (in atomic units) [20]

$$\gamma = \frac{\omega\sqrt{2I}}{F_0}, \tag{1.4}$$

where I is the ionization energy of the atom subject to a laser field with frequency ω and field strength F_0. Low intensity, high frequency photoionization processes, $\gamma > 1$, are referred to as multiphoton ionization (MPI). High intensity, low frequency processes, $\gamma < 1$, are dominated by the electric field strength of the laser field – these field-effect photoionization processes include tunnel ionization and over the barrier ionization.

MPI phenomena describe the ionization of an atom A following the absorption of n photons

$$\mathrm{A} + n \cdot \hbar\omega \rightarrow \mathrm{A}^+ + e^-.$$

MPI can proceed through resonant or non-resonant excitation of atoms in a stepwise fashion from the ground state to the continuum, as shown for a two-step scheme in Figure 1.1a. The kinetics for such a photoionization scheme are governed by the following simple rate equations (assuming equal multiplicities in the ground and excited states for simplicity) [21]:

$$\begin{aligned}
\frac{dN_1}{dt} &= -\alpha_{12}(N_1 - N_2) + \frac{1}{\tau_{12}}N_2, & N_1|_{t=0} &= N_0, \\
\frac{dN_2}{dt} &= \alpha_{12}(N_1 - N_2) - \alpha_i N_2 - \frac{1}{\tau_{12}}N_2, & N_2|_{t=0} &= 0, \\
\frac{dN_i}{dt} &= \alpha_i N_2.
\end{aligned}$$

Here, N_1 is the number density in the ground state 1, N_2 is the number density in the excited state 2, N_i is the ion density, α_i and α_{12} are absorption rates, and $1/\tau_{12}$ is the relaxaction rate of the excited atoms. Naturally, these equations would need to be expanded to consider the degeneracy of atomic states and the atomic velocity distribution within the laser field. According to these rate equations, in order to ionize the target atoms efficiently and effectively, all relevant atomic transitions would have to be simultaneously saturated. For the two-step system above, for example, assuming a negligible relaxation of excited atomic states (i.e., $\alpha_{12}, \alpha_i \gg 1/\tau_{12}$), the intensity of the ionizing laser $\mathcal{I}_2$ must be substantially higher than that of the excitation laser $\mathcal{I}_1$:

$$\mathcal{I}_2 = \left(2\frac{\sigma_{12}}{\sigma_i}\right)\mathcal{I}_1,$$

where σ_{12} is the excitation cross section and σ_i is the ionization cross section.

In the regime of a low Keldysh parameter, $\gamma < 1$, the electric field strength of the laser field is sufficiently high to distort the Coulomb potential of the atom, thereby creating a finite potential barrier, through which the valence electron can tunnel out, as shown in Figure 1.1b [22, 23]. With increasing laser intensities, the height and width of the Coulomb barrier will be further reduced until it is

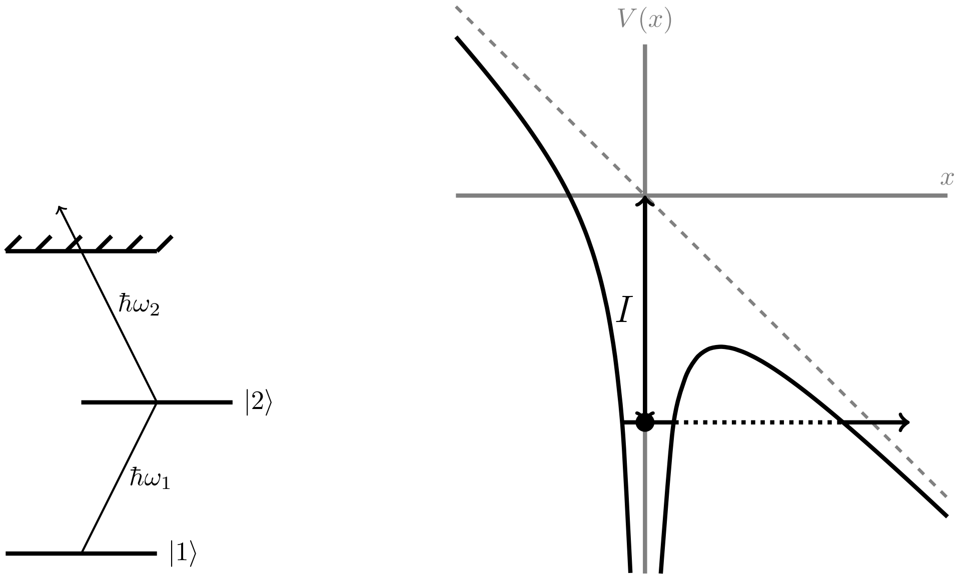

(a) Multiphoton ionization (b) Tunneling ionization

Figure 1.1

completely suppressed by the electric field such that the ground state is no longer bound to the atom [24].

Regarding the criteria of interest to us, namely efficiency and scalability, photoionization processes are undoubtedly efficient – under appropriate conditions, atoms may even undergo multiple ionization events [25]. However, it is when we consider performing any particular photoionization process on a large scale that we may encounter major drawbacks. To fulfill the aforementioned criteria for MPI or tunneling ionization, it is necessary to employ either multiple lasers [26] or attain very high intensities [27, 28], often in excess of 10^{10} W/cm^2.

Surface ionization Atoms are spontaneously ionized upon desorption from a hot, high work function metal surface and is often characterized by two quantities, α and β, which represent the fraction of atoms that are ionized and the ionization efficiency, respectively. The degree of ionization is given by the Saha-Langmuir Equation [29], which is derived in Section 1:

$$\alpha = \frac{n_i}{n_0} = \frac{g_i}{g_0} e^{-(I-\Phi)/k_B T}, \tag{1.5}$$

where n_i is the flux of surface ions emitted from the surface, n_0 is the flux of neutrals that do not undergo surface ionization, g_0 and g_i are the statistical weights of the atomic and first ionic ground states (given by $[2J+1]$ or $[(2L+1)(2S+1)]$ depending on how the thermal energy, $k_B T$, of the ionizing surface compares to the energy of the fine-structure splitting of the atom/ion), I is the ionization potential of the atom, and Φ is the work function of the metal surface, which is heated to a temperature of T. A conventional potential energy diagram depicting surface ionization is shown in Figure 1.2a. If the conditions are appropriate for surface ionization, a valence electron in the adsorbed atom will tunnel into an unoccupied state in the metal surface.

The ionization efficiency, β is defined as the ratio of ions emitted from the surface, n_i, to the total flux of atoms incident on the surface $n = n_i + n_0$ [30, 31]:

$$\beta = \frac{n_i}{n} = \frac{\alpha}{1+\alpha}. \tag{1.6}$$

Evidently, for $I \gg \Phi$, $\alpha \ll 1$ and the efficiency of surface ionization is low, $\beta \approx \alpha$, and if $I \gtrsim \Phi$, then $\alpha \gg 1$ and the efficiency will approach 100%, $\beta \approx 1$.

The metal materials typically chosen for this thermal ionization process are refractory metals (e.g., W, Re, Ta, Mo) as they have high work functions, can be operated at high temperatures, are mechanically robust, and are easily resistively heated. The versatility of surface ionization is limited for two reasons. First, the work functions of refractory metals are typically $4.5 - 5\,\mathrm{eV}$ and can be as high as $6\,\mathrm{eV}$ when optimally oxidized. Second, the ionization efficiency of surface ionization is exponentially dependent on the difference $I - \Phi$. For these reasons, surface ionization is far from a universal ionization mechanism and is largely restricted to atomic species with relatively low ionization potentials (i.e., alkali metals). The surface ionization of ground state alkali atoms can reach efficiencies as high as 100% for a system such as cesium on tungsten [29]. For this reason, surface ionization is routinely exploited in atomic physics research in a hot-wire or Langmuir-Taylor detector for the detection of alkali metal beams.

A single refractory metal wire is what is typically used in surface ionization but there is no fundamental reason why one must be restricted to a thin wire. As long as uniform high temperatures can be attained throughout the ionizing surface, it is straightforward to implement surface ionization along a wide ribbon or metal plate.

The selectivity of surface ionization is largely determined by the relationship between the atomic ionization potential and the work function of the metal surface. Atoms with $I < \Phi$ will be ionized with unity efficiency, whereas atoms with $I > \Phi$ will by ionized at a rate strongly dependent on the temperature, according to Equation 1.5. Effectively, the selectivity of surface ionization is strong only for elements with a difference in ionization energy that exceeds 1 eV. Therefore, when considering ground state atoms, it is not possible to distinguish between different isotopes of a particular element during the surface ionization process. In Chapter 5, I outline an approach to enhancing the selectivity of surface ionization, one that may be applied in an isotope enrichment scheme.

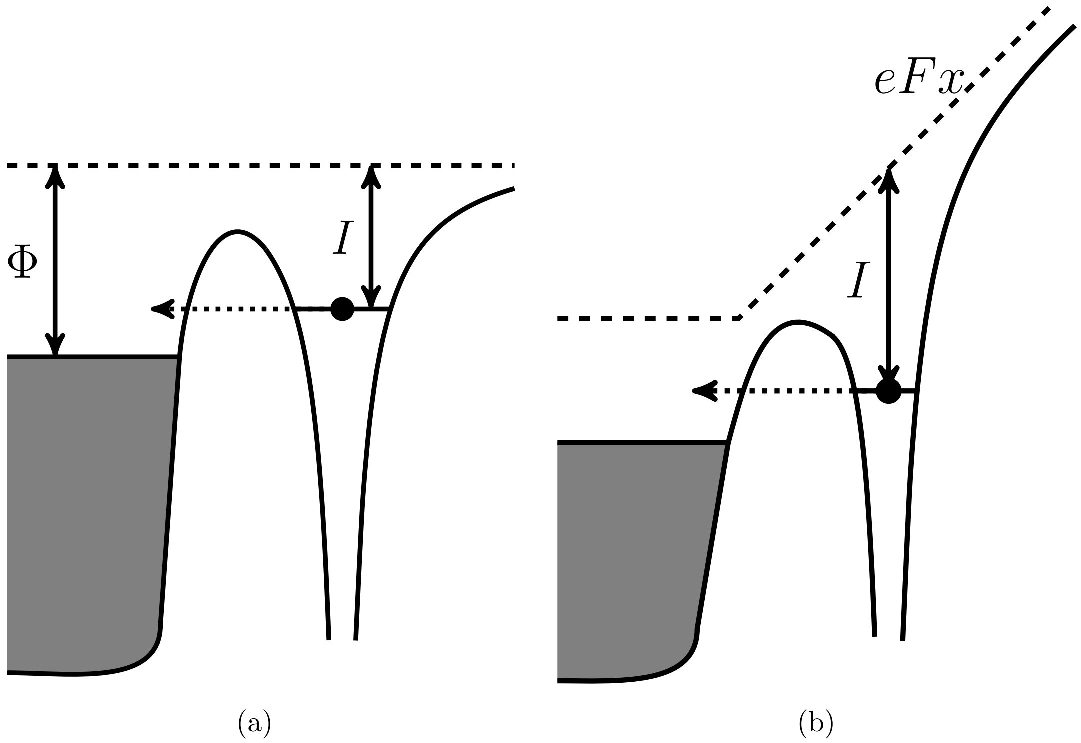

(a) (b)

Figure 1.2: Potential energy diagrams for (a) surface ionization and (b) field ionization. The probability of surface ionization increases exponentially with the difference $I - \Phi$. Fields on the order of $F \gtrsim 10^9$ V/m enable field ionization when $I > \Phi$.

Field ionization Field ionization is a quantum tunnelling phenomenon wherein an atom is ionized by an external DC electric field in excess of 10^9 V/m. The external field suppresses the Coulomb potential of the atom, as shown in Figure 1.2b. Realizing DC fields of this magnitude between any two electrodes is nontrivial – the onset of electrical breakdown of the gas between the electrodes corresponds to the dielectric strength of the medium and typically occurs at fields on the order of 10^6 V/m [32, 33, 34, 35]. Even for conditions where gas breakdown is not an issue, the onset of field emission of electrons from the cathode may occur for fields as low as 10^8 V/m [36, 37, 38]. Evidently, multiple mechanisms of charge flow between the electrodes present significant obstacles that must be circumvented in order to reach the 10^9 V/m threshold for field ionization.

Therefore, field ionization may only occur locally in a restricted volume while maintaining unfavorable conditions for other charge flow mechanisms in the bulk electric field. This is precisely what occurs in conventional DC field ionization sources: the geometric enhancement of electric fields in the vicinity of sharp structures is exploited to produce electric fields exceeding 10^9 V/m over a small volume. In such field ionization sources, the anode consists of a microstructure with an aspect ratio greater than 1000 (i.e., a tip radius of $\sim 10\,\mathrm{nm}$ and a length of $\sim 10\,\mu\mathrm{m}$) that is biased to $\sim 1\,\mathrm{kV}$ and adequately insulated over a distance of $\sim 100\,\mu\mathrm{m}$ from a grounded cathode (e.g., a fine metallic mesh) [39]. Under such conditions, the enhanced electric field is sufficiently strong for field ionization over a volume that is only $\approx 10\,\mathrm{\AA}^2$ in diameter and $\approx 0.1\,\mathrm{\AA}$ thick and some distance away from the sharp structure [40, 41]. The efficiency of ionization of atoms that pass through this volume is essentially 100%, which is significantly greater than the $10^{-2} - 10^{-4}$ ionization probability of electron impact. As an added benefit for mass spectrometry, unlike electron impact ionization, field ionization largely produces the parent ion of a molecule and few, if any, fragments are observed [42]. Regarding selectivity and universality, the former can be straightforwardly enhanced by implementing an optical pumping scheme to excite gaseous particles, thereby lowering their ionization energy. As for the latter, considering how field ionization has been repeatedly performed on helium [39, 43, 44, 45], field ionizing any other atomic species is feasible, provided that the anode can withstand the temperatures required to evaporate adsorbates (i.e., metallic adsorbates) that are not initially pulled in to the tip.

Despite the minuscule volume of the ionization zone described above, the actual collection area is considerably larger since neutral atoms may be polarized and attracted to the tip [44, 9, 45]. Nonetheless, realizing field ionization on a significantly larger scale requires arrays of sharp structures with dimensions comparable to those described above. Such arrays inevitably introduce several complications. First, fabricating arrays of identical and uniformly distributed nanostructures is nontrivial. It is naturally simpler to forgo order for fabrication expediency, but doing so comes at a cost: in arrays of disorderly carbon nanotubes or silicon nanowires, for example, select structures with abnormally large aspect ratios or those on the periphery of the array will disproportionately contribute to the ion current [39, 46]. Fabricating arrays with optimized order and uniformity requires substantially more control over relevant experimental parameters. Second, introducing additional field ion emitters imposes a restriction on the pitch, the lateral distance between adjacent structures. Neighboring nanostructures capacitively screen each other's enhanced electric fields, an effect which is inversely proportional to the pitch. Consequently, a compromise must be made between the field screening effect and nanowire density when performing field ionization on a large scale.

1.2 Motivation and overview

Originally, the long term goal of this experiment was to develop a novel method of isotope enrichment that did not fundamentally rely on small differences in the charge-to-mass ratio of different isotopes in order to address the various disadvantages of the calutron, one of the most prolific means of enriching isotopes to date [47]. This effort would complement earlier work done in our group by Tom Mazur, who demonstrated the feasibility of enriching isotopes of lithium by polarizing atoms of a particular isotope into specific magnetic states through optical pumping and subsequently guiding them towards a collector.

Our plan for achieving isotopic selectivity consisted of optically pumping atoms of the target isotope to a long lived excited state and selectively ionizing the excited atoms with an efficient, scalable ionization mechanism. Neither electron impact ionization or the various methods of photoionization are suitable. Ionization by electron impact is characteristically inefficient and one of several disadvantages of the calutron. Photoionization is limited in scale. This inspired us to consider alternative methods of ionization, namely surface and field ionization.

Since the inception of this idea several years ago, our work, which I have outlined in this dissertation, has largely consisted of investigating the mechanisms of surface and field ionization. In the first part, I address our work regarding surface ionization. Chapter 2 summarizes several pertinent principles of surface ionization. In Chapter 3, I summarize the various properties of calcium and ytterbium that make them suitable subjects for investigating the surface ionization of metastable atoms. Chapter 4 provides an overview of the three primary sections of our experimental set-up: a thermal atomic beam source, a DC hollow cathode discharge for populating the metastable states of calcium and ytterbium, and a surface ionization detector. Chapter 5 presents the results of our surface ionization experiment, demonstrating that metastable calcium and ytterbium atoms can be preferentially ionized over their ground state counterparts. Lastly, in Chapter 6, I present some of our current work concerning an optical system for calcium to replace our hollow cathode discharge as a means of populating the metastable state and rigorously quantifying the efficiency of metastable atom surface ionization.

Chapter 2

Principles of Surface Ionization

Surface ionization is the second step in a three-step process outlining the interactions between gaseous particles, A, impinging on an incandescent metal surface [48]:

1. Adsorption: $A_{\mathrm{g}} \leftrightharpoons A_{\mathrm{ads}}$
2. Ionization: $A_{\mathrm{ads}} \leftrightharpoons A^{+}_{\mathrm{ads}} + e^{-}$
3. Desorption: $A^{+}_{\mathrm{ads}} \rightarrow A^{+}_{\mathrm{g}}$

where g denotes a gas-phase particle and ads denotes an adsorbed species (adsorbed atoms are also referred to as adatoms and adsorbed ions as adions). Once adsorbed on a hot metal surface, some fraction of the particles will evaporate as neutral atoms while some fraction may evaporate as positive or negative ions after some average residence time τ_a or τ_i, which differs for atoms and ions, respectively. Hereafter, surface ionization will refer exclusively to the formation of positive ions.

We next analyze the second step, surface ionization, in more detail. As an atom approaches a metal surface, the atomic level of its valence electron is progressively perturbed, broadening into a band as it couples with the Fermi sea of electrons in the metal surface as shown in Figure 2.1 [30, 49, 50, 51, 52, 53]. This broadening results in a finite lifetime of the atomic state and the width of the broadened atomic level (can be as high as $\sim 1\,\mathrm{eV}$ for alkali atoms on tungsten [54]) corresponds to the rate of charge transfer between the atom and surface. For alkali atoms on free-electron metal surfaces, this width varies nearly exponentially with the distance to the surface [50].

At distances from the metal surface sufficiently small for broadening of the valence level to occur, the occupation probability of the valence level of the adatom (adsorbed atom) can be predicted by Fermi-Dirac statistics [55]. Consequently, the probability of occupation for the valence level, E_x, is [49]

$$P_a = P(E_x) = \left(1 + \frac{g_i}{g_a} e^{(E_x - E_F)/k_B T}\right)^{-1}, \tag{2.1}$$

where $g_{i,a}$ are the statistical weights of the ion and atom and E_F is the Fermi level of the surface. Likewise, the probability that this level is vacant (i.e., that the atom is ionized) is

$$P_i = 1 - P(E_x). \tag{2.2}$$

The degree of charge transfer for the adatom is given by

$$\frac{P_i}{P_a} = \frac{g_i}{g_a} \exp\left(\frac{E_x - E_F}{k_B T}\right), \tag{2.3}$$

where $E_x - E_F = \Phi - I_{ads}$ as outlined in [49, 29, 56]. I_{ads} is the ionization energy of the adatom at some distance x_0. Due to the perturbation of the valence level of the adatom as it interacts with the Fermi sea of electrons in the metal, the vacuum ionization energy of the atom I is reduced to I_{ads} by the image potential, $e/4\pi\varepsilon_0 x_0$,

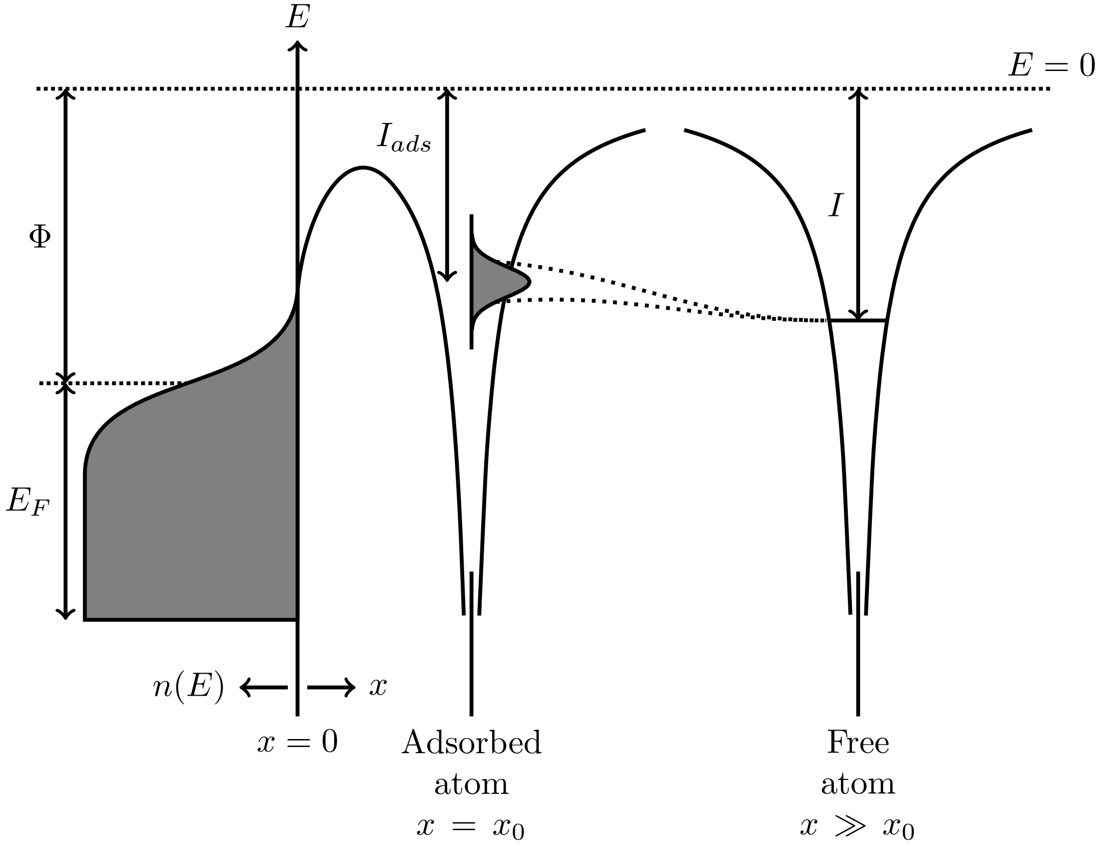

Figure 2.1: Schematic potential energy level diagram for the adsorption of an electropositive atom on a metal surface with work function Φ. The valence level of the adatom is broadened as it interacts with the Fermi sea of electrons in the metal. Should the conditions for surface ionization (i.e., $I \lesssim \Phi$), the valence electron will tunnel through the barrier into an unoccupied electronic state in the metal.

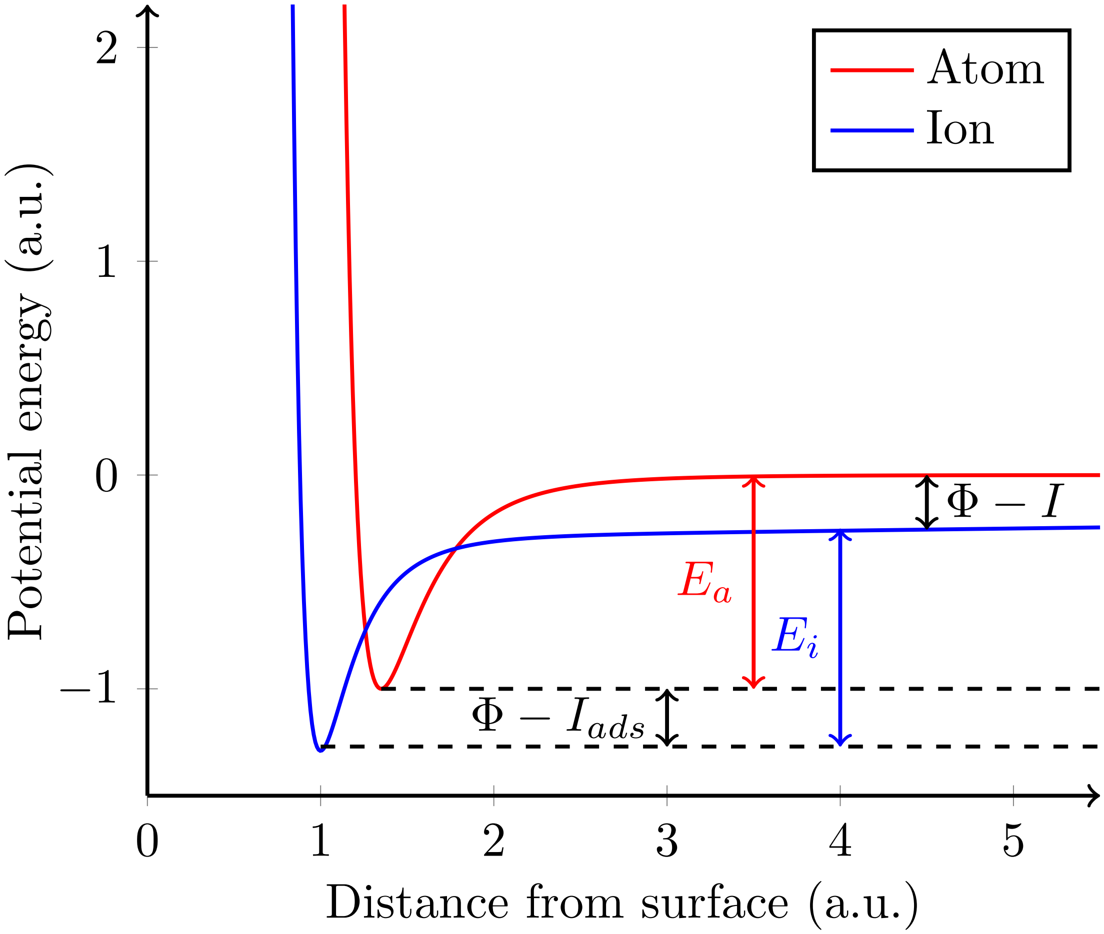

Figure 2.2: Potential energy diagram of an adsorbed atom and ion.

where x_0 is the equilibrium distance of the center of the adatom to the surface [57]. This change in the ionization energy upon adsorption [56] to be equivalent to the ionic and atomic heats of vaporization at equilibrium, E_i and E_a. These arguments allow us to rewrite Equation 2.3, the charge-transfer probability for the adatom, as

$$\frac{P_i}{P_a} = \frac{g_i}{g_a} \exp\left(\frac{E_i - E_a - (I - \Phi)}{k_B T}\right) \tag{2.4}$$

where $I_{ads} = I - (E_i - E_a)$ [58, 59, 60]. Ultimately, we are interested in the degree of ionization, α. This is the ratio of the number of ions to number of neutral atoms evaporated from the surface, which is equivalent to the product of the probability of charge transfer and the probability that the adsorbate will have sufficient kinetic energy to exceed the evaporation energy E_i or E_a.

Frenkel treated each adsorbate as a one-dimensional harmonic oscillator with frequency $\omega_{i,a}$ bound a surface with energy $E_{i,a}$ to express the rate of evaporation as an Arrhenius equation [61, 62, 63]:

$$R(E_{i,a}) = \omega_{i,a} e^{-E_{i,a}/k_B T} = \frac{1}{\tau_{i,a}}, \tag{2.5}$$

Here, $\tau_{i,a}$ is the mean residence time of adsorbed particles on the surface. The product of Equations 2.4 and 2.5 yields the degree of ionization:

$$\alpha = \frac{n_i}{n_a} = \frac{P_i}{P_a}\frac{R(E_i)}{R(E_a)} = \frac{g_i}{g_a}\frac{\omega_i}{\omega_a} e^{-(I-\Phi)/k_B T}, \tag{2.6}$$

This equation is referred to as the Saha-Langmuir equation and is a measure of the fraction of neutral atoms n_a with ionization energy I that will evaporate as ions from a surface with work function Φ and temperature T. The ratio of the vibrational frequencies of the adsorbed atom and ion, ω_i/ω_a, is approximately of order unity and is routinely dropped from the equation [49]. g_a and g_i are the statistical weights of the atomic and first ionic ground states. A general expression for the statistical weight of species x is given by:

$$g_x = \sum_{n=0}^{\infty}(2J_n + 1)e^{-E_n/k_BT}, \tag{2.7}$$

where J_n is the total angular momentum J of the n^{th} atomic or ionic level, and E_n is the excitation energy of the n^{th} ($E_0 = 0$) [64]. The ionization efficiency, β, is related to the degree of ionization by [30, 55]:

$$\beta = \frac{\alpha}{1+\alpha}. \tag{2.8}$$

A thorough derivation of the Saha-Langmuir equation from thermodynamic considerations is outlined in Appendix 1.

The Saha-Langmuir equation was first proposed by Langmuir and Kingdon in 1924 [65] and thereafter experimentally verified numerous times in a variety of different systems, including but not limited to: alkalis and alkaline-earths on rhenium [48], rare-earths on tungsten [66], alkalis and alkali salts on tungsten and platinum [67, 68].

The Saha-Langmuir equation is implicitly limited to adsorbed atoms on a clean, homogeneous surface in thermodynamic equilibrium and does not consider the electron transfer processes between the adatom and the surface. In other words, the Saha-Langmuir equation makes two fundamental assumptions: (a) the mean residence time of adsorbed particles exceeds the time required for electron transfer between the adatom and surface, and (2) the mean residence time is sufficient for complete thermodynamic equilibrium. Deviations from Eq. 2.6 occur when considering the variability in the metal work function of different crystal faces in a polycrystalline surface and the influence on the work function by diffuse foreign impurities embedded in the metal crystal and induced heterogeneity arising from the adsorption of parasitic gases (e.g., O_2, N_2 and H_2). These deviations, the influence of the binding energy of adsorbed atoms on their mean residence time, and the influence of external electric fields on the degree of ionization will be considered in Sections 2.1-2.3. Furthermore, Section 2.4 will provide an overview of particular ion neutralization phenomena at metal surfaces.

2.1 Adsorption and induced heterogeneity of a metal surface

The adsorption of foreign atoms on a metal surface can have a profound effect on the local work function of the metal, effectively hindering or enhancing the efficiency of surface ionization. The flux of atoms per unit area striking a surface, Z, is related to the pressure, p, by the Hertz-Knudsen equation [69]:

$$Z = \frac{p}{\sqrt{2\pi m k_B T}}. \tag{2.9}$$

An adsorbed monolayer of foreign atoms will form on a metal surface within 1 s, assuming a sticking coefficient of unity and a background pressure of 10^{-6} Torr [29, 9, 70, 71, 72]. An equivalent adlayer would form in about 1000 s at a background pressure of 10^{-9} Torr. For consistent and effective surface ionization, it is necessary to maintain a clean metal surface by limiting the background pressures to $< 10^{-6}$ Torr and operating the metal surface at sufficiently high temperatures in order to purge the surface of adsorbed foreign atoms. The appropriate surface temperature depends on the adsorption mechanism and corresponding binding energy of foreign atoms.

At the onset, we may distinguish between two modes of adsorption, physical adsorption and chemical adsorption, depending on the strength of the interaction between the adatom and metal surface. Physical adsorption is mediated by relatively weak van der Waals interactions between mutually induced dipole moments in the electronic shells of the adatom and surface, giving rise to binding energies on the order of $\lesssim 100\,\mathrm{meV}$ [29, 49, 73]. Physical adsorption is non-specific and can occur on all solids with all gases [9], albeit preferentially on crystal planes with high atom densities [74] or concave cracks in a metal [75]. The resulting dipole layer formed by physically adsorbed species reduces the work function for the metallic electrons [29].

Conversely, bonds between an adatom and a surface with binding energies in excess of $1\,\mathrm{eV}$ are categorized as chemisorptive and encompass homopolar (weak chemisorptive bonds) and heteropolar (strong chemisorptive bonds resulting from charge exchange between the adatom and metal substrate) [29, 76]. Homopolar chemisorption results when both the adsorbate and metal surface contribute an electron with unpaired spin to a mutual binding orbital, as described for the covalent bond in a hydrogen molecule [77]. Covalent adsorption increases the magnitude of the effective work function of the metallic electrons [29].

In contrast to homopolar adsorption, which only involves an interpenetration of the electronic shells of the adsorbate and metal, heteropolar bonds are the consequence of an electron transfer between the adatom and metal. This charge exchange forms a layer of ions on the metal surface and an oppositely charged layer of image charges in the metal. This double layer is an augmented version of that inherent to a clean metal surface at a finite temperature (see Figure 2.3a). Whether the adlayer or image charge layer is positively charged depends on the relationship between the ionization energy of the adsorbates and the work function of the metal. Should the work function exceed the ionization energy of the adatom, an electron is transfered from the adatom to the metal, creating a layer of positively charged ions on the surface which facilitate electron emission and effectively reduce the magnitude of the work function of the metal. This occurs for systems such as cesium on tungsten. This positively-charged layer of adsorbed atoms works to lower the effective work function of the tungsten surface. Likewise, in the event that I exceeds Φ, an electron is transfered from the metal surface to the adatom. This charge-exchange manifests as a negatively-charged adlayer and increases the work function of the surface. A common example occurs with oxygen following the dissociative adsorption of O_2 on a metal surface.

2.1.1 Adsorption effects on the work function

To quantify the effect of strongly chemisorbed species on the work function of the surface, one can follow a classical electrostatic approach. Consider the double layer as an electric potential jump, with dipole moment μ [78], number density of atoms at the surface, σ, and the surface coverage of the adsorbates θ. As such, the work function of the clean surface, Φ_0, will change by some amount, $\Phi = \Phi_0 \pm \Delta\Phi$ [57, 29], where:

$$\Delta\Phi \propto \mu\sigma\theta. \tag{2.10}$$

In the case of cesium on tungsten, Boudart demonstrated the lineary $\Delta\Phi$ with respect to θ for $\theta < 0.4$ [79]. Nonlinearity in $\Delta\Phi$ at higher levels of surface coverage can be attributed to interactions among adsorbates.

Table 2.1 lists the binding energy of various adsorbates on tungsten and their associated maximal work function change. Table 2.1 is by no means comprehensive. The binding energy for various adsorbates changes according to the crystal plane of the substrate [10, 80, 81]. Likewise, the change in the tungsten work function following adsorption depends on the surface coverage of the adsorbates and varies according to the crystal plane [29, 57]. The crystallographic heterogeneity in the induced work function change of an adsorbate is most acute with nitrogen, wherein the work function may increase or decrease depending on the crystal plane [80, 82]. Furthermore, the table lists maximal reported work function changes, without regard to the surface coverage of the adsorbate or interactions among adsorbates at high levels of surface coverage. In accordance with the literature, a negative $\Delta\Phi$ corresponds to a drop in the Fermi level and an increase in the magnitude of the work function.

Due to the low binding energy, the desorption of van der Waals adsorbates is relatively rapid, rendering their relatively weak effect on the surface work function short-lived at high temperatures. The binding energies of various covalent and ionic adsorbates on a tungsten surface is shown in Table 2.1 to be much higher.

Adsorbate	Binding or desorption energy (eV)	Reference	Maximal work function change, $\Delta\Phi$ (eV)	Reference
O_2	6.7	[29]	-1.9	[83]
N_2	4.1	[29]	± 0.9	[81, 82, 80]
H_2	2.0	[29]	-0.45	[29]
Ar	0.082	[84, 85]	-0.4	[86]
Xe	0.43	[84, 85]	-1.1	[86]
Li	3.36	[48]		
Na	2.95	[48]		
K	2.64	[48]	2.71	[60]
Rb	2.28	[87]		
Cs	2.01	[88]	2.89	[89]
Ca	3.66	[48]		
Sr	4.38	[48]	2.3	[2]
Ba	4.50	[48]	2.6	[2]

Table 2.1: Binding energies and changes to the work function of tungsten by various adsorbates. In accordance with the literature, a negative $\Delta\Phi$ corresponds to a drop in the Fermi level and an increase in the magnitude of the work function. For additional data regarding the desorption energy of alkaline earth elements from tungsten, see [1, 2, 3, 4].

When it is not introduced to the ionizing surface in a controllable manner, oxygen is a particularly deleterious adsorbate due to its high heat of desorption and strong effect on the work function of the metal.[1]

Extensive data regarding oxygen's influence on the work function of refractory surfaces was collected by Kawano, et. al. [90] and a model for this effect was

---

[1] Note that the adsorption of particular species, namely oxygen for high-temperature applications, can be controllably exploited to change the work function in order to meet the demands of the task at hand. For example, oxygen can be readily introduced to an incandescent refractory metal to enhance the surface ionization efficiency of high I elements [90]. Likewise, thorium, barium, and other elements are incorporated onto hot and cold cathodes to enhance their electron emission capabilities [91].

developed by Delhuille, et. al. [30]. Oxygen adsorption begins with the physical adsorption of O_2 followed by dissociation and formation of strong chemisorption bonds between individual oxygen atoms and the metal surface. Effectively, each oxygen molecule ultimately occupies two surface sites [30]:

$$2 \text{ tungsten sites} + O_2 \leftrightharpoons 2 \text{ oxidized tungsten sites.}$$

Due to oxygen's adsorption kinetics and high binding energy, cleaning the ionizing surface of oxygen *in-situ* requires that the metal be heated to very high temperatures. Kawano reports complete oxygen desorption from a rhenium surface at nearly 2000 K and Kaminsky recommends that the surface be flash heated to approximately 3000 K for thorough cleaning [29, 90].

A final complication regarding oxygen is its reactivity with other adsorbates, particularly those intended for surface ionization. This effect was particularly acute for alkaline earth elements: Stienkemeier, et. al., reported a diminished degree of surface ionization for alkaline earths on a rhenium wire at higher temperatures due to their enhanced reactivity with contaminants, particularly oxides [48]. This reaffirms the results of Müller and Wassmuth [1].

2.1.2 Desorption time

Frenkel's Equation (Equation 2.5) may be re-written to give the residence time of adions and adatoms bound to the surface with adsorption energy $E_{i,a}$

$$\tau_{i,a} = \tau_0 e^{E_{i,a}/k_B T}. \tag{2.11}$$

The prefactor τ_0 is the vibrational period of an adsorbate vibrating perpendicularly to the surface in energy potentials such as those in Figure 2.2. τ_0 is on the order of $10^{-16} - 10^{-13}$ s depending on the mobility characteristics of the adsorbed atoms and ions [48, 87]. Scheer, et. al., include a thorough derivation of τ_0 [58].

Though a minor effect, the time response of surface ionization given in Equation 2.11 does not take into account the temperature dependence of the adsorption energy [58]. Moreover, it does not address the role of oxygen used to enhance the surface work function. The desorption times of alkalis were shown to decrease with an increase in the oxidation of the surface since the adsorbed oxygen functions as an intermediate layer and effectively increases the distance between the surface and alkali atoms [92].

2.2 Intrinsic heterogeneity of the metal surface

The work function is the solid-state analog of the ionization energy in atoms and quantifies the energy required to remove an electron from an electrically neutral solid in vacuum at $0\,\mathrm{K}$, that is, the energy difference between then Fermi energy of a solid and a field-free vacuum in the vicinity of the surface [93, 94, 9]. The work function of a surface is determined, in part, by electrostatic effects having to do with the anisotropic distribution of charge at a crystal surface [95, 96]. The electron distribution at a surface does not terminate abruptly at the metal-vacuum interface, but instead decays with a Debye length of $\sim 1\,\mathrm{\AA}$, forming an electric double layer as shown in Figure 2.3a [9]. The potential of this double layer is exacerbated when the surface is not atomically smooth (Figure 2.3b). In that case, there is a surplus of electrons in the concave portions of the surface.

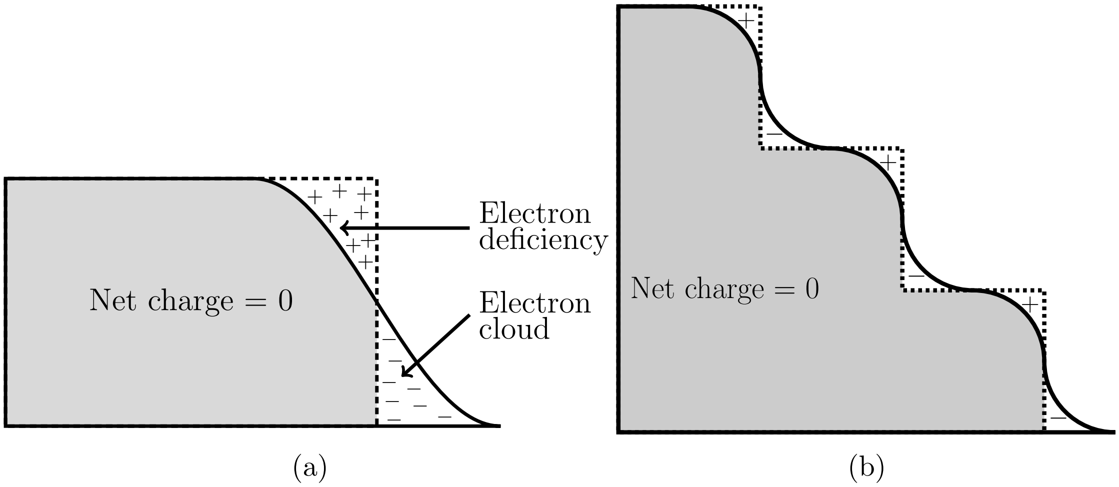

Figure 2.3: (a) the charge distribution of a surface determined by the Fermi-Dirac distribution. (b) is a schematic representing the charge distribution on an atomically rough metal surface, with a surplus of electrons in the concave portions of the metal. Reproduced from [9, 10].

The non-uniformity of this charge distribution at the surface of a metal accounts for the crystallographic anisotropy in the work function, even on completely pure, clean surfaces [9, 91]. Effectively, densely packed surfaces will have higher work functions than atomically rough or loosely packed surfaces. The measured work functions of several crystal planes of tungsten is shown in Table 2.2. For polycrystalline metal surfaces, the empirically determined value of the work function is simply an average of the crystal planes that are present on the surface:

$$\bar{\Phi} = \sum_i c_i \Phi_i,$$

where c_i is the fraction of the metal surface covered by the ith crystal plane. Polycrystalline tungsten wires were used in this experiment as an ionizing surface

Plane	TE [97]	TE [98]	FE [36]	TE [99]	TE [100]	TE [90]
111	4.38	4.3	4.39	-	-	-
116	4.29	4.20	4.30	-	-	-
001	4.56	4.44	-	-	-	-
011	5.26	5.09	5.70-5.99	-	-	-
100	-	-	-	4.59	4.56	-
Polycrystalline	-	-	-	-	-	4.54

Table 2.2: Results of experimental measurements of the work functions of different crystal planes of tungsten. All work functions were quantified by measuring a current of electrons emitted from the surface; TE: thermionic emission of electrons, FE: field emission of electrons. All values are in eV.

for metastable calcium and ytterbium atoms. Note that polycrystalline tungsten has been shown to recrystallize in a preferential direction [101]. As will become apparent in later chapters, the choice of polycrystalline tungsten as an ionizing surface is adequate considering the atomic states of the impinging atoms, even if it gradually recrystallizes throughout the experiment. That is, the energy difference between the ground and excited states of impinging calcium and ytterbium atoms ($> 2\,\mathrm{eV}$) is sufficiently greater than the difference in the work functions of different crystal plans of tungsten ($\lesssim 1\,\mathrm{eV}$). However, should surface ionization be employed for the detection of absolute quantities of trace atomic species in the equivalent atomic states, it is imperative to use atomically clean surfaces of single crystals due to the inadequate knowledge of c_i, the surface coverage of the ith crystal plane of a metal.

One should consider that there is also a temperature dependence of the work function. The Fermi level, $E_F = \frac{\hbar^2}{2m_e}\left(\frac{3n}{8\pi}\right)^{2/3}$, decreases with an increase in temperature since thermal expansion in the metal causes the electron density n to decrease. Because of this, the temperature dependence of the work function can be modeled as $\Phi(T) = \Phi(T_0) + a(T - T_0)$ [29]. However, since the work function was shown to increase by $10^{-5} - 10^{-4}$ eV/K by [102], the temperature dependence of the work function of tungsten can be neglected for the purposes of this experiment.

An additional source of heterogeneity intrinsic to a metal surface is the chemical imperfections in a crystal as the result of foreign atoms in the host lattice [29, 103, 30]. Such impurities diffuse throughout the crystal lattice and can ultimately arrive at the surface, where they may have adverse affects on surface ionization by facilitating the adsorption of foreign atoms [29] and, more importantly, by undergoing direct surface ionization upon diffusing to the surface [30]. Various surface ionization experiments detected an alkali ion current ultimately emanating from impurities in the bulk of the ionizing surface [67, 104]. Delhuille et al. [30] quantitatively address the diffusion of potassium atoms within a rhenium wire which are emitted as ions upon reaching the surface, noting that the current of impurity ions is restricted by the diffusion rate

$$I_{\text{ion}}(t) \propto D e^{-\pi^2 D t / a^2}, \tag{2.12}$$

where a is the metal thickness and the diffusion constant is expressed by an Arrhenius law, $D = D_0 \exp(-E_{\text{diff}}/k_B T)$, where E_{diff} is the diffusion activation energy [30]. Depleting the ionizing surface of impurities can be achieved by baking the metal at a high temperature for several hours, which may be expedited by using a metal with a small thickness, since the time constant of the impurity ion current (Eq. 2.12) scales as a^2.

2.3 Surface ionization in an external electric field

In the event where an externally applied electric field is used to extract and accelerate the ions from the ionizing surface, Equation 2.6 must be modified. The external electric field reduces the image potential of the ion as follows:

$$U_{\text{ext}}(x) = -\frac{e^2}{16\pi\varepsilon_0 x^2} - eFx, \tag{2.13}$$

where the first term originates from the image potential of the ion, x is the distance to the ionizing surface, and F is the external electric field. The maximal point of $U(x)$ is given by

$$U_{\text{ext}} = -e\sqrt{\frac{eF}{4\pi\varepsilon_0}}. \tag{2.14}$$

The external field effectively lowers the ionization energy of the atom, $I - U_{\text{ext}}$ [11]. Equation 2.14 can be subsequently incorporated into the Saha-Langmuir Equation [29]:

$$\alpha = \alpha(F=0)\exp\left(\frac{e\sqrt{eF/4\pi\varepsilon_0}}{k_B T}\right) \tag{2.15}$$

This modification to the Saha-Langmuir Equation was confirmed experimentally [105]. Lastly, for fields in excess of 10^8 V/m, Equation 2.15 must include the difference in the polarization energies of the adatom and the ion [29].

2.4 Deexcitation of metastable atoms and neutralization of ions at a metal surface

As mentioned in Section 1.2, the principal goal of this experiment was to demonstrate that metastable atoms undergo surface ionization at an appreciable rate when compared to the surface ionization rate of ground state atoms. This experiment was carried out with metastable calcium ($I = 6.11\,\mathrm{eV}$) and ytterbium ($I = 6.25\,\mathrm{eV}$) atoms on a tungsten surface, which, in their respective metastable states, have ionization energies of roughly $4.22\,\mathrm{eV}$ and $4.02\,\mathrm{eV}$, respectively (see Figures 3.2 and 3.3). As will be demonstrated in this dissertation, it is the effective ionization energy of the metastable state and its relationship to the work function of the metal surface that determines the surface ionization probability of the atom. However, should the excitation energy of the metastable state be comparable to or greater than the work function of the surface, additional charge exchange processes may occur.

If the work function of the metal surface exceeds the effective ionization energy of the metastable atom ($\Phi > I_{\text{eff}}$), then resonance ionization (process (1) in Figure 2.4a) of the atom by tunneling of the excited electron into an unoccupied electronic state in the metal is highly probable [53, 106]. Resonance ionization fundamentally the same ionization mechanism as in surface ionization.

If E^+, the effective recombination energy of the ion to the neutral atom ground state (which, due to surface effects is approximately $1 - 2\,\mathrm{eV}$ less than the ionization energy of the ground state neutral atom in free space), exceeds double the work function, $E^+ \geq 2\Phi$, then Auger neutralization may occur, wherein an electron from the metal tunnels to the vacant ground state (process (2) in Figure 2.4b). The excess energy from Auger neutralization simultaneously excites a second electron to a higher energy state in the metal [106]. If the excess energy is sufficient, this electron may be ejected and detected (referred to as an Auger electron) [53, 107, 108, 109].

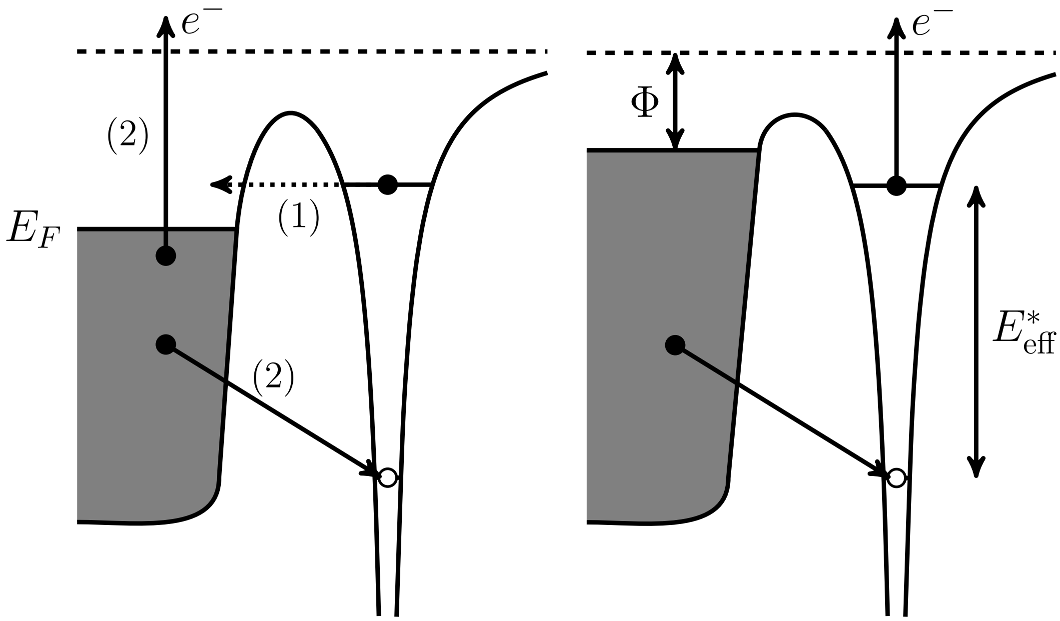

(a) RI + AN (b) AD

Figure 2.4: Some interactions between excited atoms and metal surfaces. (a) Resonance ionization RI (1) followed by Auger neutralization AN (2); (b) Auger de-excitation AD. E^*_{eff} denotes the excitation energy of the metastable atom near the surface, which is distance-dependent. Likewise, I_{eff} denotes the ionization energy of the metastable atom.

However, in the event that $E^+ < 2\Phi$, the emission of an Auger electron is prohibited and an electron in the metal will instead be excited to an unoccupied state following ion neutralization [106]. The condition $E^+ < 2\Phi$ particularly applies to metastable calcium and ytterbium on a clean tungsten surface ($\Phi = 4.54\,\text{eV}$). Our concern at the onset of this experiment was precisely that the calcium and ytterbium ions would immediately undergo Auger neutralization following surface ionization and evaporate from the tungsten surface as neutral atoms.

To our knowledge, detection of positive ions resulting from the interaction between metastable atoms and metal surfaces has only been reported before twice, both times with metastable noble gas atoms [110, 111]. However, the results by Varney were only qualitative [110] and neither result has since been reproduced, likely due to the fact that the Auger garners more interest because of its significance to spectroscopy [112]. Additionally, Auschwitz and Lacmann report the surface ionization of optically excited sodium atoms in the $^2P_{3/2}$ state on a tungsten surface [113]. Specifically, they present a correlation between the intensity of the laser used to pump this transition and ion yield at the tungsten surface.

For the sake of completion, it is worth nothing that if there are no vacant energy levels in the solid for the tunneling valence electron from the atom (i.e., if the work function of the metal is less than the effective ionization energy of the metastable atom, $\Phi < I_{\text{eff}}$), resonance ionization is forbidden and the metastable atom is likely to undergo Auger de-excitation. In this case, an electron from the metal tunnels to the vacant ground state in the atom, triggering the ejection of the excited electron from the atom [53]. The energetic condition for Auger de-excitation to proceed is $E^*_{\text{eff}} > \Phi$, where E^*_{eff} denotes the excitation energy of the metastable atom [106]. Auger de-excitation may occur, for example, for metastable noble gas atoms on low work function surfaces, such as those coated by alkali metals. Nonetheless, Auger de-excitation is not a viable process for metastable calcium and ytterbium atoms on tungsten.

Chapter 3

Applicability to calcium and ytterbium

The primary motive of this experiment was to demonstrate the feasibility of a novel method of isotope enrichment by the selective surface ionization of metastable atoms. Calcium and ytterbium not only have physical properties that are highly suited to this experiment, as will be addressed below, but have stable isotopes of key relevance to fundamental scientific research and medicine.

3.1 Physical properties

Calcium, an alkaline earth metal with atomic number $Z = 20$, is the fifth most abundant element, following aluminum and iron as the third most abundant metal, in the earth's crust, largely appearing as a sedimentary deposit of $CaCO_3$ [114]. Elemental calcium is largely produced by the electrolysis of $CaCl_2$ [114] or by the reduction of calcium oxides and carbonates with aluminum at high temperatures [115], ultimately to be used almost exclusively as a scavenger in steelmaking (to eliminate oxygen, sulfur, and phosphorus impurities) [116]. Elemental calcium has a dull silver appearance but readily forms an oxide and white nitride outer layer when exposed to air [114]. Calcium oxide, CaO, reacts with water, forming calcium hydroxide $Ca(OH)_2$, a base which ultimately allows us to remove Ca and

Property	Value		Unit	Reference
	Ca	Yb		
Atomic number	20	70		
Atomic mass	40.08	173.0	amu	[120]
Density	1.54	6.965	g/cm^3	[121]
Melting point	839	819	°C	[121]
Boiling point	1484	1194	°C	[121]
Temperature at 1×10^{-2} Torr	600	470	°C	[122]
van der Waals radius	2.27	2.26	Å	[123]
Ionization energy	6.11	6.25	eV	[124, 125]

Table 3.1: Relevant physical data for calcium and ytterbium.

CaO deposits from experimental components with acetic acid, where a calcium acetate salt forms according to [117]

$$2\mathrm{CH_3COOH_{(aq)}} + \mathrm{Ca(OH)_{2(aq)}} \longrightarrow \mathrm{Ca(CH_3COO)_{2(aq)}} + 2\mathrm{H_2O_{(l)}}.$$

Relevant physical properties of calcium are listed in Table 3.1.

Ytterbium, a lanthanide metal with atomic number $Z = 70$, has a pale yellow silver appearance. Ytterbium is predominately used in frequency standards [118] and as a dopant in solid-state Yb:YAG lasers [119]. As with the oxides of other lanthanides, the oxide of ytterbium, $\mathrm{Yb_2O_3}$ is insoluble in water but absorbs it to form a hydroxide, and both compounds readily dissolve in aqueous acids (as with calcium compounds, we routinely used diluted acetic acid to dissolve ytterbium compounds) [114]. Physical properties of ytterbium are listed in Table 3.1.

The vapor pressures of calcium and ytterbium over a range of temperatures is shown in Figure 3.1. The normal operating temperature for the atomic beam source was roughly 650 °C, producing vapor pressures of 50 mTorr for calcium and 1.4 Torr for ytterbium. The vapor pressure is closely described by:

$$\log_{10} P = 5.006 + A + BT^{-1} + C \log_{10} T. \tag{3.1}$$

For calcium, $A = 10.127$, $B = -9517$, $C = -1.4030$. For ytterbium, $A = 9.111$, $B = -8111$, $C = -1.0849$. For this formula, P is in Pa and T is in K [121].

3.2 Atomic and spectroscopic properties

As alkaline earth and alkaline earth-like elements, both calcium and ytterbium are characterized by an atomic structure with two valence electrons. Under Russel-Saunders term symbol notation of ${}^{2S+1}L_J$ to describe the total angular momentum of the atom, the ground state electron configurations for calcium and ytterbium are [126, 127]:

$$\text{Calcium: } [\text{Ar}]4\text{s}^2,\ \ {}^1S_0$$

$$\text{Ytterbium: } [\text{Xe}]4\text{f}^{12}6\text{s}^2,\ \ {}^1S_0$$

Considering the two electrons in the outer shells, the total spin S can take values of 0 or 1, giving rise to singlet ($2S + 1 = 1$) and triplet ($2S + 1 = 3$) states, respectively. Not surprisingly, the spectra of calcium and ytterbium, shown in Figures 3.2 and 3.3 are very similar.

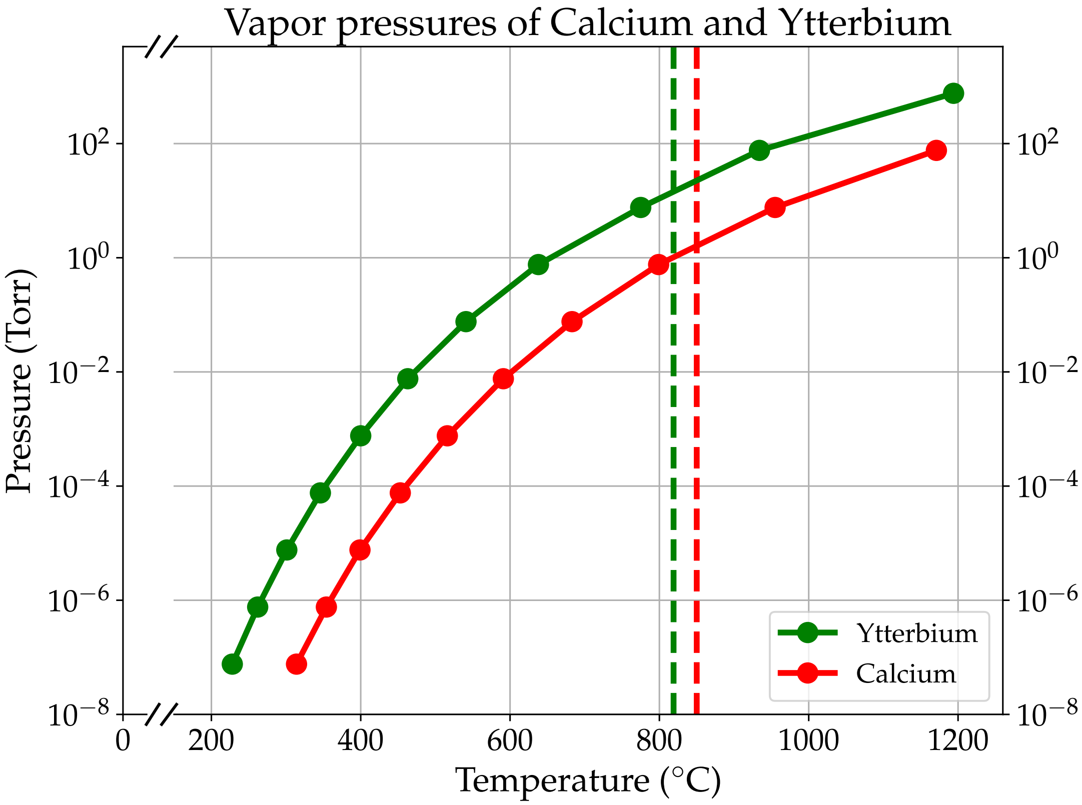

Figure 3.1: Vapor pressures of calcium and ytterbium. The dashed vertical lines mark the respective melting temperatures. Typical oven temperatures ranged from $550 - 650\,^{\circ}\mathrm{C}$.

3.2.1 Transition intensities

The intensity of the spectral line corresponding to a transition from the level k to the level i of an atom is given by

$$I_{ki} = W_{ki} h \nu_{ki}, \tag{3.2}$$

where W_{ki} is the total rate of spontaneous emission for the transition and ν_{ki} is the frequency of the corresponding photon [128, 129]. The rate of spontaneous emission is proportional to the total number of atoms per unit volume in the upper level n_k:

$$W_{ki} = A_{ki} n_k, \tag{3.3}$$

where the constant of proportionality, A_{ki}, is the Einstein A coefficient for the transition and is the inverse of the spontaneous radiative lifetime of level k [130]:

$$A_{ki} = \frac{1}{\tau}. \tag{3.4}$$

3.2.2 Relevant transitions

As mentioned in the preceding chapters, the goal of this experiment was to demonstrate the enhanced rate of surface ionization for calcium and ytterbium atoms when excited to metastable states, namely the lowest ^3P_J triplet. The initial round of this experiment, as outlined in this dissertation, consisted of populating the metastable states in a discharge. The finer details of the discharge will be addressed later (see Section 4.2), but for now, it will suffice to consider it simply as an electron impact excitation scheme, wherein the metastable states in calcium and ytterbium are populated either by direct excitation from the ground state or through a cascade from higher-lying states. Calcium and ytterbium are well suited for this experiment because they have modest ground state ionization energies (6.11 eV and 6.25 eV) and metastable states with ionization energies of roughly 4.23 eV and 4.02 eV, respectively. In other words, when considering a clean polycrystalline refractory metal surface (i.e., a work function of 4.5 eV for tungsten) the work function of the metal surface exceeds the ionization energy of the metastable states of calcium and ytterbium but is less then the ground state ionization energies. Consequently, the degree of ionization given by Equation 2.6 is expected to be near unity for metastable incident atoms, but less than 10^{-4} for ground state atoms.

Largely for its expediency, the first round of this experiment as outlined in this dissertation consisted of populating metastable ^3P_J states in calcium and ytterbium through a discharge (see Section 4.2). This scheme inadvertently populated several other atomic states. In order to estimate the degree of ionization of metastable calcium and ytterbium atoms on a refractory metal surface, it is necessary to measure the precise number of incident atoms in the ^3P_J states. In this section, I will address the properties of various atomic states of calcium and ytterbium, as well as atomic transitions that complicated the task of quantifying the number of atoms in the ^3P_J states following the discharge. Future rounds of this experiment (see Chapter 6) will use a laser to enable greater degrees of control and precision for populating the metastable states.

According to the selection rules for atomic transitions, as shown in Table 3.2, transitions within the singlet and triplet manifolds are allowed and are typically characterized by linewidths in excess of 10 MHz. In alkaline earth and alkaline earth-like elements the lowest excited states lie in the $nsnp\ ^3P$ triplet and are regarded as metastable since transitions between manifolds (referred to as "intercombination lines") are forbidden by the rule, $\Delta S = 0$ [5]. However, due to enhanced spin-orbit coupling for heavier atoms, the strength of intercombination lines in these atomic systems becomes more pronounced with increasing Z [131]. In this experiment, this is readily apparent when considering the rate of spontaneous decay of the $^3P_1$ states to the $^1S_0$ ground state in calcium and ytterbium (see Tables 3.3 and 3.4). As with the $^3P_1$ state, transitions from the $^3P_0$ and $^3P_2$ states to the ground state are spin-flip forbidden as well as strongly electric dipole forbidden as $J = 0 \leftrightarrow 0, 2$ is not permitted. Consequently, the $^3P_{0,2}$ spectral lines do not appear in the spectra of alkali earth and alkali-earth like elements or are very week [129]. In calcium, the $^3P_2$ state decays to the ground state via the $^3P_0$ or $^3P_1$ states, of which the former decays to the ground state through a two-photon E1M1 process with an estimated rate of $3.9 \times 10^{-13}\,\mathrm{s}^{-1}$ [131]. In bosonic ytterbium, these states exhibit similar radiative decay characteristics as in calcium [127]. However, in fermionic alkaline earth systems, the hyperfine interaction between the total angular momentum J and the finite nuclear spin I quenches the $^3P_0$ resulting in a finite linewidth of $\Gamma < 2\pi \times 10\,\mathrm{mHz}$ [132]. Given the greater natural abundance of fermionic ytterbium isotopes in contrast to calcium isotopes (see Table 3.5), the $^3P_0$ state is routinely exploited in metrology applications for its exceedingly narrow linewidth less than 10 mHz [132].

Although the $^1P_1$ state lies above the metastable triplet in calcium and ytterbium, the $^1S_0 \leftrightarrow {}^1P_1$ transition is often considered the resonance transition for these systems since it is significantly stronger than the intercombination transition from the $^3P_1$ state. This state has spontaneous emission rates of $2.18 \times 10^8\,\mathrm{s}^{-1}$ and $1.76 \times 10^8\,\mathrm{s}^{-1}$ for calcium and ytterbium, respectively, and thus very short lifetimes on the order of a few nanoseconds [133, 134]. Due to its large rate of spontaneous decay, the decay of this state is the most intense spectral line in calcium and likewise one of the most intense in ytterbium. Although, for the most part, atoms in the $^1P_1$ state will have long decayed to the ground state before reaching the ionizing surface, it is worthwhile to note that this state is not a closed transition and some fraction of $^1P_1$ atoms may decay to the ^3P triplet through the intermediate states $4s3d^1D_2$ in calcium and $6s5d^3D_{1,2}$ in ytterbium [133, 135, 136].

In calcium, rather than decaying to the ground state, some fraction (10^{-5}) atoms in the $^1P_1$ state may decay into the $^1D_2$ state at a rate of $2.1 \times 10^3\,\mathrm{s}^{-1}$ [133, 137]. When populating the calcium metastable state through a discharge, the reasons the calcium $4s3d^1D_2$ state is problematic are twofold: first, this state partly populates the metastable triplet as it spontaneously decays to the $^3P_1$ and $^3P_2$ states at rates of $300\,\mathrm{s}^{-1}$ and $96\,\mathrm{s}^{-1}$, respectively [133, 137, 138]. Considering these rates, during the time between electron excitation at the discharge and impingement on the incandescent ionizing metal surface, it is mainly the $^1D_2 \rightarrow {}^3P_1$ that slightly augments the population of metastable $^3P_1$ atoms in the atomic beam in a manner that cannot be easily detected in the current set-up. Second, the most adverse effect of the $^1D_2$ state in calcium is its exceedingly long lifetime of $2.3\,\mathrm{ms}$

[138]. The total radiative decay rate out of the $^1D_2$ level is less than $500\,\mathrm{s}^{-1}$ since the $^1D_2 \rightarrow {}^1S_0$ is also dipole forbidden and instead proceeds by electric quadrupole radiation with a rate of $90\,\mathrm{s}^{-1}$ [138]. The long lifetime and high excitation energy (2.7 eV) of $^1D_2$ calcium atoms implies that they too may undergo surface ionization along with ^3P_J atoms. This is problematic given that the number of $^1D_2$ atoms following the discharge cannot be adequately quantified in the current set up. Consequently, the degree of surface ionization that may be computed from the data in Chapter 5 is fundamentally an underestimate due to the imprecise knowledge of impinging metastable calcium atoms.

For completeness, it should be noted that in ytterbium, as in calcium, there is a leakage channel from the $^1P_1$ singlet state to ^3P_J metastable states, though it proceeds through the triplet $^3D_{1,2}$ states [139]. The rate of this channel limited by the low rate of spontaneous decay of the $^1P_1 \rightarrow^3 D_{1,2}$ intercombination transitions [134, 135].

The detailed mechanics of the discharge will be addressed in Section 4.2. The end result is that the metastable ^3P_J states in calcium and ytterbium get populated with relative populations of $g_J = 2J + 1$ (accordingly, the ratio is $1 : 3 : 5$) either through direct excitation from the ground state or following a cascade of decays from higher excited atomic levels. Lacking a suitable laser system to probe one of the three dipole allowed transitions $^3S_1 \leftrightarrow {}^3P_J$, quantifying the post-discharge population of the ^3P_J states was limited to detecting a decay to or from the metastable states. This was most straightforward for ytterbium, which exhibits an intense decay from the $^3P_1$ state with a lifetime shorter than 1 μs [134].

Transition type	ΔJ	ΔS	ΔL
E1 Electric dipole	$0, \pm 1$	0	$0, \pm 1$
E2 Electric quadrupole	$0, \pm 1, \pm 2$	0	$0, \pm 1, \pm 2$
M1 Magnetic dipole	± 1	0	0

Table 3.2: Selection rules for electric dipole, electric quadrupole, and magnetic dipole radiative transitions between L-S coupled states [5, 6]. Note that for both ΔJ and ΔL, $0 \nleftrightarrow 0$ is forbidden.

According to the ratio of multiplicities of the metastable state, the number of atoms detected from the $^3P_1$ decay would correspond to a third of the total number of atoms excited to the metastable triplet. The intensity of th $^3P_1$ 556 nm radiation would be indicative of the number of atoms remaining in the long-lived $^3P_{0,2}$ states. In calcium, the same transition proceeds at a much lower rate ($2300\,\mathrm{s}^{-1}$), ultimately rendering the 657 nm signal to be fairly weak in a wavelength range overwhelmed by the blackbody radiation from the calcium source. Without a way to chop the 657 nm signal to enable lock-in detection, a circuitous but effective way to quantify the population of metastable calcium atoms was to detect the blue $^3D_J \leftrightarrow {}^3P_J$ transitions. The detection procedure of these transitions in calcium and ytterbium is addressed in more detail in Section 5.2.

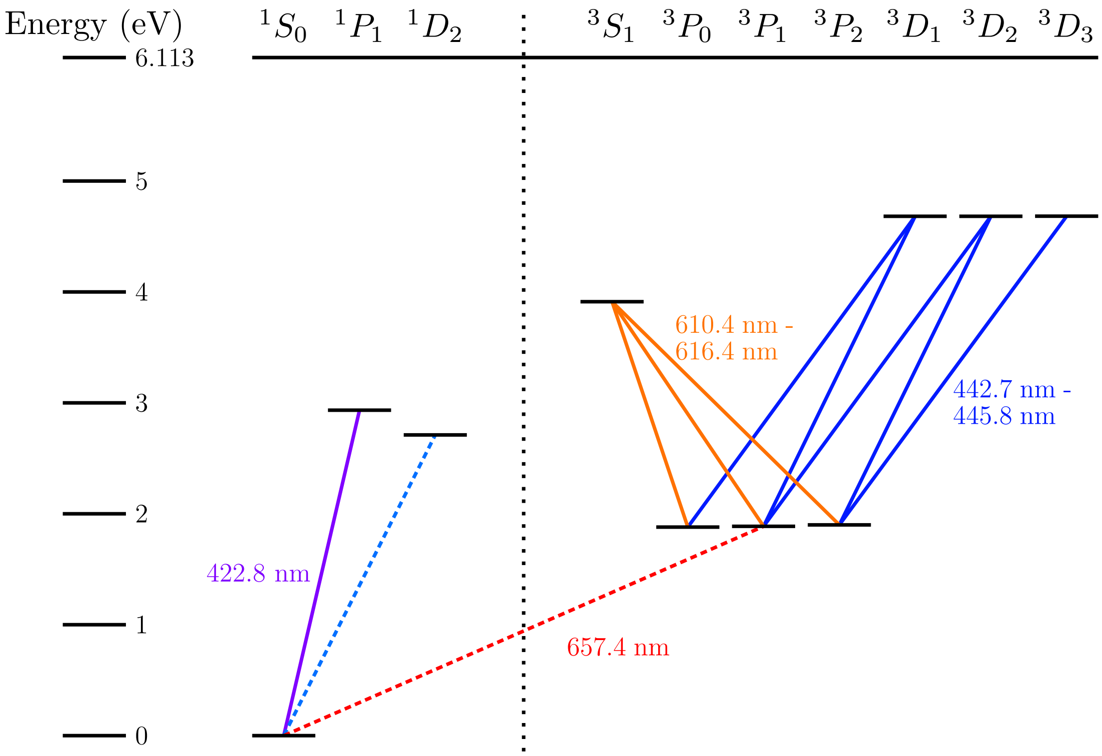

Figure 3.2: Energy level diagram for calcium. The metastable states we aimed to populate in this experiment are the $^3P_{0,1,2}$ triplet states.

3.3 Isotopic relevance

In addition to having easily accessible metastable states with sufficiently low ionization energies, isotopes of calcium and ytterbium also have various applications in medicine [143, 144, 145, 146] and basic scientific research [147, 148]. As mentioned in Section 1.2, the ultimate purpose for investigating the surface ionization of metastable atoms is a proof-of-concept experiment for a novel method of isotope enrichment, the premise of which would be to optically pump atoms to long-lived metastable states, which undergo surface ionization at greater rates

Initial	Final	Wavelength (nm)	A (s^{-1})	Reference
$^1P_1$	$^1S_0$	422.8	$2.18 \cdot 10^8$	[133]
$^1P_1$	$^1D_2$	5547	2180	[133]
$^1D_2$	$^1S_0$	457	40	[133]
$^1D_2$	$^3P_{1,2}$		96-300	[133]
$^3P_1$	$^1S_0$	657.4	2300	[140, 138]
$^3D_{1,2,3}$	$^3P_{0,1,2}$	442.7-445.8	10^7	[141]

Table 3.3: Wavelengths and rates of spontaneous decay for relevant transitions in calcium.

Initial	Final	Wavelength (nm)	A (s^{-1})	Reference
$^1P_1$	$^1S_0$	389.9	$1.76 \cdot 10^8$	[134]
$^3P_2$	$^1S_0$		$4.2 \cdot 10^{-4}$	[139]
$^3P_1$	$^1S_0$	555.8	$1.1 \cdot 10^6$	[134]
$^3P_0$	$^1S_0$	578.4	$1 \cdot 10^{-2}$	[132, 142]
$^3S_1$	$^3P_2$	649.1	$9.7 \cdot 10^6$	[139]
$^3S_1$	$^3P_1$	680.1	$2.7 \cdot 10^7$	[139]
$^3S_1$	$^3P_0$	770.2	$3.7 \cdot 10^7$	[139]
$^3S_1$	$^1P_1$	1311.2	$1.6 \cdot 10^5$	[139]

Table 3.4: Wavelengths and rates of spontaneous decay for relevant transitions in ytterbium.

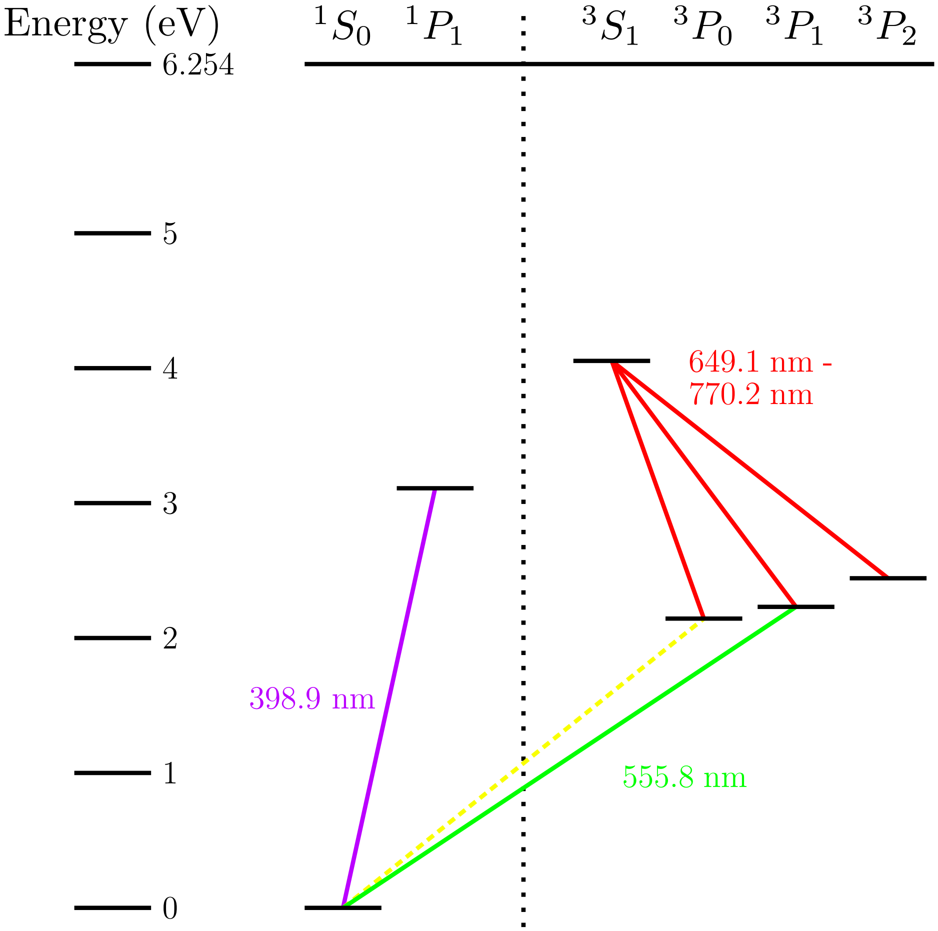

Figure 3.3: Energy level diagram for ytterbium. The metastable states we aimed to populate in this experiment are the $^3P_{0,2}$ triplet states.

than atoms in the ground state. In the case of calcium, this would solely require a single laser system to pump the atoms of the target calcium isotope to the $^3P_1$ state, which has an ionization energy of 4.23 eV. As for ytterbium, since the rate of spontaneous decay of the $^3P_1$ state is markedly greater (in excess of $1 \times 10^6\,\mathrm{s}^{-1}$) than in calcium, it would be more prudent to employ two laser systems to shelve the atoms of the target isotope in the long-lived $^3P_{0,2}$ states via the $^3S_1$ state. This will be addressed in more detail in Chapter 6. In both systems, the isotope shift in the $^3P_1 \leftrightarrow {}^1S_0$ transition will be exploited to achieve the necessary isotopic selectivity when populating the metastable states.

The differences in mass (mass effect) and charge distribution (field effect) of the nucleus of different isotopes of mass A and A' manifest as a spectral isotope shift $(\Delta\nu_i s)_k^{AA'}$ for each transition k. The total isotope shift, therefore, has contributions from the mass and field effects:

$$(\Delta\nu_i s)_k^{AA'} = M_k \frac{A' - A}{AA'} + F_k \delta\langle r^2\rangle^{AA'}. \tag{3.5}$$

M_k and F_k are the mass-shift and field-shift coefficients, respectively, and $\delta\langle r^2\rangle^{AA'}$ accounts for the variation in the nuclear charge radius [149]. It is only for heavy atoms that the field effect dominates the isotope shift [150, 151]. The isotope shift in the $^1S_0 \leftrightarrow {}^3P_1$ transition for various calcium and ytterbium isotopes is shown in Table 3.5.

	Isotope	Natural abundance (%)	$^1S_0 \leftrightarrow {}^3P_1$ $\Delta\nu_{is}$ (MHz)
Ca	40	96.94	0
	41	$1 \cdot 10^{-12}$	280.8
	42	0.65	509.5
	43	0.14	782.2
	44	2.09	996.2
	46	$4 \cdot 10^{-3}$	1481.1
	48	0.19	1922.5
Yb	168	0.13	4610.0
	170	3.05	3241.2
	171	14.3	-1177.2 ($\frac{1}{2} \to \frac{1}{2}$)
	172	21.9	1954.9
	173	16.12	-1431.9 ($\frac{5}{2} \to \frac{7}{2}$) 3266.2 ($\frac{5}{2} \to \frac{5}{2}$)
	174	31.8	954.8
	176	12.7	0

Table 3.5: Natural abundance of various stable isotopes of calcium and ytterbium. Data for the isotope shift of the intercombination transition in calcium relative to calcium-40 is from Bergmann [7]. Data for the isotope shift of the same transition in ytterbium relative to ytterbium-176 is from Pandey [8].

Chapter 4

Experimental overview

The setup used in this experiment consists predominantly of a thermal atomic beam source, an electric discharge excitation for populating the metastable states of calcium and ytterbium, and a surface ionization detector. All of these items are enclosed in a custom stainless steel[1] vacuum chamber, shown in Figure 4.1, maintained at a pressure range of $10^{-7} - 10^{-6}$ Torr during normal operation. All of the calcium and ytterbium used in this experiment was purchased from ESPI Metals as granules enclosed in argon-filled cans to minimize oxidation during transportation.

4.1 Effusive atomic beam source

4.1.1 Theoretical considerations

Subtleties in the mechanics of the electric discharge used to populate the metastable state required that the density of the atomic beam be sufficiently high to support a self-sustaining glow discharge (see Section 4.2 for more details). To reach the necessary densities for calcium and ytterbium, the atomic beam source needed to be able to consistently reach temperatures in excess of 700 °C.

---

[1] Unless otherwise stated, all stainless steel used throughout the experiment consists of 304 stainless steel.

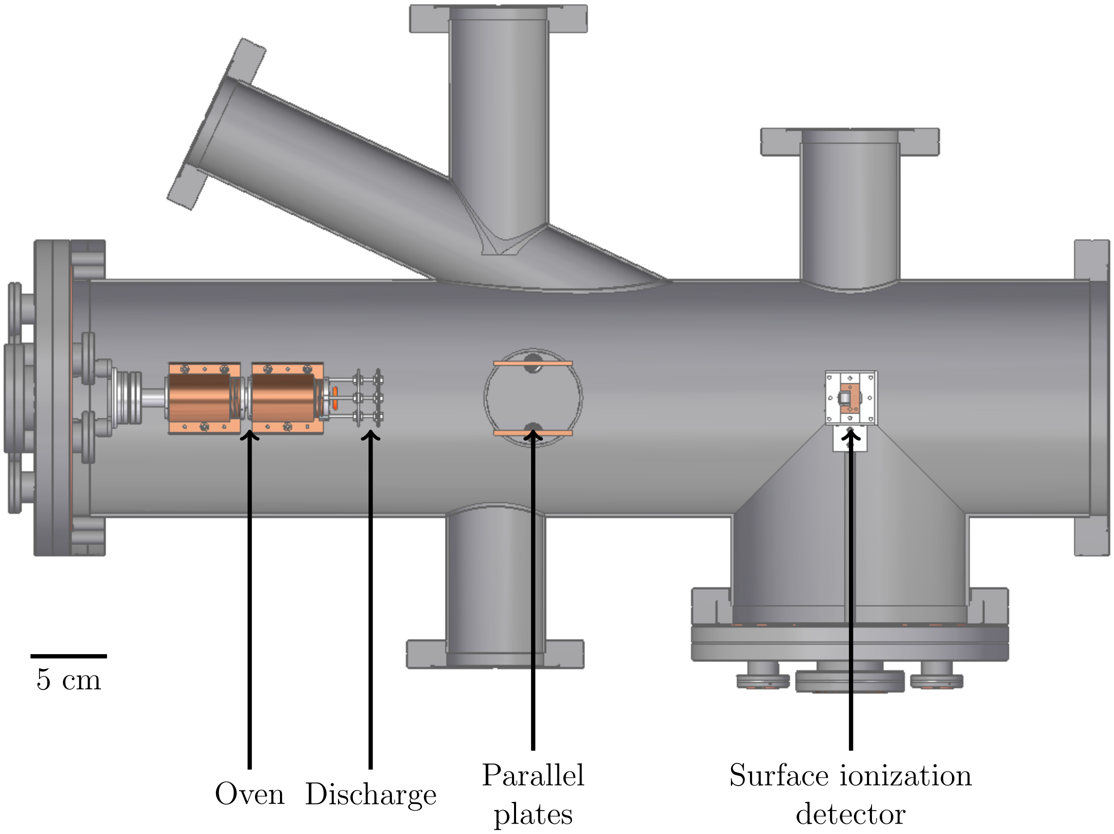

Figure 4.1: An overview of the experimental setup for the surface ionization of metastable calcium and ytterbium atoms. The oven on the leftmost flange produces a thermal atomic beam of calcium or ytterbium that is bombarded by electrons in a discharge. All charged particles produced in a discharge are extracted from the beam by a pair of transverse parallel plates. The remaining neutral atoms (a composition of ground state and metastable atoms) impinge on the surface ionization detector, which can be moved transversely by a linear actuator (not shown). A half-nipple is welded on the chamber at 35° to facilitate the in-situ temperature calibration of the hot wire with a pyrometer. The oven is mounted on four stainless steel legs of variable length so that the oven position may be changed if necessary.

The atomic beam source used in this experiment consists of a two-part multi-channel oven based loosely off of the design in [152]. The reservoir was heated to a variable temperature T to vaporize the metallic granules. In equilibrium, the vapor pressure, p, at a particular temperature is shown in Figure 3.1 and the density of the gas, n, may be described by the ideal gas law

$$n = \frac{p}{k_B T}. \tag{4.1}$$

The average distance traveled by a particle between successive collisions – the mean free path – is given by

$$\lambda = \frac{1}{\sqrt{2}\sigma n} = \frac{k_B T}{\sqrt{2}\pi d_0^2 p}, \tag{4.2}$$

where $\sigma = \pi d_0^2$ is the collision cross-sectional area, d_0 is the atomic diameter, and n is the gas density given by Equation 4.1 [153, 11]. The mean free paths of calcium and ytterbium are plotted over a range of temperatures in Figure 4.2.

Consider the source opening to be a single channel with length L and radius a. Different operating regimes can be distinguished, depending on the relationship between the mean free path and the aperture dimensions [11, 152, 153, 154, 155]:

> Effusive/molecular flow regime: $\lambda \gg a, L$. In this mode, atom-wall collisions dominate and an atom in the reservoir traveling in the direction of the tube will pass through the aperture without an atom-atom collision. The beam intensity is proportional to the gas pressure in the source and the beam shape is determined by the aperture geometry [155].

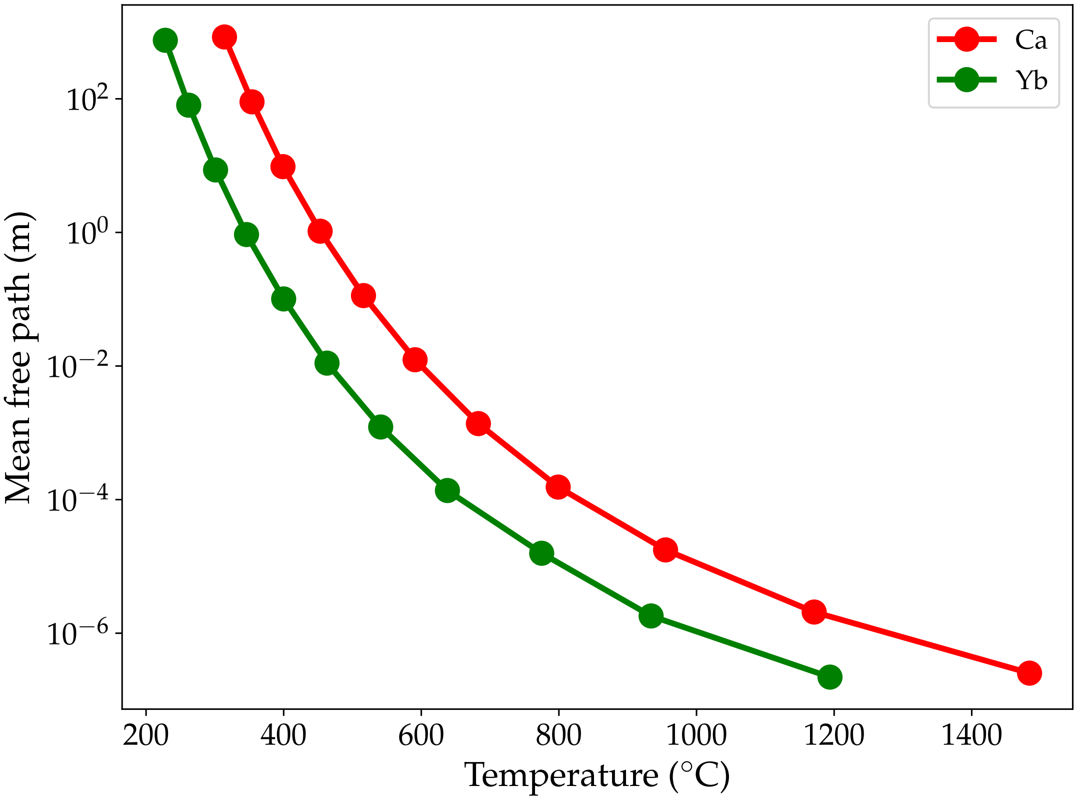

Figure 4.2: Mean free paths of calcium and ytterbium over a range of temperature as given by Equation 4.2 and data from Table 3.1 and Figure 3.1.

Transitional/opaque regime: $\lambda > a$, $\lambda \lesssim L$. Interatomic collisions may no longer be neglected and the average number of gas-phase collisions is estimated to be $2L/\lambda$ [154].

Gas dynamic/hydrodynamic regime: $\lambda \ll a, L$. This mode is characterized by high intensity beams with narrow velocity distributions. This continuum flow will not be considered here.

In this experiment, the calcium and ytterbium sources were operated in the effusive and opaque regimes. Effusive beams are advantageous for a number of reasons, but mainly for their calculable intensities and velocity distributions. The total flux of atoms effusing through a long channel is

$$\Phi = \frac{1}{4} W n \bar{v} A_s, \tag{4.3}$$

where W is the flow resistance or transmission probability of atoms through the aperture, $\bar{v}$ is the mean atomic velocity, and A_s is the aperture cross-sectional area [153, 154, 156]. The transmission probability for long channels is $W = 8a/3L$.

In the effusive regime, the normalized velocity distribution of atoms exiting the source at angle θ relative to the aperture axis is given by the normalized Maxwell-Boltzmann velocity distribution [154]

$$P(v) = \frac{2}{\alpha}\left(\frac{v}{\alpha}\right)^3 \exp\left(-\frac{v^2}{\alpha^2}\right), \tag{4.4}$$

where $\alpha = \sqrt{2k_B T/m}$, the most probable velocity is $v_{\mathrm{mp}} = \sqrt{3/2}\alpha$, and the average velocity is $\bar{v} = (3/4)\sqrt{\pi}\alpha$. The velocity distributions of the calcium and ytterbium beams are compared in Figure 4.3 at 650 °C.

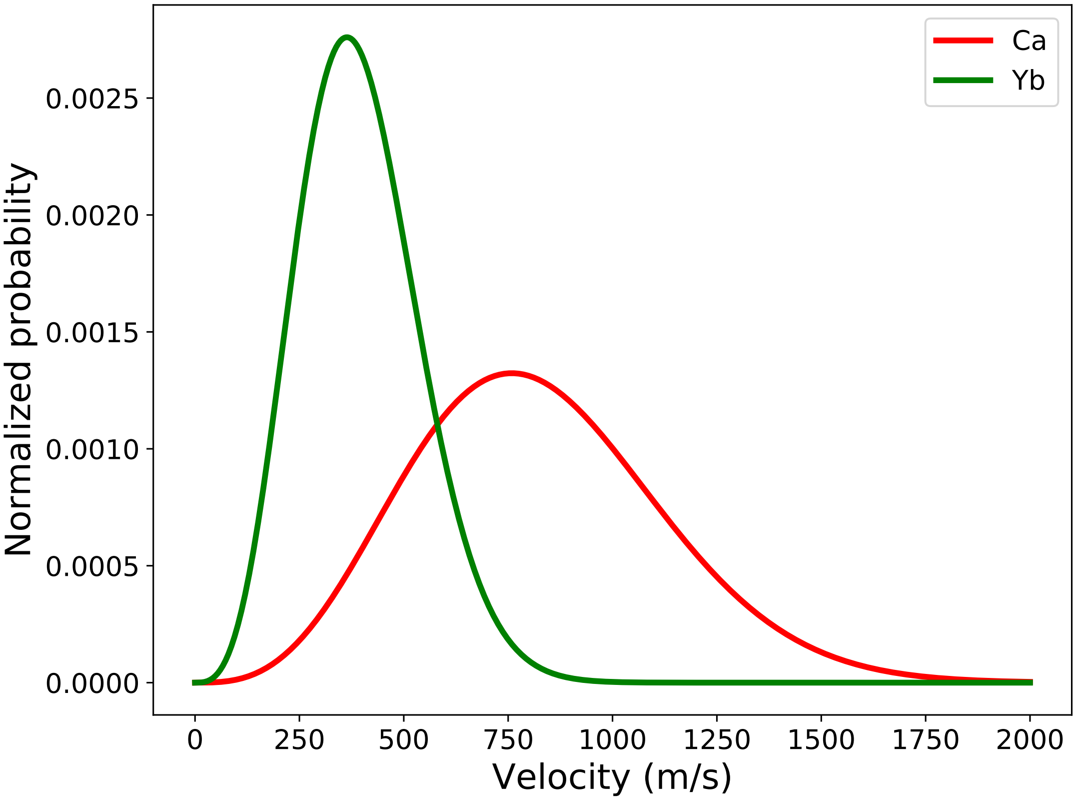

Figure 4.3: Normalized velocity distributions of Equation 4.4 of the calcium and ytterbium atomic beams at 650 °C.

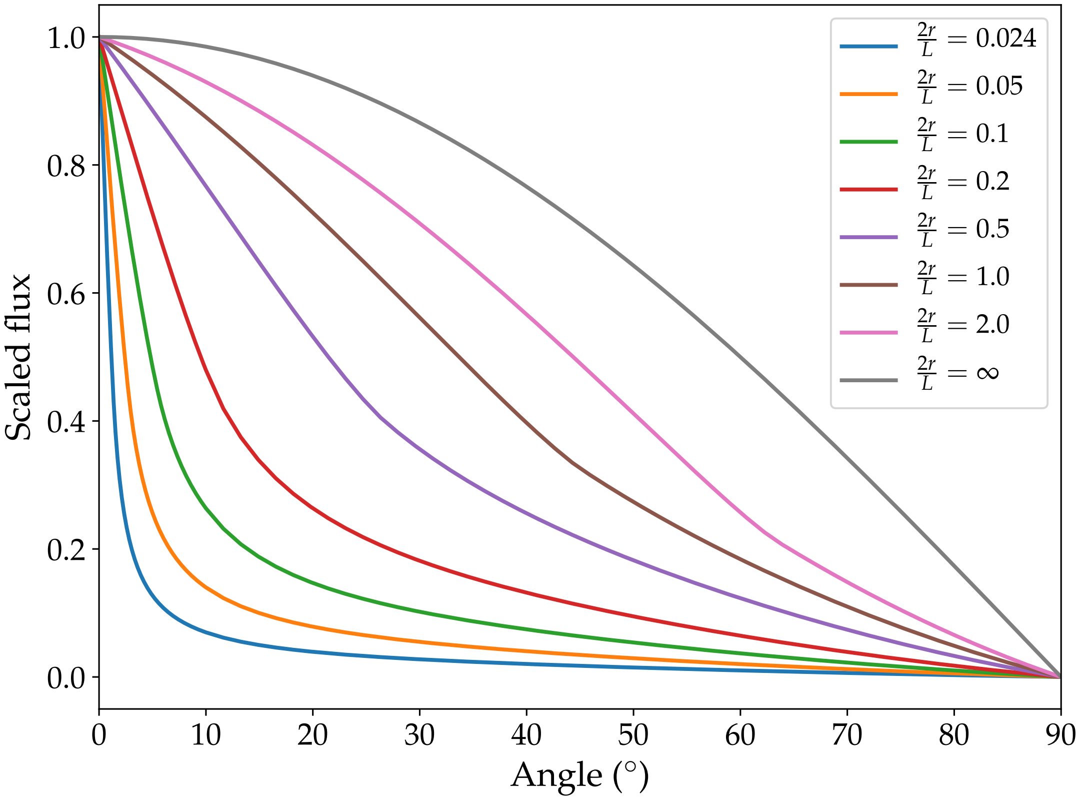

Figure 4.4: Angular distribution for an effusive beam for various apertures according to [11]. The channels used in this experiment have $2r = 1.14\,\mathrm{mm}$ and $L = 48.3\,\mathrm{mm}$. $2r/L = \infty$ corresponds to the cosine distribution of a thin-walled aperture.

Figure 4.4 shows the angular distribution in the effusive regime normalized to the center-line intensity for various apertures, of which the ones used in this experiment are noted in blue [11]. In equilibrium, the angular distribution of an effusive source is only dependent on the atom-wall collision rate, $\nu = \frac{1}{4}n\bar{v}$ [154, 157]. Atoms undergo diffuse reflection off the inner walls of the source; after residing on the wall for a finite time (Equation 2.11), atoms are reemitted isotropically and independently of the incident angle. Consequently, atoms in the resulting beam emitted at angles $\theta \geq 2r/L$ have undergone a minimum of one wall collision. For this reason, the atom flux at large angles can never be eliminated. Note that the diffuse reflection of atoms off the aperture walls implies that some may be retroreflected and re-enter the reservoir. This consequence is exploited by multichannel arrays to extend the lifetime of the source [152].

As mentioned previously, the atomic beam source was occasionally operated at higher temperatures and vapor pressures in order to generate a beam of higher intensity and density. Particularly for ytterbium, higher densities were required in order to support a self-sustaining discharge. As the source temperature was increased, interatomic collisions became comparable in frequency to atom-wall collisions, rendering the source aperture opaque, as described by Pauly and Beijerinck [11, 154]. In the transitional, opaque regime, the total flux may still be described by Equation 4.3, until the source pressure is sufficiently great and hydrodynamic effects must be taken into account [157]

Before proceeding, it is helpful to introduce the dimensionless ratio of the mean free path to aperture length, the Knudsen number [154, 11]

$$K = \frac{\lambda}{L}. \tag{4.5}$$

The effusive regime necessarily has a large Knudsen number ($K \to \infty$). The properties most strongly affected during the transition from an effusive to opaque mode of operation are the angular distribution and center-line ($\theta = 0$) intensity. A drop in the Knudsen number is consistent with an increase in interatomic scattering and opacity in the aperture. The center-line intensity of an opaque emitter correspondingly decreases with the Knudsen number [154]

$$I(\theta = 0)_{\text{opaque}} = I(0)_{\text{effusive}} K^{1/2}, \tag{4.6}$$

where the centerline intensity for an effusive emitter is

$$I(0)_{\text{effusive}} = \frac{1}{4\pi} n\bar{v} A_s. \tag{4.7}$$

The angular distribution in the transitional regime has three contributions: (a) atoms emitted directly from the source without scattering, (b) atoms diffusely remitted from the channel walls, and (c) atoms that undergo gas-phase collisions when exiting the channel. Since atom-wall and inter-atom collisions must both be considered, it requires knowledge of the number density profile (which cannot be calculated exactly) in addition to the wall collision rate [154, 157]. Pauly [11] graphically depicts the angular distribution of a source for various Knudsen numbers. As the Knudsen number decreases, the angular distribution for large angles remains roughly unchanged and levels off as $\theta \to 0$ to a decreased center-line intensity [154]. Consequently, the half-width increases and the angular distribution broadens for decreasing Knudsen numbers. Note that the velocity distribution of the beam is perturbed as well in the opaque regime since slow atoms are more susceptible to collisions due to their longer time-of-flight and will be preferentially scattered out of the center-line [154].

Lastly, multichannel sources will be addressed since the calcium source used in this experiment was a 28-channel source inspired by [152]. Two primary advantages of employing an array of channels are an increase in source lifetime (due to the aforementioned diffuse reflection of atoms off the channel walls) and an increase in intensity without a compromise in directionality [11, 152]. The directionality is determined by the aspect ratio of the channels, $L/2r$, and the center-line intensity by R^2/L, where R is the radius of the overall aperture [11].

4.1.2 Design considerations

The oven consists of two parts: a reservoir that holds the stock granules of calcium or ytterbium and a nozzle which holds an array of long stainless steel hypodermic needles or capillaries[2] for improved directionality. To accommodate the higher temperature characteristics of calcium and ytterbium (in contrast to lithium as used in [152]) and effectively produce a sizable flux of atoms, the oven needed to be able to operate continuously at temperatures $\lesssim 750\,^\circ\mathrm{C}$. Considering the mean free path of calcium and ytterbium in Figure 4.2, attaining an effusive beam at higher source temperatures would necessitate smaller channels, which would unnecessarily complicate the assembly process. Since the conflat (CF) flanges with

---

[2] Purchased from MicroGroup. Part no.: 304H18XX

copper gaskets used throughout the vacuum chamber are rated for maximal temperatures of 450 °C [158][3], the oven and its heater cables were all enclosed within the vacuum chamber (a modified 8" CF tee) and thermally isolated from the vacuum chamber with various macor ceramic parts.

The first oven designed for this experiment (shown in Figure 4.5) possessed a 1.33" CF flange at its center between the reservoir and nozzle for rapidly refilling the oven. Partly due to a design flaw, this central CF flange was never able to maintain an adequate seal at high temperatures, which substantially diminishes the total beam flux through the capillaries. This 1.33" flange was replaced by a thin-walled, 0.1"-long, 0.5"-wide stainless steel tube. A 1.33" half nipple was attached to the back of the reservoir in later designs but was subsequently welded closed with a stainless steel rod since, not surprisingly, calcium perpetually condensed onto the cold flange, which would have ultimately sealed the flange anyway.

The body of the oven consists of custom-machined 0.025"-thick stainless steel. Oxygen-free copper sleeves were subsequently press-fitted onto the stainless steel body for a nearly 23-fold increase in thermal conductivity [121]. Sixteen round trenches with a radius of 0.045" were threaded over about 1.8" on the copper sleeves to support custom aerorod heater cables from ARi Industries. These heater cables consist of heating wires enclosed in an inconel sheath and insulated with magnesium oxide. The heater cables used to heat the reservoir and nozzle were identical cables with a length of about 5 ft and a diameter of 0.093" so that they

---

[3] See Kurt J. Lesker `https://www.lesker.com/newweb/flanges/flanges_technicalnotes_conflat_1.cfm`.

would fit tightly in the 0.045”-radius grooves. Each cable was brazed onto a 1.33” CF flange with the knife edge directed towards the cable leads such that the flanges interfaced with corresponding half nipples in the vacuum-side of the chamber to facilitate assembly of the oven.

Each heater cable was wrapped around the reservoir or nozzle and held tightly in place by copper clamps. One type-K thermocouple was attached to each heater cable powered by separate transformers to maintain an approximate 100 °C temperature difference between the reservoir and nozzle to prevent any hypothetical clogging of the capillaries by condensed atoms. Initial measurements demonstrated temperature variations of less than 10% along the reservoir and nozzle. In the long term, the vapor pressure of the oven is determined by the temperature of the coldest section of the reservoir – the reservoir leaks heat through the unheated back end connected to the 1.33” CF flange. Calcium and ytterbium ultimately condense onto the back of the reservoir and the temperature of this section determines the long term vapor pressure.

In accordance with [152], the nozzle had a triangular cut down its centerline bored out by a wire electric discharge machining (EDM) process to more easily support a multichannel array of hypodermic needles. These capillaries were packed hexagonally in the triangular bore and clamped in place by a bar at the front face of the nozzle, as shown in Figure 4.6. The capillaries chosen for this experiment had a nominal inner diameter of $2r = 1.14\,\mathrm{mm}$ and a length of $L = 48.3\,\mathrm{mm}$ and thus an aspect ratio in excess of 40. The oven is opaque in the aforementioned operating temperature for both calcium and ytterbium and inevitably so: producing a sufficiently dense atomic beam for a self-sustained discharge (to be addressed) while remaining in the effusive regime would necessitate using microscopic capillaries with diameters less than $\sim 1\,\mu\text{m}$ for ytterbium.

4.2 Electric discharge for populating metastable ^3P_J states

The equilibrium fraction of atoms in the ith state emitted by the source is given by the Boltzmann distribution

$$\frac{n_i}{n} = \frac{g_i}{Z(T)} \exp(-E_i/k_B T), \tag{4.8}$$

where g_i and E_i are the multiplicity and excitation energy of the ith state, respectively, and $Z(T) = \sum_i g_i \exp(-E_i/k_B T)$ is the partition function. All states decay to the ground state after a characteristic lifetime. For calcium and ytterbium the fraction of atoms in the ^3P_J metastable states (explicitly, the $^3P_{0,1,2}$ states in calcium and the $^3P_{0,2}$ states in ytterbium since the intercombination transition has a lifetime of approximately 850 ns [159]) emitted from the source at the operating temperature is vanishingly small – less than 10^{-9} atoms are in the metastable states prior to entering the discharge area. Effectively, all of the atoms in the beam can be considered to be initially in the $^1S_0$ ground state when exiting the source. Consequently, the ^3P_J states must be populated through some external means, such as by implementing a collection of lasers to optically pump atoms into the metastable states. In the case of calcium, this may be done with a single laser stabilized to the 657.4 nm intercombination line; when considering ytterbium, two lasers will be required, one to pump the short-lived 555.8 nm transition and another to shelve

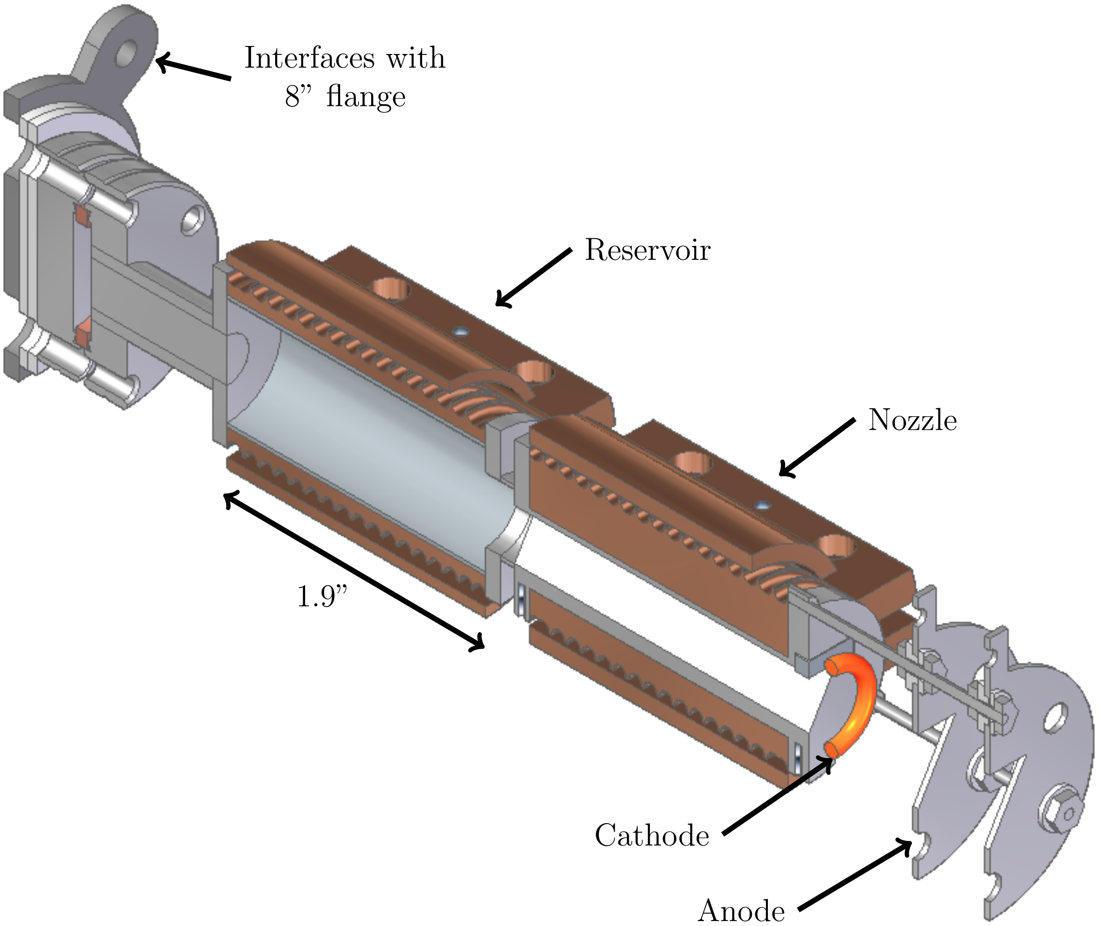

Figure 4.5: Cross-section view of the oven and discharge setup. The bodies of the reservoir and nozzle are composed of 0.025”-thick stainless steel and are welded into a single unit. Copper sleeves were press-fitted onto the reservoir and nozzle for enhanced thermal conductivity. Two identical heater cables (not shown) are wrapped around the copper sleeves and held in place by copper clamps. At the back end of the oven, a series of stainless steel pieces and macor plates thermally isolate the oven from the vacuum chamber. Type K thermocouples are attached to each heater cable beneath the copper clamps for monitoring the oven temperature. The discharge electrodes consist of a toroidal tungsten cathode placed within 1 cm of the nozzle and stainless steel anodes attached via three threaded rods and insulated by a series of alumina ceramic washers.

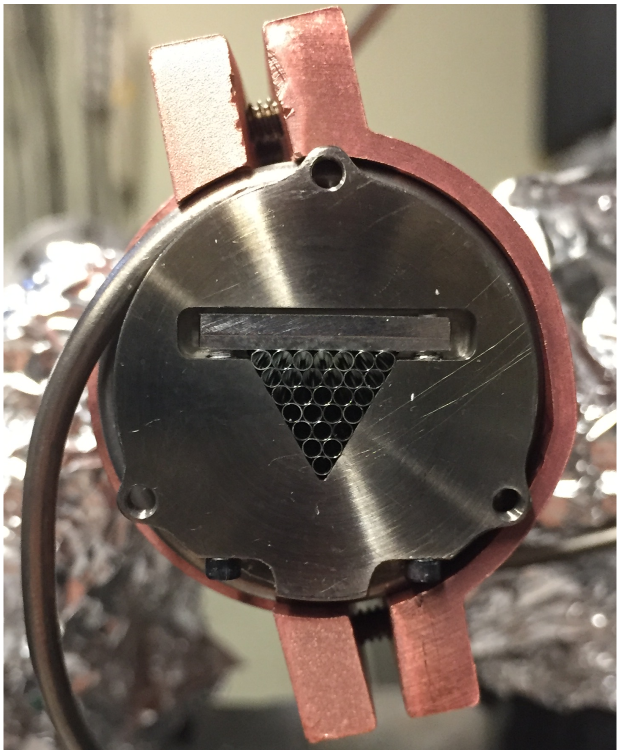

Figure 4.6: Photo of 28 capillaries packed hexagonally into the oven nozzle and held in place by a stainless steel bar. The discharge anode is attached to the front face of the oven via the three 2-56 holes distributed along the circumference of the nozzle.

these atoms in the $^3P_{0,2}$ metastable states via the 680.1 nm transition to the $^3S_1$ state. A markedly more expedient method for populating the metastable states is to employ an electric discharge to excite the atoms through inelastic interactions with free electrons [11]:

$$e^- + A_{n,l} \longrightarrow e^- + A_{n',l'}. \tag{4.9}$$

These inelastic collisions are one of several inter-particle interactions experienced by atoms in a discharge [160]. Two other interactions that will be relevant in this section are ionization (Equation 1.1) and the secondary emission of electrons resulting from the impact of high energy ions on the electrode surface. The first two reactions, inelastic and ionizing collisions, are characterized by different energy-dependent cross sections as shown in Figure 4.8

Various techniques exist to ignite a discharge, the simplest of which is a DC discharge consisting of a positive anode and negative cathode [161, 162]. The gas between the electrodes is initially non-conducting. An increase in the potential difference between the electrodes accelerates electrons emitted from the cathode as a result of sporadic cosmic rays, stray energetic particles, or ambient radiation toward the anode resulting in a current at the anode limited by the electron mobility within the gas [160, 163, 158, 32, 164]. Assuming the field between the electrodes is not sufficient for field emission of electrons, the current saturates for increasing voltages once all of the electrons emitted by the cathode reach the anode. If the inter-electrode voltage is further increased beyond some threshold, free electrons will gain enough energy to collisionally ionize atoms in the gas. For an adequate electric field and gas pressure (i.e., the mean free path must be long enough for electrons to acquire the necessary kinetic energy for ionization and short enough to support additional collisions before reaching the anode), an avalanche Townsend discharge occurs wherein freed electrons undergo multiple ionization collisions before reaching the anode. This avalanche, referred to as a dark discharge, causes an increase in the current at the anode due to the exponentially increasing number of free electrons and is not self-sustaining in that the Townsend discharge ceases below the aforementioned threshold voltage [32]. In a Townsend discharge, the potential drop between the electrodes is uniform and there is an insignificant glow in the gas.

Upon surpassing a critical voltage that depends on the inter-electrode spacing, gas between the electrodes, the gas density, and the external circuit, the Townsend discharge transitions into a glow discharge, which is accompanied by a rapid increase in the anode current. The ionization cascade of the Townsend discharge alone is insufficient fur supporting a self-sustaining glow discharge. This transition occurs once (a) the loss of energy due to inelastic collisions with the gas atoms is recouped from the external electric field and (b) electron losses at the anode are compensated by sufficient electron gains at the cathode. These additional electrons at the cathode may be released due to thermionic emission (i.e., a hot cathode) or secondary electron emission resulting from the impingement of high energy ions [160, 165, 166, 167]. Further increases in the discharge current and voltage will eventually result in an arc [32].

As mentioned above, the breakdown of the gas between the electrodes occurring during Townsend and glow discharges is dependent on the electrode spacing and, more importantly, on the density of the gas and the properties of its constituent atoms. The minimum density of the gas required to support a self-sustaining glow discharge can be found for a given gas as outlined in [168]. We begin by assuming a neutral discharge

$$n_e \simeq n_i, \tag{4.10}$$

where $n_{e,i}$ are the electron and ion densities and impose the condition of charge conservation on the system,

$$\Phi_e = \Phi_i + I/e, \tag{4.11}$$

where $\Phi_{e,i} = n_{e,i}v_{e,i}$ are the electron and ion flux as functions of their velocities and I is the external current. If the ion generation rate is

$$\Phi_i = \sigma_i n_a (I/e) l, \tag{4.12}$$

where σ_i is the ionization cross section, n_a the atomic density, and l is the distance between the electrodes, we arrive at a minimum condition for the atomic beam density that must be met to produce a self-sustained discharge:

$$n_a \geq \frac{1}{l\sigma_i}\sqrt{\frac{m_e}{m_i}}. \tag{4.13}$$

Crucially, this density condition is inversely proportional to the square root of the ion mass, suggesting that a higher density is needed for a self-sustained ytterbium discharge, despite the similarity between the vapor pressures and electron impact cross sections of calcium and ytterbium. Assuming a discharge length of $l \simeq 2\,\mathrm{cm}$ and an ionization cross section of $\sigma_i \approx 5\,\text{Å}^2$, the minimum atomic densities required for calcium and ytterbium are $\sim 3.7 \cdot 10^{18}$ atoms/m^3 and $\sim 1.7 \cdot 10^{18}$ atoms/m^3, respectively.

When fulfilling the density requirements for a self-sustaining discharge, it is necessary to account for the density profile along the axis of the aperture – the beam density outside of the oven will be appreciably lower than $n_0 = p/k_BT$ as the vapor freely expands into the vacuum chamber. This topic is addressed by Pauly and the density along the axis of a singular capillary is shown in Figure 4.7. Note the significant drop in density along the axis (and particularly after the exit) of the channel. The oven must consequently be operated at sufficiently high temperatures such that the density of the vapor *outside* the oven meets the density requirements of the discharge.

Thus far, we have primarily addressed ionization collisions in the glow discharge due to their relevance to the ionization cascade. Of significantly greater import to this experiment are the inelastic collisions present in the discharge that result in the production of excited atoms, some of which will be in the metastable ^3P_J states. Since ionization from the ground state requires greater energy than any excitation process and since the ionization and excitation cross sections are finite over a range of electron energies (see Figure 4.8), there will be a significant density of excited atoms resulting in the emission of radiation according to the allowed transitions in Table 3.2 [167]. The cascade of ionization collisions in the discharge is merely a means of exponentially increasing the number of electrons in the discharge that may undergo inelastic excitation collisions with atoms to appreciably populate the metastable states in calcium and ytterbium.

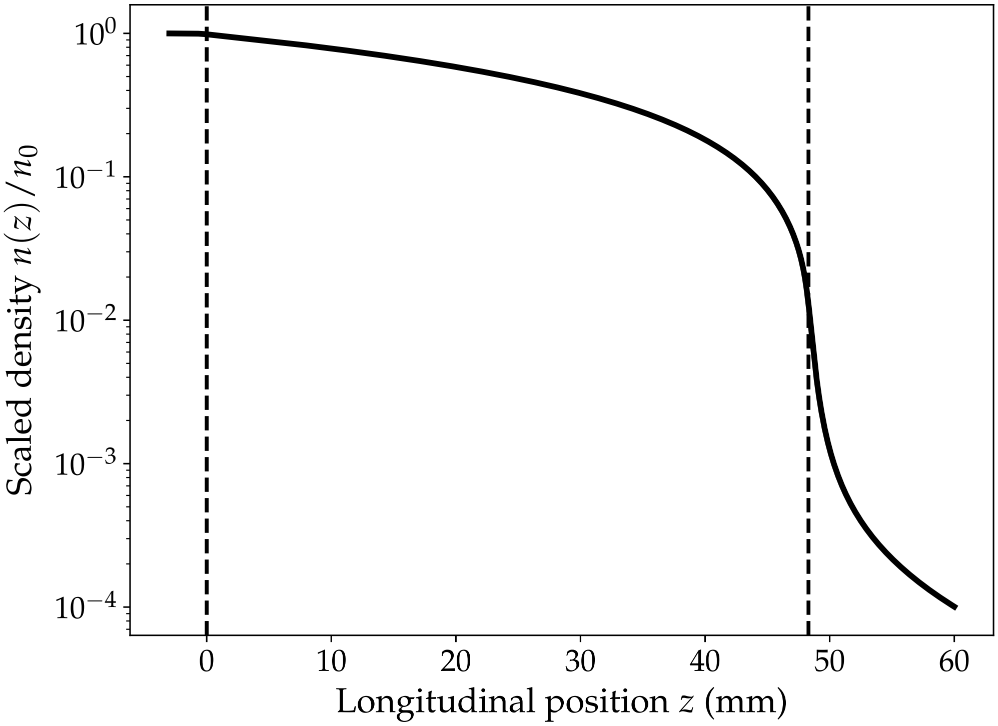

Figure 4.7: Longitudinal density profile along the axis of a single capillary with diameter $2r = 1.14\,\mathrm{mm}$ and length $L = 48.3\,\mathrm{mm}$. The density has been scaled by the density within the reservoir, n_0. The entrance and exit of the channel correspond to $z = 0$ and $z = L$, respectively. The discharge region extends to approximately 2 cm beyond the oven exit.

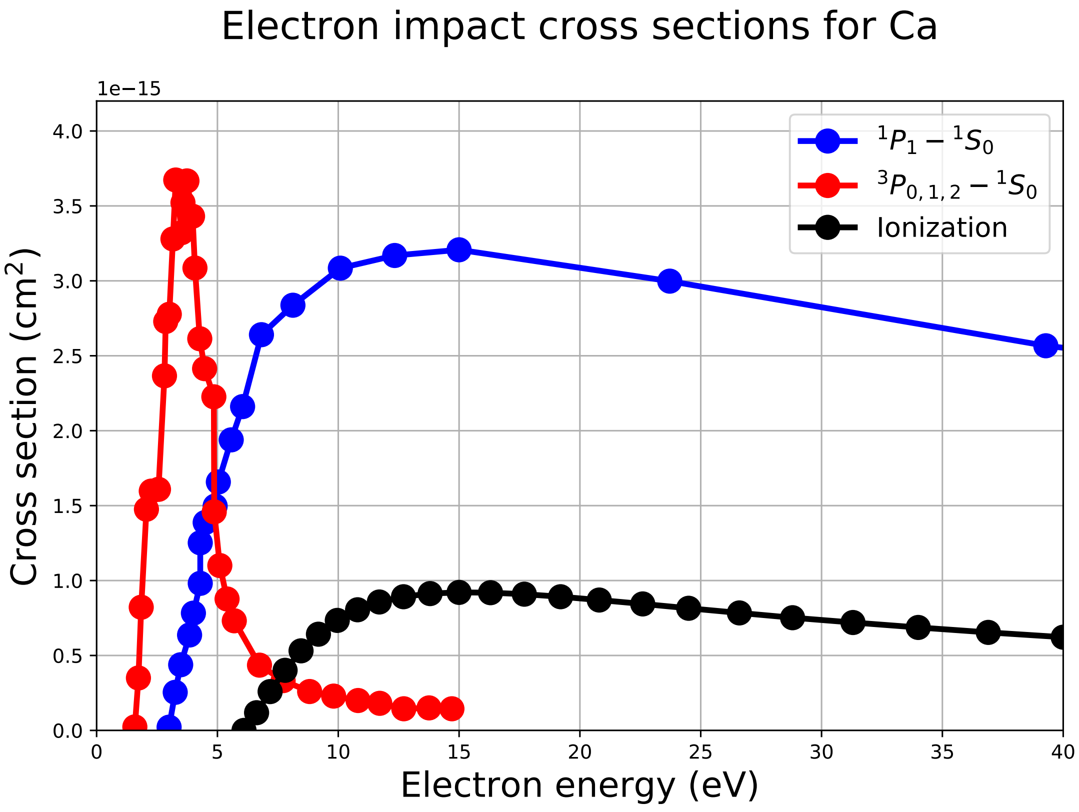

Figure 4.8: Electron impact cross sections for the ionization and excitation of calcium to the ^3P_J and $^1P_1$ states. Data from [12].

All excited states produced in the discharge will ultimately decay after some finite lifetime given by Equation 3.4 through spontaneous emission. The intensity of the emitted spectral lines is proportional to the Einstein A coefficient for the transition; consolidating Equations 3.2 and 4.8 yields [161]

$$I_{ki} = A_{ki} h \nu_{ki} n \left(\frac{g_k}{Z} \right) \exp(-E_k / k_B T), \tag{4.14}$$

where n is the atom number density in the discharge region. Naturally, the discharge emission spectra will be subject to various broadening mechanisms (i.e., Doppler and pressure broadening) [169]. However, the bandwidths of the bandpass optical filters used in analyzing the emission spectra (see Section 5.2) are sufficiently broad (in excess of 1 THz) such that broadening mechanisms need not be considered here.

Figure 4.8 shows data for the ionization and excitation electron impact cross-sections in calcium[4]. Unsurprisingly, the three curves peak in an order of increasing energy. In order to create an ionization avalanche in a self-sustaining glow discharge, a substantial fraction of electrons from the cathode must be able to attain energies in excess of the ionization energy of the atom. As the cross-sections in Figure 4.8 are finite and overlap for a range of electron energies, it is no surprise that in the discharge for both calcium and ytterbium, the population of the $^1P_1$ and ^3P_J states occur in tandem with ionization. The cross-section for excitation to the ^3D_J states in calcium is not known but these states may be populated by

---

[4] Similar data is not known for yttterbium but is assumed to be qualitatively similar.

direct excitation from lower lying states or through de-excitation of higher lying states [170].

Before describing the design of the DC electric discharge used in the experiment, it is necessary to address the effect of electron-atom collisions in the discharge on the atomic beam angular and velocity distributions (Equation 4.4). The forward scattering of electrons traveling axially with respect to the atomic beam will simply result in a small longitudinal momentum transfer to the atom. Likewise, in the event that the electron is scattered through some finite angle, the atom will acquire a transverse momentum kick. The latter case will consequently cause deviations from the expectations in Figure 4.4 and increase the angular spread of the beam, albeit by a small amount. This was found to be the case by Rundel, who reported a 1.4° increase in the full-width half-maximum in the angular distribution of their metastable noble gas beam as a result of electron-atom collisions in the discharge [170]. Lastly, the velocity distribution of the atomic beam following the discharge will be shifted toward higher velocities as slower atoms will sustain greater angular deflections than faster atoms and effectively be more strongly attenuated [170, 171].

4.2.1 Design considerations

The hollow-cathode discharge scheme used in this experiment for populating the metastable ${}^3P_J$ states was initially based off of the design given in [168, 172]. A longitudinal discharge (i.e. one wherein the discharge electrodes are coaxial with the atomic beam) was chosen over a transverse discharge since, in the latter, greater transverse momentum would inevitably be imparted on the atomic beam in the discharge region [171].

The discharge consists of a toroidal tungsten cathode placed within 1 cm of the nozzle opening and a stainless steel plate with an enlarged triangular bore placed about $1 - 2\,\mathrm{cm}$ away from the cathode as shown in Figure 4.5. Several hollow-cathode discharges incorporate a coaxial solenoid to enhance the metastable atom production efficiency in the discharge [168, 172]. The solenoid accomplishes this by focusing the electrons onto the atomic beam along funnel-like trajectories to augment the probability of electron-atom collisions [173]. We decided to forgo the solenoid due to the unnecessary practical complications it presented for achieving the reported metastable production efficiencies of $\sim 50\%$, which are needlessly high for the purposes of this experiment.

The toroidal tungsten cathode was made by winding a 0.01"-diameter tungsten wire around a 2-56 screw, rendering a helix which was then bent into a torus and expanded to an appropriate diameter of $\approx 1.5\,\mathrm{cm}$. The cathode was positioned immediately downstream from the oven opening and held in place by insulating ceramic rods on a crane-like structure[5]. After assembly and under an appropriate vacuum, it is critical that the cathode be slowly heated over a timespan of a few minutes in order to relieve internal stress resulting from the winding process [174]. Rapid heating consistently resulted in an elaborate warping of the cathode causing it to frequently short on the oven or some other grounded surface.

---

[5] Alumina rods with two bores from McMaster-Carr. Part no.: 87175K71

The cathode functioned as a source of both thermionic and secondary electrons. As mentioned before, the secondary electrons are a result of impinging ions formed in the discharge. Thermionic electrons are emitted from the cathode surface when heated to a high temperature – the electron analog of the thermionic emission of ions in surface ionization [91, 175]. The current density J of emitted thermionic electrons is dependent on the temperature T and, not surprisingly, the work function Φ of the metal surface

$$J(T) = A\,T^2 e^{-\Phi/k_B T}. \tag{4.15}$$

Equation 4.15 is known as Richardson's Law and $A = 4\pi e m k_B^2/h^3 = 1.2 \times 10^6$ A/m^{2}K^2 is the Richardson constant. In the event of an external field (sufficiently low so that *field* emission of electrons may be neglected), Equation 4.15 may be modified by a Schottky term akin to Section 2.3 [29]. The work function is highly sensitive to impurities, defects, and crystallographic orientation (see Sections 2.1 an d2.2). This sensitivity be readily exploited to enhance the thermionic current density, such as by using a thoriated tungsten wire [105] or coating the cathode with alkaline earth oxides [172]. For ytterbium, a pure tungsten cathode was sufficient for igniting the discharge; in the case of calcium, the cathode as a source of thermionic electrons was unnecessary and the external electric field was sufficient for sustaining a glow discharge.

An 80% transmission stainless steel mesh was spot welded over the anode opening in order to achieve a more uniform electric field. The anode was attached to the front face of the oven via 5 cm long 2-56 threaded rods anchored to the protruding holes in Figure 4.6. The anode was electrically isolated from the grounded rods by a combination of ceramic tubes and shoulder washers[6]. After sufficiently long operation times, substantial quantities of metal vapor would accumulate on the ceramic washers, inevitably compromising the the electrical isolation of the anode. Preceding complete shorting of the anode, sporadic flashes (ostensibly with wavelengths of 423 nm in calcium and 556 nm for ytterbium) could be seen in the vicinity of the ceramic washers due to the rapid resistive heating of a deficient connection between the anode and the grounded rods. The high operating temperature required to produce a self-sustaining glow discharge in ytterbium resulted in a flux of atoms exceeding $\sim 1 \times 10^{20}$ atoms/s and an angular spread appreciably greater than that for an effusive beam (Figure 4.4). Consequently, this quickly (within thirty minutes) undermined the electrical isolation of the anode so we decided to remove it entirely, relying on the toroidal hot cathode alone to ignite the discharge with the front face of the oven effectively acting as a grounded anode.

A final point regarding the design of the discharge: because we are exclusively interested in the metastable states that are populated as a byproduct of the ionization avalanche in the glow discharge, beyond the discharge region, the ions in the plasma must be extracted out of the atomic beam. In failing to do so, a considerable fraction of ions and electrons from the discharge will impinge on the surface ionization detector and manifest as an erroneous ion current that would mask any current of surface ions created at the detector. Therefore, we installed a pair of transverse parallel plates a few centimeters downstream from the discharge to filter out any charged particles emanating from the discharge (see Figure 4.1).

---

[6] Alumina shoulder washers purchased from thermoshield.us. Part no.: 11052-1030.

4.3 Surface ionization detector

The surface ionization detector used in this experiment was based on the designs outlined in previous work [30, 47]. As shown in Figure 4.9, the surface ionization detector consists of a ~ 2.75" long, 0.01" diameter tungsten wire (also referred to as a hot wire). It is spot-welded between two molybdenum tags, one of which is extendable via a bend at its center to accommodate any expansion in the tungsten wire during heating. The hot wire is encased in and electrically isolated from a collector machined out of a stainless steel tube (OD 0.75") with a 2.50" x 0.375" rectangular cut along its body to allow the atomic beam to be deposited onto the hot wire. Machined macor parts are used to electrically isolate the collector and hot wire from the detector frame. The frame interfaces with a linear actuator[7] for centering the detector within the chamber. An electrical lead is anchored to the collector via a copper clamp bolted on to the outside of the collector.

The collector is grounded through an ammeter and the power supply connected to the hot wire can be floated to $\pm 50\,\mathrm{V}$ to appropriately bias the hot wire (i.e., negatively biased for detecting thermionic electrons for work function measurements and positively biased for detecting surface ions). The frame of the detector is composed of four 0.125" stainless steel rods parallel to the hot wire and anchored to the top and bottom plates. Three stainless steel plates from previous designs are attached to the frame in order to confine the radiative heating of the

---

[7] MDC Vacuum. Part no.: 660004.

hot wire.

As with the toroidal tungsten cathode used to ignite the discharge, the hot wire also warrants slow initial heating. The extendable tag described above must also be initially slightly extended at room temperature. If that is not the case, any force resulting from the thermal expansion of the hot wire will be insufficient to compress the (relatively rigid) tag, causing the hot wire to warp and bend. In accordance with Sections 2.1 and 2.2, the hot wire must be heated for a sufficiently long time (e.g. four to five hours) to purge the surface of the hot wire of impurities.

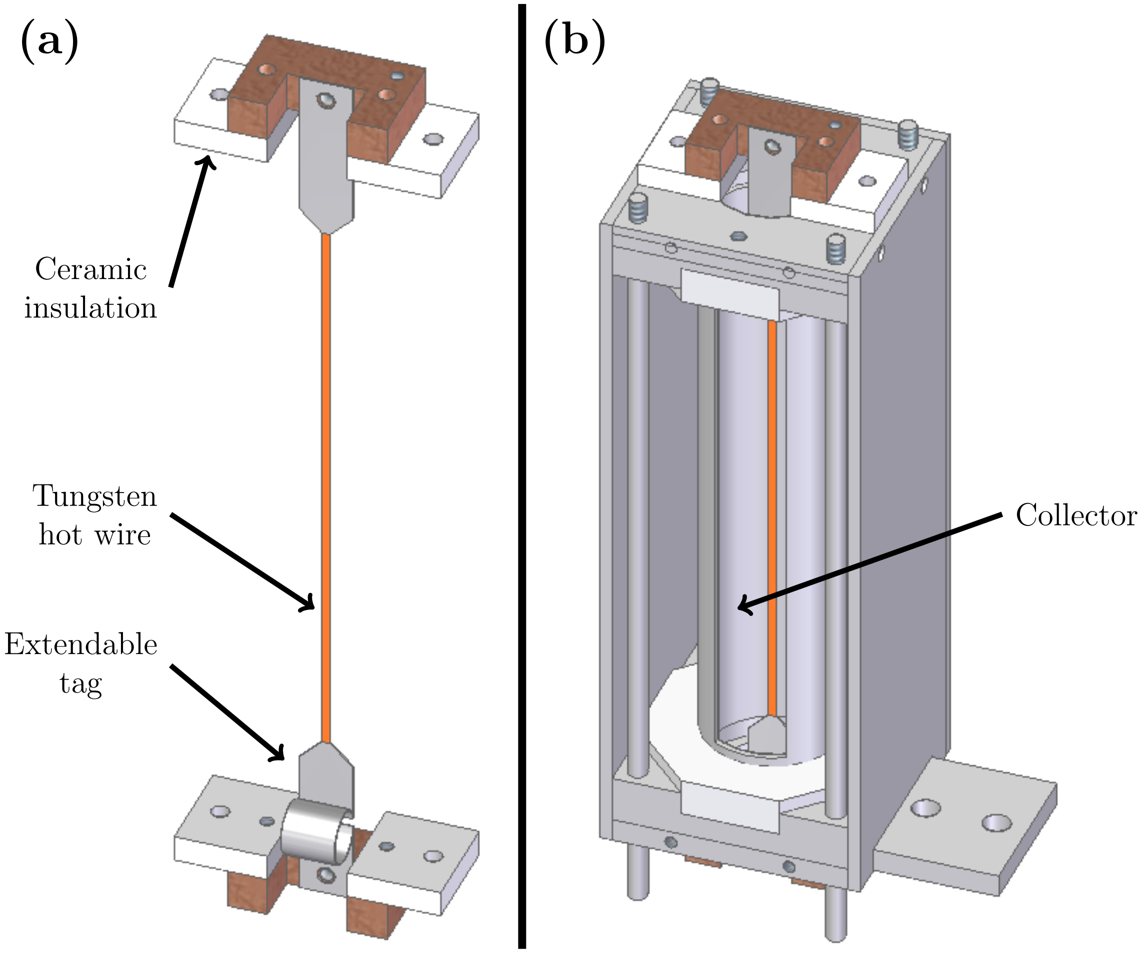

Figure 4.9: (a) Bare tungsten hot wire and (b) the fully assembled surface ionization detector. The tungsten hot wire is spot welded onto two molybdenum tags, one of which is extendable to sustain any change in strain resulting from the thermal expansion of the hot wire. The hot wire is encased in a cylindrical stainless steel collector with a rectangular opening in the front to allow the atomic beam to impinge on the hot wire. Three copper clamps (not shown) are attached to each tag and the collector to anchor wires connected to electrical feedthroughs. Custom-machined macor ceramic parts were used to isolate the hot wire and collector from the grounded frame.

Chapter 5

Results

5.1 Quantifying the atomic flux at the surface ionization detector

The physical requirements for producing a self-sustaining discharge required us to operate our oven at temperatures no less than 650 °C producing atomic beams not strictly in the effusive regime discussed in Section 4.1. This was particularly true for ytterbium, as it has a shorter mean free path than calcium. In the transitional/opaque regime, the total flux of atoms emanating from the oven may still be described by Equation 4.3 [11]. However, this regime is characterized by atomic beams with greater angular spreads and centerline intensities that vary in proportion to the Knudsen number. Since the surface ionization detector is placed in the center of the atomic beam, it is necessary to properly quantify the total flux of atoms impinging on the hot wire.

We proceeded to measure the atomic beam intensity at the position of the surface ionization detector by measuring the vapor deposition rates with a quartz crystal thickness monitor[1] This sensor applies a radiofrequency voltage across the quartz crystal at a frequency equivalent to its resonance frequency (approximately

---

[1] We used a deposition rate/thickness sensor, quartz crystal, and STM-2 transducer from INFICON. See `https://www.inficon.com/`.

6 MHz for an unused crystal). The sensor monitors the decrease in resonance frequency as mass accumulates on the exposed face of the crystal during deposition:

$$\frac{m_f}{m_q} = -c\frac{\Delta\nu}{\nu_q}, \tag{5.1}$$

where m_f is the mass of the accumulated film, m_q is the mass of the quartz crystal, $\Delta\nu = \nu_q - \nu_f$ is the change in resonance frequency throughout deposition, ν_q is the initial resonance frequency, and c is a proportionality constant [176]. With some simple substitutions, we can derive an expression relating the film thickness, T_f, to the change in resonance frequency:

$$T_f = \frac{K\Delta\nu}{\rho_f}, \tag{5.2}$$

where ρ_f is the density of the film and K is a tabulated proportionality factor. However, Equation 5.2 is found to be inaccurate for frequency changes exceeding a 2% drop in ν_q and additional work regarding oscillating quartz crystals yielded a more accurate equation relating the film thickness to the resonance frequency [176, 177]:

$$T_f = \left(\frac{N_{at}\rho_q}{\pi\rho_f\nu_f Z}\right)\arctan\left(Z\tan\left[\frac{\pi\Delta\nu}{\nu_q}\right]\right), \tag{5.3}$$

where $N_{at} = 1.661 \times 10^5\,\mathrm{Hz\,cm}$ is a frequency constant of these quartz crystals, $\rho_q = 2.649\,\mathrm{g/cm^3}$ is the crystal density, and Z is a tabulated parameter that is film-specific [178]. For calcium, $\rho_f = 1.54\,\mathrm{g/cm^3}$ and $Z = 2.620$. For ytterbium, $\rho_f = 6.97\,\mathrm{g/cm^3}$ and $Z = 1.130$.

Since the parameter N_{at} is temperature-dependent and the frequency measurements are sensitive to temperature gradients across the crystal surface, we regulated the thickness monitor temperature with a chiller set to 7 °C. We limited the length of the water cooling lines to $\sim 1\,\mathrm{m}$ and insulated them with foam cladding to minimize heating.

We mounted the thickness monitor on a 2.75" CF bellows affixed on a translation stage with a 5 cm range to enable us to translate the thickness monitor across the atomic beam. Since the diameter of the thickness monitor sensor is 8.27 mm, we attached an aluminum aperture with a 1 mm-diameter hole onto the sensor to improve our spatial resolution. Using a shutter consisting of a plate attached to a rotary feedthrough on a lateral half-nipple, we were able to further control the deposition process. As we translated the thickness monitor across the atomic beam, we collected deposition data at various locations for 5 min. Such data for calcium using an array of 28 capillaries with diameter $2r = 1.14\,\mathrm{mm}$ and length $L = 48.3\,\mathrm{mm}$ is shown in Figure 5.1. The black line in the figure represents the angular distribution of an atomic beam effusing from a singular opening channel with the same dimensions of one capillary. The red-dashed distribution corresponds to the best fit to the data, which resembles the angular distribution of a singular channel with a diameter to length ratio of $2r/L = 0.082$. Effectively, as anticipated in Section 4.1, operating the calcium source in the transitional/opaque regime at 650 °C produces an atomic beam with the centerline intensity and angular distribution of an effusive beam emanating from a channel with a near 3.5-fold increase in radius or decrease in length.

We performed similar flux measurements using the thickness monitor on the ytterbium beam. As in calcium, we placed the thickness monitor at the location

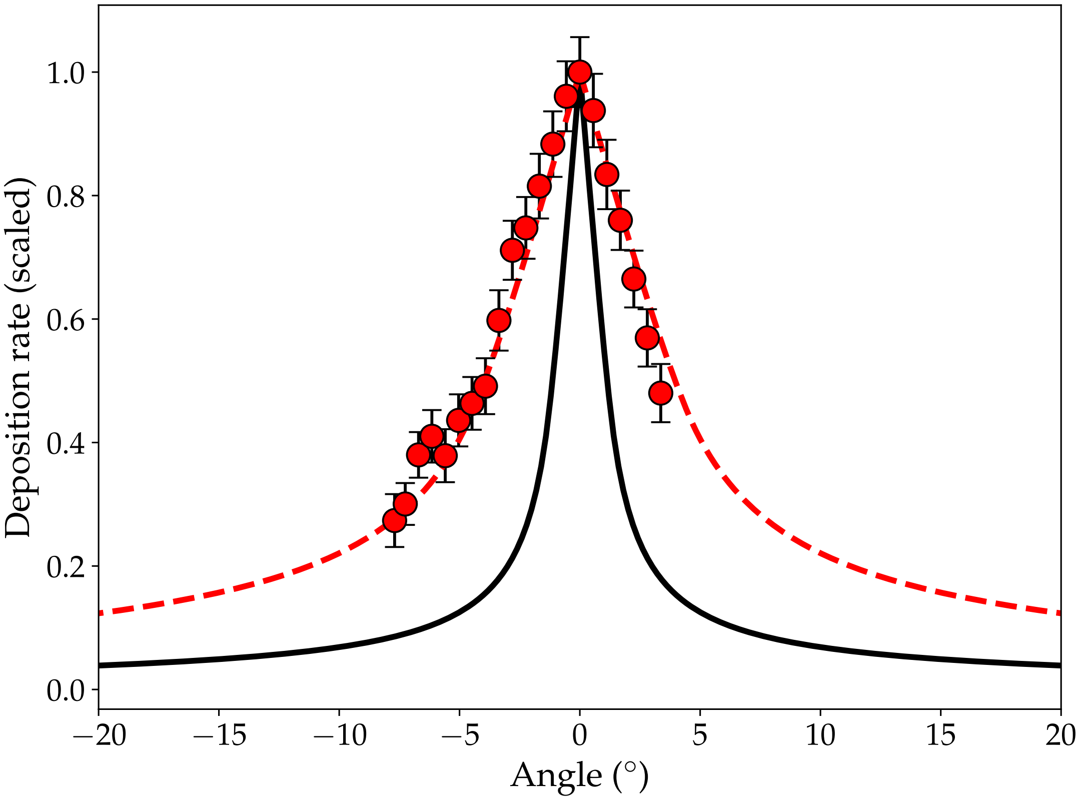

Figure 5.1: Angular distribution of the calcium atomic beam at the position of the surface ionization detector. The oven reservoir temperature was stabilized at 650 °C. Deposition rate data was collected at various transverse positions with a quartz crystal thickness monitor. The error bars denote the standard error in the deposition rate over a time span of five minutes. The black distribution corresponds to the anticipated angular distribution of an effusive beam emanating from a single channel with the diameter $2r = 1.14\,\mathrm{mm}$ and length $L = 48.3\,\mathrm{mm}$ of the capillaries used in Section 4.1.2. The red-dashed distribution is a best fit to the data using the expressions for the angular distribution of an effusive source outlined in [11]. The discrepancy between the black and red-dashed distributions can be attributed to two reasons: (a) the black distribution corresponds to that of a single channel whereas twenty eight capillaries were used, and (b) the oven was operated at a high temperature, where the increased rate of inter-atomic collisions has the effect of virtually reducing the channel length and broadening the angular distribution [11]. All curves were scaled to have a centerline intensity of unity.

of the surface ionization detector, $\sim$ 33 cm downstream from the oven opening, and exposed it to the atomic beam. Possibly due to the high vapor pressure (1.4 Torr) in the oven at a reservoir temperature of 650 °C, the high deposition rate on the sensor manifested as a nonlinear frequency response over time. During the deposition process, the calculated deposition rate from Equation 5.3 was not constant and the measured oscillation frequency was nonlinear. This anomalous behavior in the sensor is most clearly shown in Figure 5.2 for an unused crystal and with the 1 mm aperture removed. Two anomalies are immediately apparent and more easily seen in the deposition rate measurements. First, the deposition rate is not constant, as we would expect it to be for an oven at equilibrium (note that the oven temperature had equilibrated at 650 °C when we opened the shutter to expose the sensor to the beam, which manifested as an initial spike in the deposition rate data), but instead drops steadily. Second, there is a precipitous drop in the deposition rate after about thirteen hours of continuous deposition. It may be that at this point, the sensor had accumulated an excessive amount of mass that that compromised its accuracy.

The final thickness reading from the thickness monitor was 1884 nm for the data in Figure 5.2. Following the deposition, we used a microscope to directly measure the thickness of the deposited film to compare it to the calculated thickness from the sensor. Largely for convenience and at no detrimental cost to precision, we opted to use an optical microscope (in contrast to, say, an atomic force microscope)[2] to measure the final thickness of the film deposited over the 8.27 mm-diameter

---

[2] We used a 3D laser scanning confocal microscope from Keyence. See `www.keyence.com`.

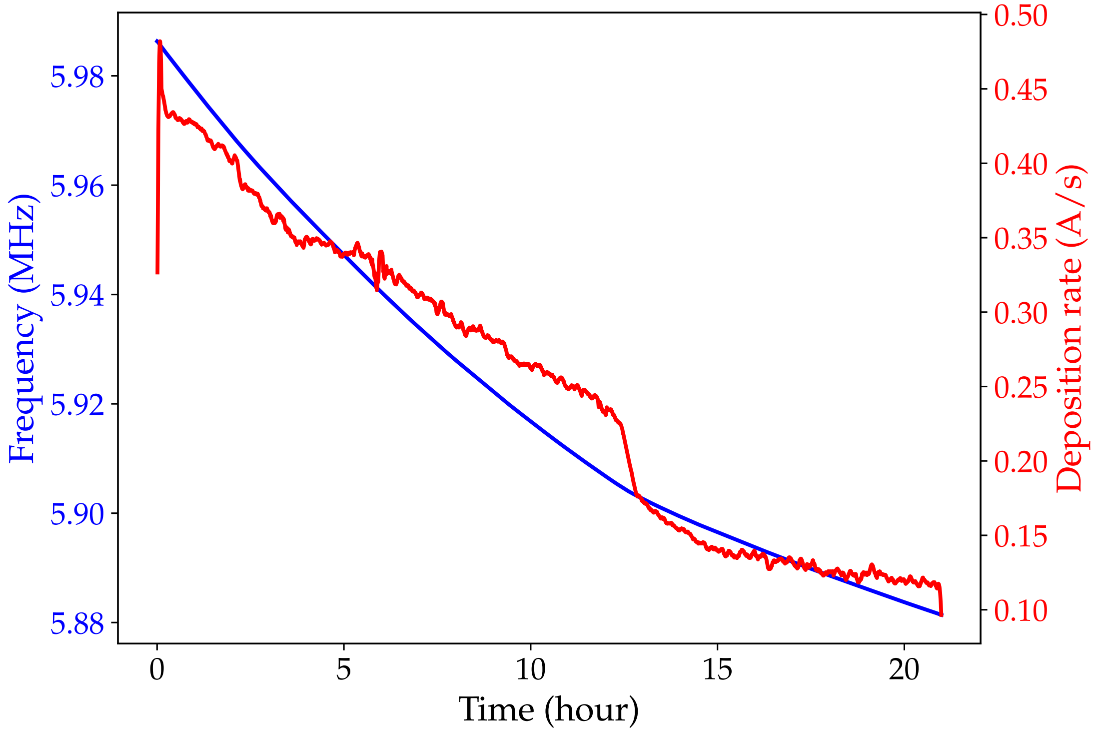

Figure 5.2: Change in oscillation frequency and deposition rate for a quartz crystal thickness monitor exposed to the ytterbium beam.

active area of the crystal. Due to the high flux of atoms at this location and the aforementioned oven temperature, the film deposited onto the crystal was fairly rough (see Section 5.2.2 for more details), but was measured to have an average thickness of $1568 \pm 1\,\mathrm{nm}$, a near 20% difference from the calculated thickness of the sensor. Naturally, it is the microscope measurement of the thickness that is the most reliable due to the anomalies exhibited in the thickness monitor data.

With the dimensions measured by the optical microscope, it is evident that over the nearly twenty one hours of ytterbium deposition, the total number of atoms deposited on the quartz crystal is on the order of 10^{18}. This low number and is readily attributable to the fact that at an oven temperature of 650 °C, the flow is far from effusive. With a mean free path of $\sim 0.1\,\mu\mathrm{m}$ and a Knudsen number on the order of 0.001, the beam is highly collisional – we can expect an exceptionally broad angular distribution and a small fraction of the total flux in the centerline. Under these conditions, it is difficult to accurately assess the fraction of total atoms incident on the surface ionization detector. Furthermore, it is also nontrivial to estimate the total flux of atoms emanating from the oven at this temperature due to the outsized effect of interatomic collisions on the flow – all that may be expected is a decrease in intensity and a broadening of the beam [11]. Equation 4.3 is no longer applicable in this regime as the flow may no longer be described within the framework of a molecular model. Due to the atypical dimensions and geometry of our source, it is nontrivial to accurately model its flow and additional work must be done to rigorously quantify the angular distribution of the beam and its flux.

5.2 Quantifying the population of the ^3P_J states

Recall the properties of the ^3P_J states, namely their lifetimes, as addressed in Section 3.2.2. Since the lifetime of the intercombination $^3P_1 \rightarrow {}^1S_0$ transition decreases for increasing atomic mass, it is sufficiently long (and can therefore be considered metastable) in calcium for a sufficient fraction of the $^3P_1$ atoms to survive the transit to the surface ionization detector. This is not the case in ytterbium, where the lifetime of the transition is 5.5 µs and essentially all of the ytterbium atoms in the $^3P_1$ state can be expected to decay before impinging on the surface ionization detector. Therefore, the metastable states targeted in the discharge region are specifically the $^3P_{0,1,2}$ states in calcium and the $^3P_{0,2}$ states in ytterbium. These states can be expected to be populated in relative proportions according to their statistical weights.

Quantifying the fraction of atoms exiting the discharge region in the ^3P_J states can be accomplished most rigorously by using a laser, say to measure its absorption when tuned to a transition between the metastable triplet and another triplet state, such as the 610.2 nm $^3P_0 \leftrightarrow {}^3S_1$ transition in calcium [172]. This would yield the total number of $^3P_0$ atoms, x, and the rest may be found according to their statistical weights: $3x$ and $5x$. In lieu of a laser, observing the fluorescence of the intercombination transition (specifically $^3P_1 \rightarrow {}^1S_0$) would be an adequate measurement of the number of $^3P_1$ atoms, and the remaining metastable atoms may be calculated as in the absorption measurements [168]. This is possible for ytterbium, where the intercombination transition is sufficiently short-lived and of a distinct green, 555.8 nm wavelength, enabling it to be easily observed in the discharge region. Can the fluorescence of the intercombination transition in calcium be detected as well? In short, this is theoretically possible after extending the vacuum chamber to accommodate the long transition lifetime. We indeed attempted to detect this fluorescence signal but since the oven and filament are housed in the main chamber, they contributed a significant background in the red wavelengths due to their high temperatures that occluded the detection of a weak, diffuse 657.4 nm signal. Certainly further modifications to the set-up could have been implemented to enable this fluorescence measurement, but a much more expedient option was to detect the decay of the $4s4d\,^3D_J$ triplet to the metastable $4s4p$ ^3P_J states in the $442-446$ nm range (see Figure 3.2). These decays have ~ 100 ns lifetimes as they are electric dipole allowed transitions and should be visible at the oven opening. This fluorescence signal will give an estimate for the total number of ^3P_J calcium atoms. Note that some finite amount of calcium atoms will be in the metastable $^1D_2$ state following the discharge and since its excitation energy exceeds that of the ^3P_J triplet, it too will undergo surface ionization. Quantifying the fraction of atoms in this state is necessary for any sort of estimate of the surface ionization efficiency of metastable atoms. However, doing so is non-trivial given its long 2 ms lifetime and without a 5.5 µm laser to drain these atoms through the $^1P_1$ state to the ground state, they too will undergo surface ionization along with the ^3P_J atoms.

In the case of ytterbium, this situation is greatly simplified given the greater linewidth and shorter wavelength of the intercombination transition, both properties that enhance its signal to noise ratio. Since the $^3P_1$ state decays at a rate of $1.1 \times 10^6\,\mathrm{s}^{-1}$ this transition is visible in the discharge region [134]. Given the 1:3:5 multiplicity of the ${}^3P_J$ triplet, quantifying the number of ytterbium atoms decaying from the ${}^3P_1$ state by measuring the intensity of the 555.8 nm signal is an indirect way of determining the number of atoms remaining in the metastable ${}^3P_{0,2}$ states.

5.2.1 Calcium

At oven temperature above 650 °C, the calcium vapor pressure is above approximately 0.05 Torr and the calculated total flux of atoms out of the oven is approximately 2×10^{17} atoms/s. At these conditions, the atomic beam density is a few orders of magnitude less than that of the calcium vapor in the reservoir (see Figure 4.7) but sufficient, nonetheless, to meet the density requirement in Equation 4.13 for a self-sustaining glow discharge. Indeed, above reservoir temperatures of 650 °C, a glow discharge could readily and consistently be ignited solely by raising the voltage on the anode. That is, a *hot* cathode was neither necessary nor sufficient for producing the discharge, though it certainly intensified the fluorescence from the discharge when heated to produce thermionic electrons. The 423 nm fluorescence signal from the decay of the ${}^1P_1$ singlet state could be easily seen by eye in the discharge region as shown in Figure 5.3B, first forming within $\sim$ 1 mm of the capillaries and then spreading to encompass the volume shown in the figure at higher anode voltages.

The set-up for detecting the ${}^3D_J \rightarrow {}^3P_J$ transitions in calcium is shown in Figure 5.3. Two different power supplies separately powered the filament and both

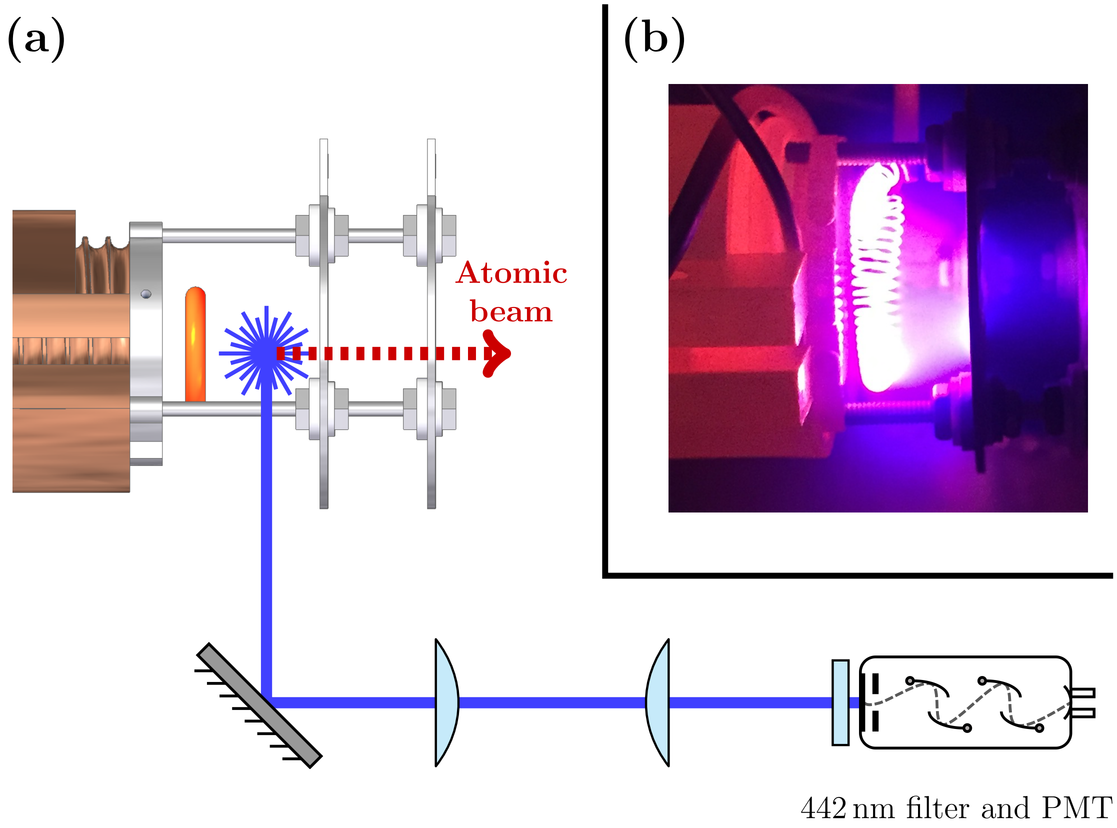

Figure 5.3: (a) The setup for detecting the ${}^3D_J \rightarrow {}^3P_J$ transitions in calcium with wavelengths in the $442-445$ nm range. A series of mirrors and planoconvex lenses were used to image the fluorescence signal from the discharge onto a PMT. A bandpass filter centered around 442 nm from Edmund Optics was used to extract the relevant signal. (b) A photo of the calcium discharge under normal operating conditions (oven reservoir at a temperature of 673 °C). The orange blackbody glow of the oven nozzle is seen on the left and the radiation from the cathode ($\gtrsim$ 1500 °C) saturated the camera. Note that the violet fluorescence is predominantly from 423 nm decay of the singlet ${}^1P_1$ transition to the ground state.

discharge plates[3]. We imaged the discharge plasma directly onto a photomultiplier tube (PMT)[4] and used a bandpass filter centered at 442 nm with a pass band of 10 nm to extract the signal from these transitions[5].

With the oven at a normal operating temperature of approximately 650 °C, the emission of the $^1P_1$ and ^3D_J decays (of which, only the former was visible by eye due to the higher density of atoms that were directly excited to the $^1P_1$ state) in calcium could only be detected when the voltage on the discharge plates exceeded about $\sim 15\,\mathrm{V}$ and was never detected as a result of the emission of thermionic electrons from the filament alone[6]. Effectively, the anode plates were necessary and sufficient for igniting the discharge and the ensuing glow was amplified by the filament. Data exemplifying this concerning the $442 - 446\,\mathrm{nm}$ decay of the ^3D_J states is shown in Figure 5.4.

The raw signal at the PMT was converted to the number of total photons emitted at various voltages on the discharge plate by considering the PMT detection efficiency at this wavelength and the solid angle of the emission captured by the detection system, which was limited by the first planoconvex lens (focal length $f = 250\,\mathrm{mm}$, diameter 50.8 mm, distance 229 mm) at 0.04 sr. At these temperatures, the total flux of atoms given by Equation 4.3 is approximately

---

[3] The high voltage power supply used to bias the anodes was RA60-1.5P from Matsusada Precision. See `https://www.matsusada.com/pdf/ra_rb.pdf`.

[4] PMT from Hamamatsu. Part no.: R212.

[5] Bandpass filter from Edmund Optics. Part no.: 65-684.

[6] Presumably a glow discharge may have also been visible at these conditions had the filament been floated at a voltage of $\sim 15\,\mathrm{V}$. However, one terminal of the filament was always grounded for consistency.

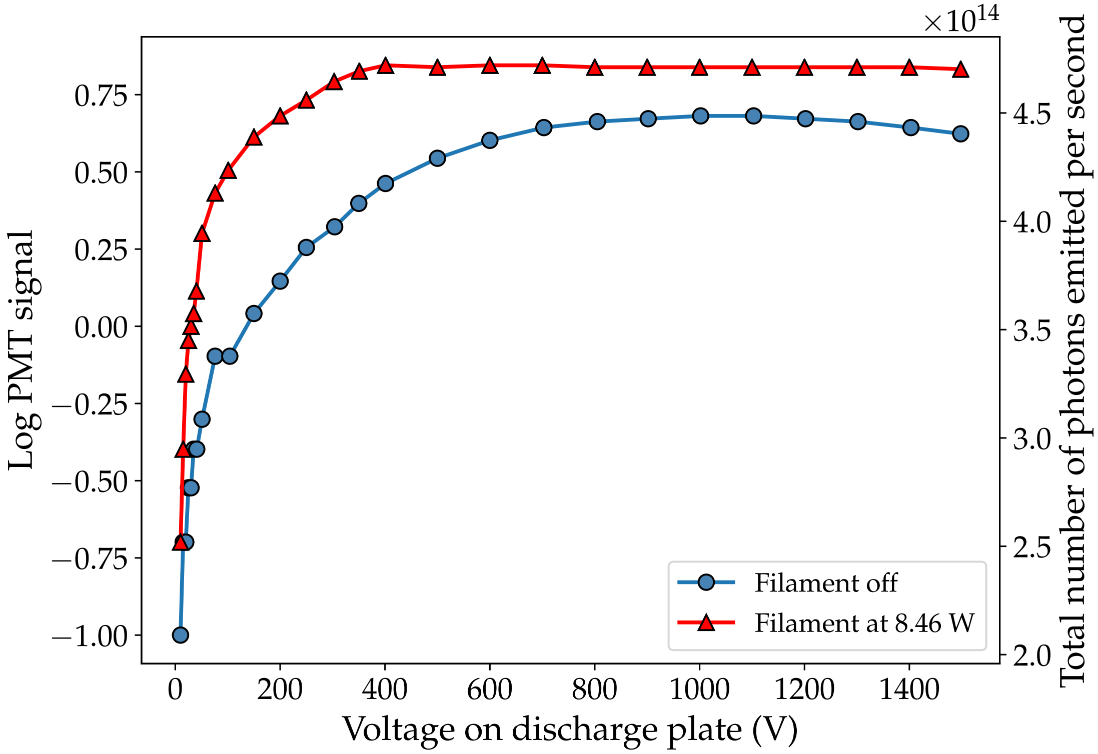

Figure 5.4: Fluorescence signal from the $442 - 446\,\mathrm{nm}$ decay of the ^3D_J states. The saturation in the signal that occurs at around $500\,\mathrm{V}$ is likely a consequence of the $40\,\mathrm{mA}$ current limit on the power supply used to bias the anode. For these measurements, the oven reservoir temperature was about $660\,^\circ\mathrm{C}$.

2×10^{17} atoms/s, implying that, depending on the filament, approximately 0.24% of atoms undergo the ${}^3D_J \rightarrow {}^3P_J$ transitions. Considering this low fraction, it is highly unlikely that atoms undergo these transitions multiple times. Nevertheless, this is assuredly an underestimate of the total number of metastable atoms produced by the discharge as not all ${}^3P_J$ atoms undergo a decay from the higher lying ${}^3D_J$ states and some unknown fraction of atoms may be in the metastable singlet ${}^1D_2$ state (see Section 3.2.2).

5.2.2 Ytterbium

For ytterbium, the oven was operated at a temperature of 650 °C, producing a ytterbium vapor pressure greater than 1.3 Torr and a total flux no greater than 1×10^{18} atoms/s. No self-sustaining glow discharge was visible under any circumstances for temperatures below this limit. Since the ytterbium mean free path under these conditions is less than $\sim 0.1\,\mathrm{mm}$, the oven was operating far from the effusive regime and, in contrast to calcium, we decided to forgo use of the capillaries from Section 4.1 to facilitate the loading process since they were no longer providing a meaningful enhancement to the collimation of the atomic beam. Furthermore, due to the high ytterbium flux, any attempted effort to electrically isolate the discharge anode from the grounded oven was ultimately in vain as the isolating ceramics were fully coated with metal vapor within thirty minutes of operation. In the end, the toroidal tungsten cathode was sufficient for igniting the ytterbium discharge, a photo of which is shown in Figure 5.5(b).

Since the rate of spontaneous emission of the ${}^3P_1$ in ytterbium is substan-

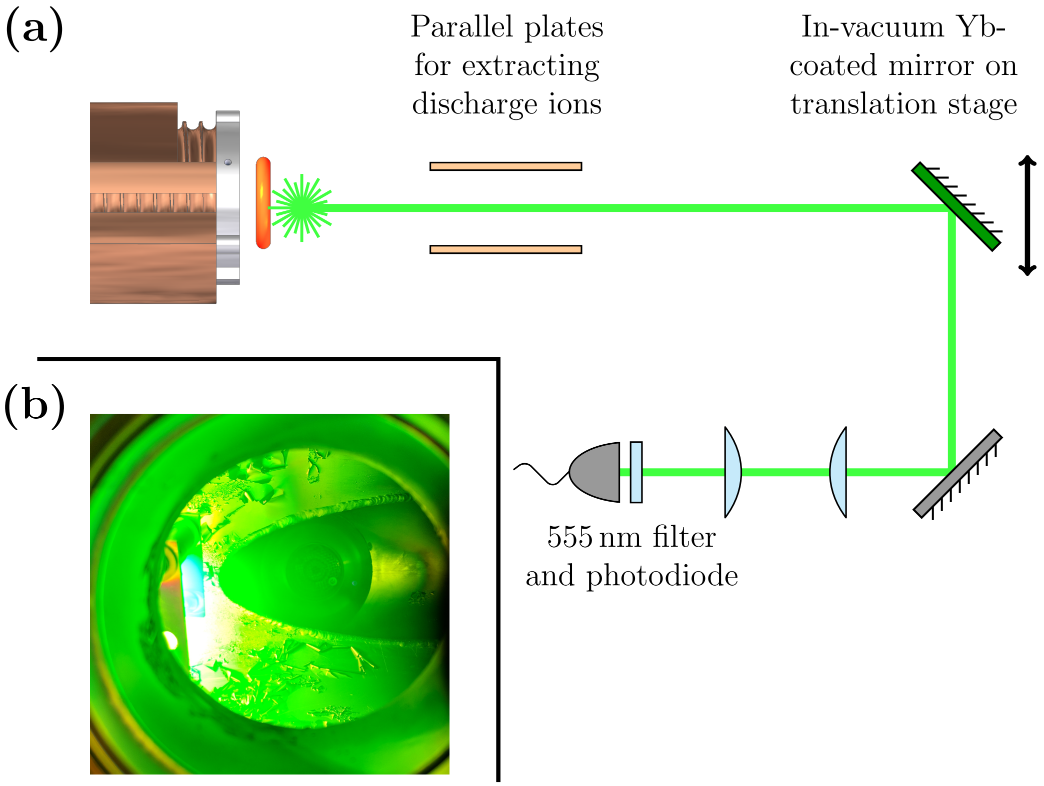

Figure 5.5: (a) The set-up for detecting the $^3P_1 \rightarrow {}^1S_0$ transition in ytterbium with a wavelength of 555.8 nm. A series of mirrors and planoconvex lenses were used to image the fluorescence signal from the discharge onto a photodiode, where the ytterbium-coated mirror is denoted in green. The ytterbium mirror was mounted on a translation stage so that it may be moved in vacuum perpendicularly to the beam to facilitate alignment. A bandpass filter centered around 556 nm from Semrock was used to extract the relevant signal. (b) A picture of an intense ytterbium discharge at an elevated oven temperature (oven reservoir at approximately 715 °C) taken a few minutes before the viewport became completely coated. Under normal operating temperatures, the discharge glow discharge did not exceed a volume of $\sim 1\,\mathrm{cm}^3$. Note the blue fluorescence near the parallel plates of what is presumed to be the decay of the $^1P_1$ state.

tially higher than that in calcium (see Table 3.4), measuring the intensity of the 555.8 nm intercombination line in ytterbium would be the most direct method for quantifying the number of metastable $^3P_{0,2}$ atoms produced in the discharge. The set-up for detecting the 555.8 nm fluorescence from the ytterbium discharge is shown in Figure 5.5(a) and utilizes a bandpass filter centered at 554 nm with a band width of 23 nm[7]. The discharge was imaged onto a photodiode[8] with a series of mirrors and lenses.

Due to the high ytterbium flux at these temperatures, lateral view ports on the vacuum chamber in the vicinity of the oven became noticeably coated by metal vapor within several minutes[9]. Accordingly, we placed a 1" silvered mirror at 45° with respect to the atomic beam 82 cm downstream from the discharge on a homemade translation stage. This enabled us to direct a fraction of the 555.8 nm signal through a view port sufficiently far from the discharge to not be exposed to any metal vapor. Naturally, as it is at the center of the atomic beam, the mirror was directly exposed to the ytterbium vapor and sustained a drop in reflectivity at this wavelength once it was fully coated. The solid angle subtended by the optical set-up was limited by the ytterbium-coated mirror to 0.024 sr.

In order to produce a functional ytterbium mirror, it is necessary that the metal vapor flux at the mirror be sufficiently low to produce a smooth surface. We found that with the oven at 650 °C, the ytterbium vapor deposition rate on a

---

[7] Bandpass filter from Semrock, `semrock.com`. Part no.: FF01-554/23-25.

[8] Photodiode from Thorlabs. Part no.: PDA100A.

[9] Sections of the view ports without line-of-sight to the oven opening also became rapidly coated due to the augmented angular spread in the beam from collisions within the discharge.

silvered mirror positioned 50 cm downstream (the position of the surface ionization detector in Figure 4.1) was too high, resulting in a rough ytterbium surface and poor reflectivity [179]. This was immediately apparent as the signal of the blackbody radiation of the filament continuously and incessantly dropped to nearly the background level throughout the deposition process. The ytterbium film on the mirror was visibly rough. Lowering the deposition rate by decreasing the oven temperature was not a viable option since the atomic beam density would have been too low to support a self-sustaining discharge. The simplest alternative was to move the mirror 82 cm downstream from the oven. At this position, the mirror remained fully exposed to the ytterbium vapor and maintained specular reflection at 45°. Once fully coated after a few hours, it exhibited a constant drop in reflectivity. We were able to quantify this change in reflectivity by measuring the intensity of the blackbody radiation of the cathode over a range of temperatures through the bandpass filter before and about four hours after being exposed to the ytterbium beam, both with the oven off so as not to ignite the discharge. This data is shown in Figure 5.6.

Prior to exposure to the ytterbium beam, the silvered mirror had a reflectance of 96.27% at 555.8 nm for a 45° angle of incidence[10]. Following the ytterbium deposition, the reflectance dropped to 0.265 the initial value, giving the ytterbium mirror a modest reflectivity of 25.5±0.1% in the range of wavelengths within the passband of the filter.

---

[10] Protected silver mirror from Thorlabs. Part no: PF10-03-P01.

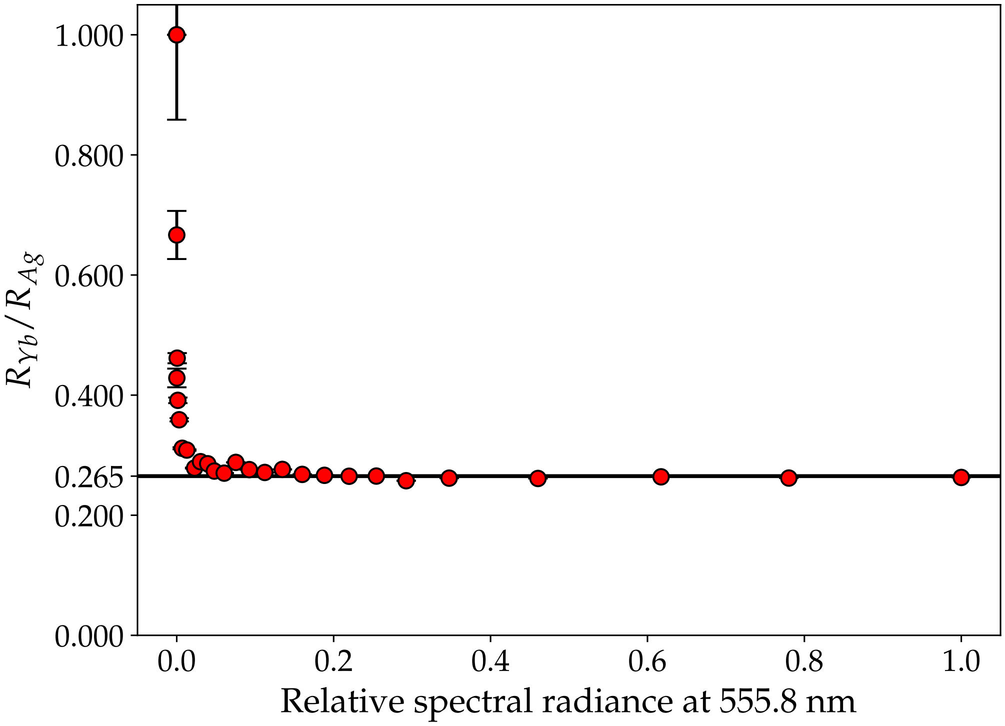

Figure 5.6: Change in reflectivity before and after ytterbium deposition. The tungsten filament in the discharge was used as an approximate blackbody radiation source for measuring the reflectivity of the mirror. The relative spectral radiance was calculated at $\lambda = 555.8\,\text{nm}$ assuming an ideal blackbody for various filament temperatures, as calculated from Equation 5.7.

Once the reflectivity of the ytterbium mirror had been firmly established, we quantified the intensity of the 555.8 nm fluorescence signal from the discharge using the same set-up as described above. Naturally, the parallel plates used to extract ions from the beam were biased to a potential difference of 3 kV to control for any effect they may have on the intensity of the discharge. After subtracting the background radiation signal from the oven and filament, the fluorescence signal of the decay of the $^3P_1$ state is shown in Figure 5.7. The total number of photons (on the order of 10^{13}) was calculated in a similar manner as in Figure 5.4 – the captured solid angle of 0.024 sr was determined by the ytterbium-coated mirror within the vacuum chamber and the total transmission of all the optics used to detect the ytterbium discharge was 17.5%. For the reasons outlined at the end of Section 5.1, it is difficult to determine what fraction of atoms undergo this transition since the flow is far from effusive and Equation 4.3 is invalid under these conditions.

5.3 Surface ionization of metastable atoms

5.3.1 Tungsten work function measurement

When addressing the principles of surface ionization in Chapter 2, we addressed the exponential dependence of the probability of ionization on the work function, Φ, of the metal surface. In the same chapter, we also considered the dependence of the work function on the crystal orientation of the surface and, more importantly, on the presence of adsorbates (of which O_2 has the strongest effect) and impurities within the metal that diffuse to the surface (namely, alkaline and alkaline earth impurities). The polycrystalline tungsten used as an ionizing surface

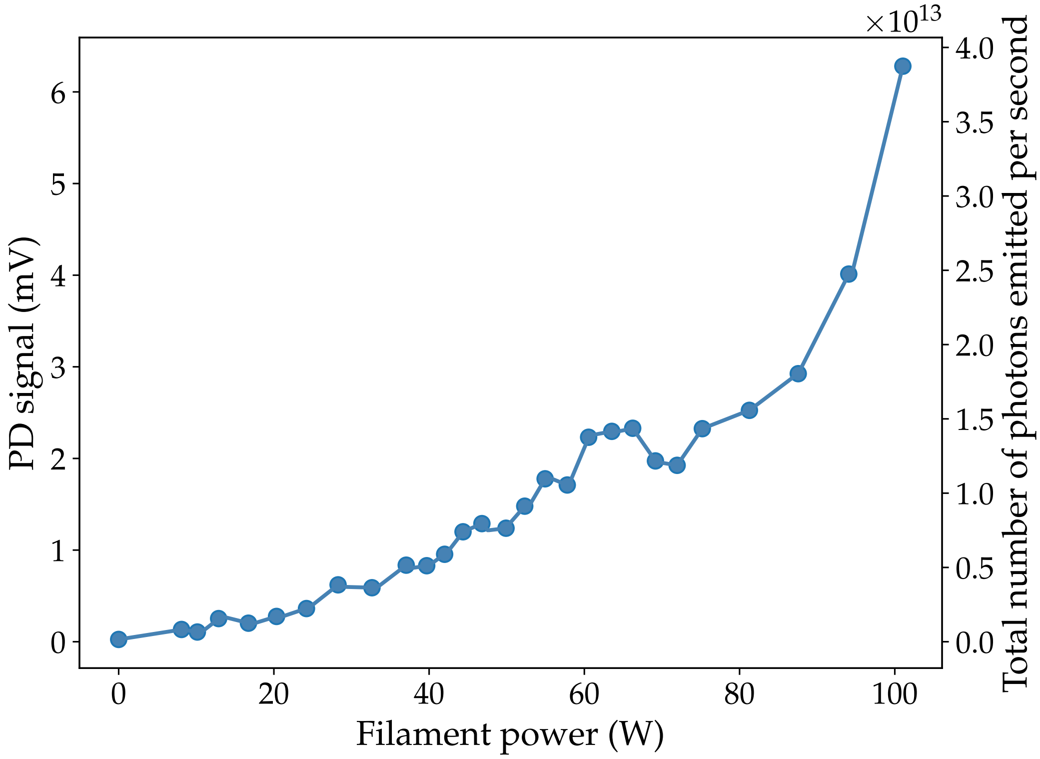

Figure 5.7: Fluorescence signal from the 555.8 nm decay of the $^3P_1$ state in ytterbium. Considering the multiplicity of the ^3P_J states, the number of atoms undergoing this transition is equal to half the number of atoms remaining in the metastable $^3P_{0,2}$ states.

in this experiment is expected to have a work function of 4.54 eV [90]. Ground state calcium and ytterbium atoms have ionization energies greater than this value (6.11 eV and 6.25 eV, respectively) and metastable triplet states with sufficiently low ionization energies (~ 4.22 eV and ~ 4.02 eV, respectively). According to the elemental theory of surface ionization on a hot polycrystalline tungsten surface, we may anticipate that impinging metastable atoms will evaporate predominantly as ions, while incident ground state atoms will remain neutral following desorption. This expectation is grounded on the validity of the assumption that the polycrystalline tungsten work function is approximately 4.54 eV.

During normal operation[11], the pressure within the vacuum chamber is typically on the order of 10^{-6} Torr. Recalling the Hertz-Knudsen equation in Section 2.1, a monolayer of adsorbates will form on a metal surface within 1 s. Should oxygen be one of these adsorbates, the magnitude of the work function of the ionizing tungsten surface may increase by as much as 1.9 eV (see Table 2.1). This would be detrimental, as it would imply that ground state calcium and ytterbium atoms may undergo surface ionization at appreciable rates and comparable to those of the metastable atoms, thereby rendering this experiment futile. On the other hand, should the tungsten hot wire in the surface ionization detector be insufficiently purged of most alkaline and alkaline earth impurities, its local work function may too change drastically, decreasing by about 2.5 eV, wherein we would expect the degree of ionization (Equation 2.6) for metastable and ground state atoms alike to be negligibly small, again rending the experiment

---

[11] An oven temperature $\geq 650\,^{\circ}$C and a discharge cathode temperature $\gtrsim 2000\,^{\circ}$C

ineffective at investigating the surface ionization mechanisms of metastable atoms.

The effect on the work function resulting from impurities can be readily mitigated by purging the metal at a high temperature for a long duration prior to running the experiment (see Equation 2.12). Regarding the effect on the work function due to oxygenation, the background pressure must be sufficiently low and the ionizing hot wire must be operated at an adequately high temperature to suppress the long-term effects of oxygen adsorption. To verify that this is indeed the case and that the work function of the tungsten used for surface ionization in this experiment is suitable for investigating the surface ionization of metastable calcium and ytterbium atoms, I will address measurements we performed of the hot wire work function in this section.

The reported measurements of the tungsten work function in Table 2.2 were performed through a variety of means, namely by measuring the current of emitted electrons over a range of temperatures (thermionic emission) or electric field (field emission). Measuring the work function is markedly simpler through thermionic emission, wherein the current density of emitted electrons is governed by Richardson's Law [29, 91]:

$$J(T) = AT^2 e^{-\Phi/k_B T}, \tag{5.4}$$

where $A = 1.2 \times 10^6\,\mathrm{A/m^2K^2}$ is a constant defined when we first encountered thermionic emission in Equation 4.15 when considering sources of electrons in the discharge. An external electric field is incorporated in to Richardson's Law as it was for the Saha-Langmuir equation in Section 2.3 [29]:

$$J(T) = AT^2 \exp\left(-\frac{\Phi}{k_B T}\right) \exp\left(\frac{e}{k_B T}\sqrt{\frac{eF}{4\pi\epsilon_0}}\right). \tag{5.5}$$

A final point of significance concerns the accumulation of a negative space charge in the volume surrounding the cathode (i.e., the hot wire is the cathode and the cylindrical connector is the anode, as it pertains to this section alone). If this accumulated charge is too great, it will impede the flow of electrons from the cathode to the anode, resulting in a diminished current at the anode. To mitigate this issue, it is crucial that the potential difference between the electrodes be sufficiently great to overcome the potential imposed on thermionic electrons by the space charge. In the space-charge-limited regime, the current density at the anode J_A varies according to the three halves power of the anode voltage V_A, as stated in Child's Law [180]:

$$J_A = \frac{4\epsilon_0}{9d^2}\sqrt{\frac{2e}{m}}V_A^{3/2}, \tag{5.6}$$

where d is the distance between the electrodes and m is the electron mass. As the anode potential is increased for a fixed cathode temperature, J_A will eventually saturate at a value predicted by Richardson's Law.

Richardson's Law provides a method for determining the work function of the polycrystalline tungsten used in this experiment. The tungsten wire is resistively heated by a direct current and floated to a fixed negative voltage $V_{\text{float}} = -100\,\text{V}$. The collector anode is grounded through an ammeter to measure the current of thermionic electrons emitted from the hot wire at high temperatures. We calibrated the temperature of the hot wire with an optical pyrometer[12] through the 35° half-nipple shown in Figure 4.1, though this proved to be a more cumbersome and ultimately less precise and consistent method of measuring the temperature than observing the change in resistance with respect to temperature, which we may linearly approximate as:

$$R(T) = R_0(1 + \alpha(T - T_0)), \tag{5.7}$$

where R_0 is the hot wire resistance at room temperature T_0 and α is an empirical parameter. For tungsten, a linear fit to the resistivity data up to 3655 K indicates that $\alpha = 5.924 \times 10^{-3}\,\mathrm{K}^{-1}$ [121].

The work function of the cathode can be readily calculated from the data of the thermionic electron current at various temperatures. As was done by Kawano et. al., this is typically done by plotting $\ln(J/T^2)$ against $1/T$ in a "Richardson" plot [90]:

$$J = A'T^2 \exp\left(-\frac{\Phi}{k_B T}\right) \tag{5.8}$$

$$\ln\left(\frac{J}{T^2}\right) = \ln(A') - \frac{\Phi}{k_B T}, \tag{5.9}$$

wherein the work function may be determined by the slope of the line. In the analysis above, I have incorporated the electric field component of Equation 5.5 resulting from the static floating voltage of −100 V of the hot wire into the prefactor, A'. Certainly, there is some minimal temperature dependence within the Richardson constant A and it has been absorbed into A'; however, it will suffice to

---

[12] Cyclops C100L from AMETEK-Land. See `https://www.ametek-land.com`

consider A' as constant since the external field is relatively small and its contribution in Equation 5.5 is insignificant. Note that the field must be sufficiently large to mitigate the effects of space charge, but small enough so that the contributions of field emission of electrons to the current density can be neglected – this criterion can be readily satisfied since the onset of field emission does not occur until fields on the order of 10^8 V/m [36, 37, 38].

Data concerning the thermionic emission of electrons from a polycrystalline tungsten wire was collected with the detector in Section 4.3 and is shown in Figure 5.8. A linear fit to the data for temperatures below 1700 K indicated that, for this temperature range, the work function of the tungsten hot wire is 5.18 ± 0.03 eV. This elevation in the work function from the accepted value of 4.54 eV is likely a result of oxidation. If a purely clean tungsten surface is desired, Kaminsky recommends flash heating the filament to approximately 3000 K to purge the surface of oxides and other contaminants [29]. Likewise, Kawano reports virtually no oxidation while operating a rhenium wire at temperatures exceeding 2000 K [90].

5.3.2 Calcium

To summarize, the set-up for investigating the surface ionization of metastable calcium is shown in its entirety in Figure 4.1. At a reservoir temperature of 660 °C, the oven produces a thermal beam of calcium atoms, which are then bombarded by electrons in a hollow cathode discharge and some fraction is excited to the metastable ${}^3P_J$ triplet, as shown in Figure 5.4. Crucially, the discharge also produces a number of ions which are filtered out of the atomic beam by a pair of

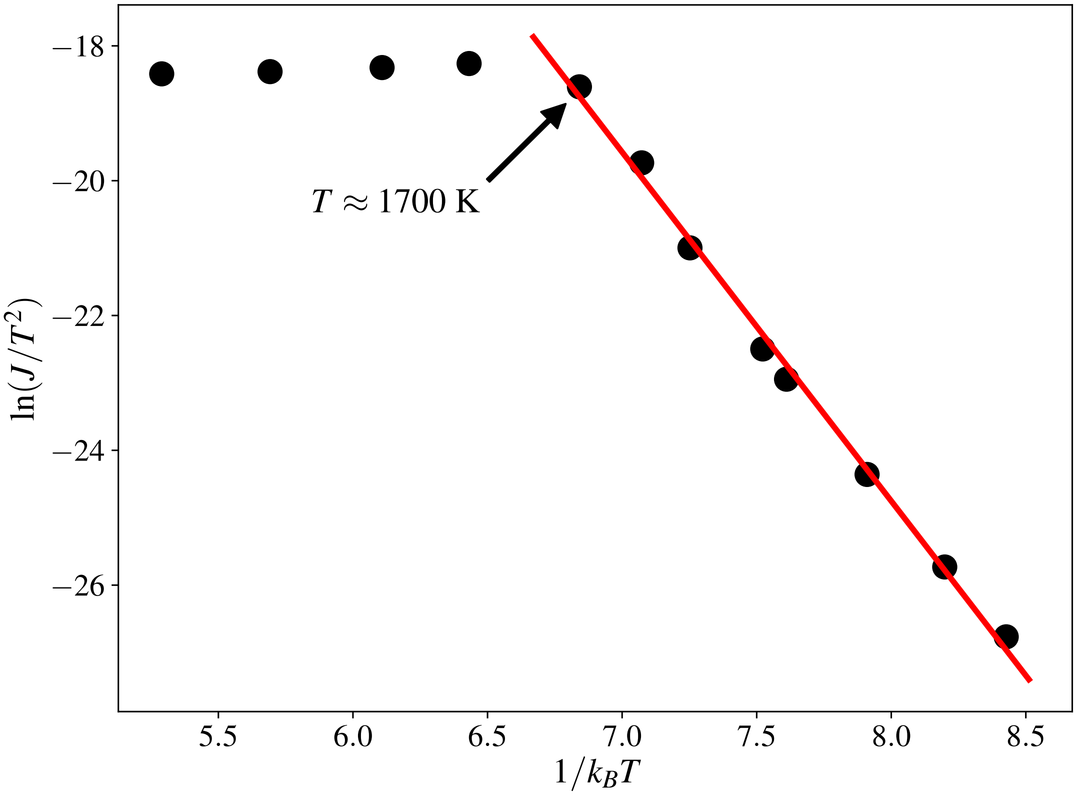

Figure 5.8: Thermionic emission data from a polycrystalline tungsten wire. The value of the work function inferred from the slope of the linear fit to the data shown in red is $5.18 \pm 0.03\,\mathrm{eV}$. Above a temperature of 1700 K, the thermionic electron current at the detector is clearly space-charge limited. Space-charge effects may be further mitigated by increasing the potential difference between the cathode (hot wire) and anode (collector) beyond the 100 V used in this experiment.

parallel plates transverse to the atomic beam. The beam then impinges on a surface ionization detector with a tungsten hot wire (with a work function of about 5.18 eV) and an ion collector that is floated at $-10\,\mathrm{V}$ with respect to the hot wire. The hot wire is baked at near $\sim 2000\,\mathrm{K}$ for approximately four hours to purge the surface of foreign adsorbates and any defects within the wire, particularly alkali metal impurities. Any ions that may be formed on the hot wire surface will be evaporated and attracted toward the collector, thereby generating a current that we measure using a low noise transimpedance amplifier[13]. The transimpedance amplifier subsequently generates a voltage signal with a gain of 10^8 V/A, enabling us to measure the output with a multimeter.

We proceeded to determine whether metastable calcium atoms are surface ionized in two ways. First, we modulated the voltage on the discharge anode while maintaining a constant electric field of $\sim 200\,\mathrm{V/mm}$ between the transverse ion repulsion plates. This allowed us to vary the fraction of metastable atoms in the beam, as shown in Figure 5.4, while extracting all the ions produced as a byproduct in the discharge. This data is shown in Figure 5.9

Second, we modulated the potential difference on the ion repulsion parallel plates with the anode voltage maintained at 1 kV and the filament heated by 8.46 W. Doing this serves as proof that the current at the surface ionization detector is due to surface ions originating at the tungsten surface and not stray ions created at the discharge. This data is shown in Figure 5.10

---

[13] Purchased from Femto. Part no.: DLPCA-200. See `www.femto.de/en/products/`.

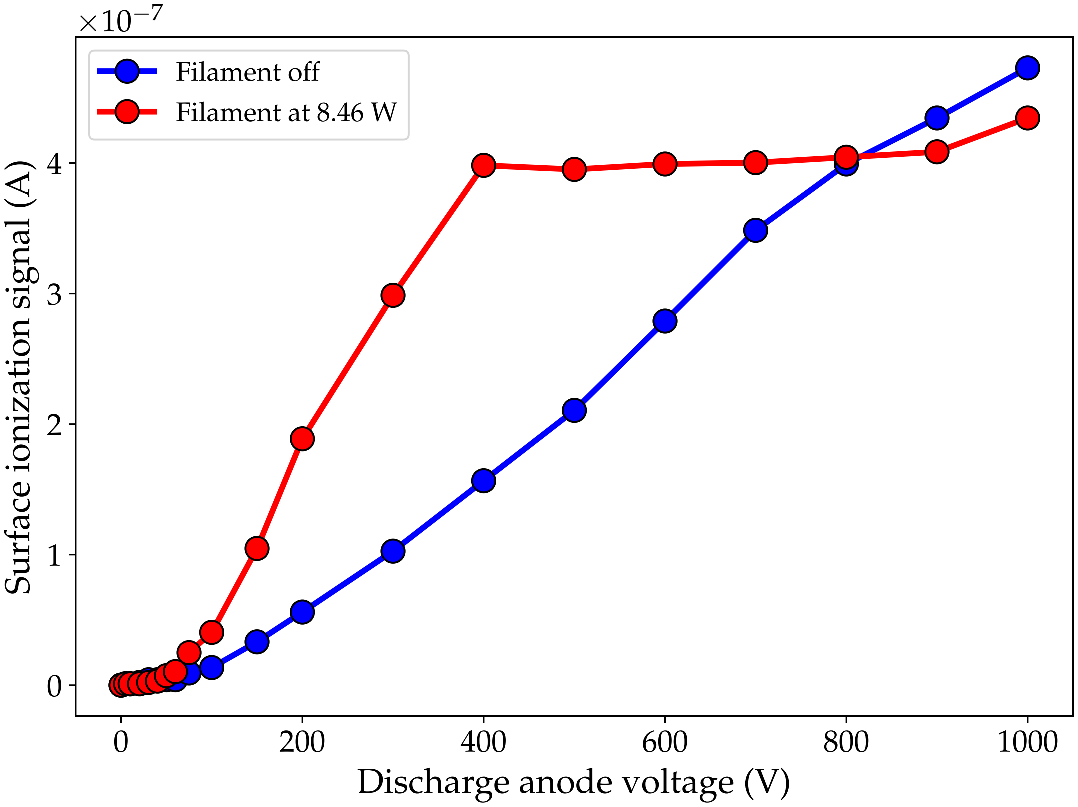

Figure 5.9: Surface ionization signal of metastable calcium on tungsten at various discharge anode voltages. Not surprisingly, when the filament (discharge cathode) is heated by 8.46 W, we see a saturation in the surface ion signal at an anode voltage of 400 V and above – the same threshold for saturation seen in Figure 5.4. It is unclear as to why the blue curve exceeds the red at a high anode voltage.

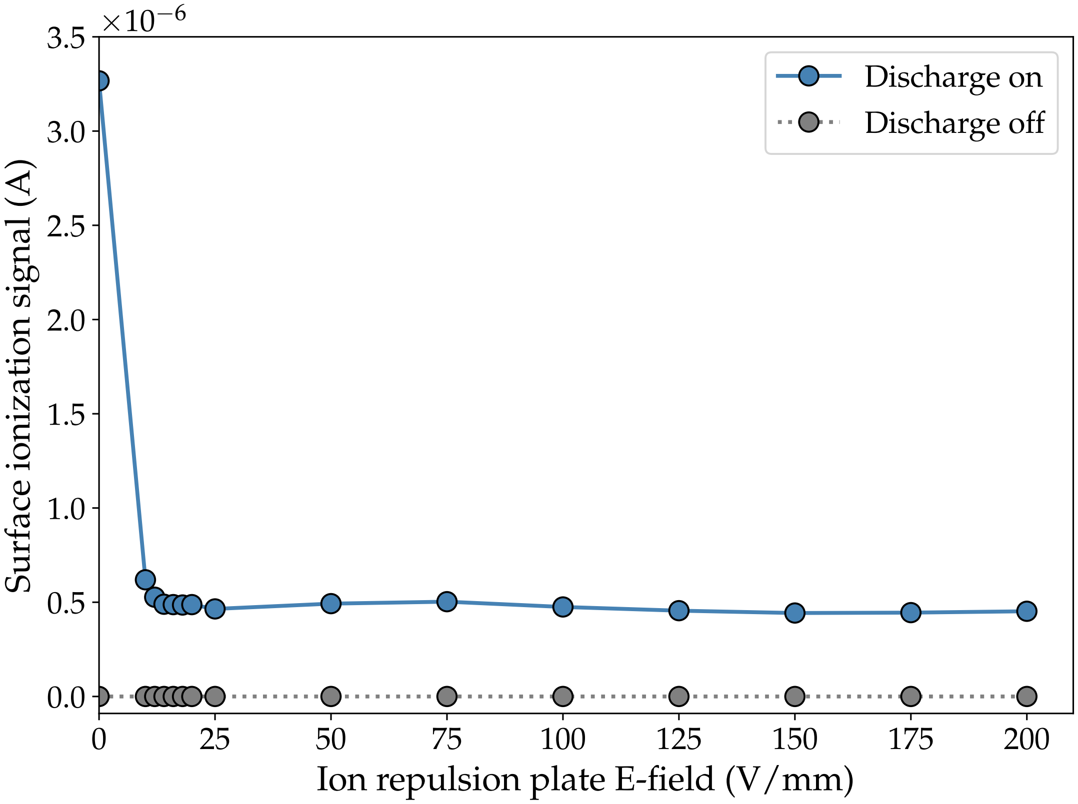

Figure 5.10: Ion signal at the surface ionization detector at various values of the electric field between the ion repulsion parallel plates with the discharge anode at 1 kV and 8.46 W through the filament. Under these conditions, we expect both metastable atoms and ions to be created in the discharge region. At a field of zero, the ions created in the discharge are able to strike the surface ionization detector.

5.3.3 Ytterbium

The set-up for investigating the surface ionization of metastable ytterbium is shown in Figure 4.1. However, the anodes used for calcium had to be removed as they were rapidly shorted to the grounded oven by the high flux of ytterbium vapor at the operating temperature of 650 °C. As outlined in Section 5.2.2, the only means by which we were able to modulate the number of metastable atoms was by resistively changing the temperature of the discharge cathode. Heating the tungsten cathode leads to thermionic emission of electrons, which are accelerated by the electric field of the cathode into the atomic beam. As in calcium, this electron bombardment in the discharge excites a fraction of the total atoms to the ^3P_J triplet, of which a third rapidly decay through the $^3P_1 \rightarrow {}^1S_0$ channel and emit light at 555.8 nm. The remaining metastable $^3P_{0,2}$ atoms propagate down the chamber, in the direction of the surface ionization detector. Using ion repulsion plates similar to those used for calcium, we applied a transverse electric field of nearly 100 V/mm to extract any free electrons and ions from the beam.

In contrast to the calcium surface ionization measurements in the previous section, we used a picoammeter[14] to directly measure the current at the surface ionization collector. The hot wire was cleaned at a temperature of nearly 2000 K for five hours before these measurements. We floated the hot wire at +25 V with respect to the collector and resistively heated it up to $\sim$ 1750 K. At various hot wire temperatures, we modulated the power through the discharge cathode to

---

[14] Picoammeter from Tektronix, formerly Keithley. Part no.: 6485. See `www.tek.com`.

change the number of metastable atoms in the beam and detected ion signals such as those shown in Figure 5.11.

Surface ionization data collected over a range of discharge intensities at various hot wire temperatures exhibits a consistent onset in the ion signal above $\sim 51\,\mathrm{W}$ in the discharge cathode. Considering the fluorescence data in Figure 5.7, a sudden ion onset is unexpected and likely indicates that our detection system is insensitive at lower ion currents.

A DC background signal was present in the ion data that was independent of the discharge intensity. This signal was subtracted from the data and was shown to vary according to the hot wire temperature. A likely explanation for the hot wire temperature dependence of the background is inadequate cleaning of the hot wire, despite the fact it was baked at nearly $2000\,\mathrm{K}$ for several hours prior to these measurements. It is reassuring, nonetheless, to see that the ion signal is independent of the hot wire temperature, as we would expect from the principles of surface ionization in the case that $I < \Phi$. The fact that we do not see an exponentially rising ion signal, as we did for the fluorescence signal in Figure 5.7, is likely due to the insensitivity of our measurement system for currents much lower than $10\,\mathrm{nA}$. Future generations of this experiment will employ a more sensitive ion detector, such as a channel electron multiplier [48].

5.4 Conclusions

In this chapter, it has been demonstrated that our hollow cathode discharge can effectively populate the metastable ^3P_J states in calcium and ytterbium. In

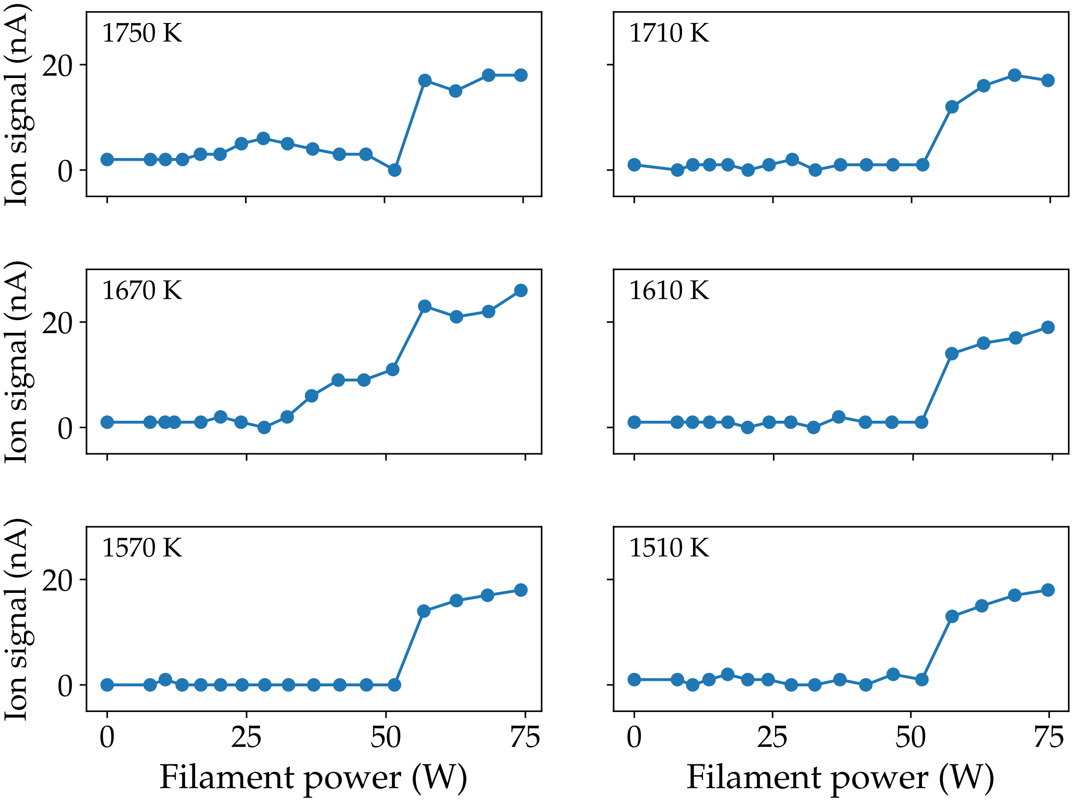

Figure 5.11: Ytterbium ion signal from the surface ionization detector at various hot wire temperatures shown in the upper left corner of the plots. We swept through a range of power in the discharge cathode for each measurement to modulate the number of metastable atoms in the atomic beam. A DC background signal has been subtracted from the data.

calcium, it is estimated that 0.24% of the atomic beam is excited to the metastable states. However, the reasons this is an underestimate are twofold. First, our detection system in Figure 5.3 aimed to detect the fluorescence of the ${}^3D_J \rightarrow {}^3P_J$ decays. There is no compelling reason to assume that all atoms populating the ${}^3P_J$ states did so via the decay of the ${}^3D_J$ states – some may have been directly excited to the ${}^3P_J$ states from the ground state and others may have decayed from the ${}^3S_1$ triplet state. Second, some unknown fraction of atoms were surely excited to the metastable singlet ${}^1D_2$ state – atoms which we cannot detect but which are expected to contribute to the surface ionization signal along with the ${}^3P_J$ atoms.

In the case of ytterbium, the number of atoms in the metastable ${}^3P_{0,2}$ states can be readily calculated from the fluorescence of the ${}^3P_1$ state (see Figure 5.5). However, the oven needed to be operated at a high temperature in order to produce a self-sustaining discharge. At this temperature, the flow of atoms out of the oven was far from effusive and the total flux of atoms is nontrivial to estimate accurately. For this reason, it cannot be discerned what fraction of atoms are in the metastable state nor what fraction ultimately impinge on the surface ionization hot wire as the angular distribution is atypical.

Nonetheless, we were able to rigorously demonstrate that metastable calcium and ytterbium atoms undergo surface ionization at higher rates than their ground state counterparts. We demonstrated through thermionic emission measurements that the work function of the tungsten hot wire is appropriate for these experiments. By modulating several parameters in the discharge, we demonstrated with calcium and ytterbium that metastable atoms can be surface ionized on the hot wire surface with a much greater efficiency than ground state atoms.

Regarding calcium specifically, from the measurements of the angular distribution of the calcium beam in Figure 5.1, the percentage of atoms incident on the 0.01”-diameter hot wire at a distance of 10.2” is approximately 0.29%. Therefore, we can conclude that of the total flux of emitted calcium atoms (2×10^{17} atoms/s), about 1.4×10^{12} metastable atoms impinge on the tungsten hot wire per second. In considering the data in Figure 5.10, a surface ion signal of 500 nA corresponds to an ion flux of about 3.1×10^{12} ions/s. This indicates that for every metastable atom incident on the tungsten surface, about 2.2 ions are emitted. Immediately, we may explain this discrepancy by noting that the number of metastable calcium atoms is an underestimate for the reasons described above. Regardless, it seems likely that the surface ionization efficiency of metastable atoms is fairly high.

Chapter 6

Future work

As stated in Chapter 3, future generations of this experiment will attain far greater degrees of precision in populating the metastable states by replacing the discharge with a laser to optically pump the intercombination transition ${}^1S_0 \rightarrow {}^3P_1$. Recently, we have been working to develop an optical system pump this transition in calcium. Doing so is considerably less complicated than for ytterbium for two reasons. First, the ${}^3P_1$ state in ytterbium is not metastable due to its short lifetime. In order to populate the ${}^3P_{0,2}$ metastable states in ytterbium, we would need an additional laser to pump the 680.1 nm transition to the ${}^3S_1$ state. While in the laser field, the majority of the ${}^3S_1$ atoms would then ultimately decay to the ${}^3P_{0,2}$ states. Second, laser diodes at 556 nm are uncommon, to say the least. In contrast, only a single laser system would be needed for calcium since the 0.4 ms lifetime of the ${}^3P_1$ state is sufficiently long.

Using a laser to populate the metastable states of calcium will alleviate many of the complications involved in the discharge. It would enable us to detect a surface ion signal while simultaneously quantifying the number of atoms in the metastable state through absorption measurements at the 657.4 nm wavelength of the transition. This absorption spectroscopy would also yield a direct measure of the number of excited atoms, in contrast to the indirect fluorescence measurement of the blue ${}^3D_J \to {}^3P_J$ transitions in calcium.

There is no minimum bound on the atomic beam density for optical pumping as there is for the discharge (see Section 4.2). Because of this, the oven can be operated within the effusive regime, which would allow the angular distribution and beam intensity to be readily calculated. This was not the case with the discharge. In order to achieve a self-sustaining discharge, the oven was operated at temperatures exceeding 650 °C, producing a calcium beam in the transitional regime and a ytterbium beam that was decisively in the gas dynamic regime. Furthermore, the effects of the electron-atom collisions on the beam properties are nonexistent when using a laser.

These two advantages, a direct measure of the number of metastables and effusive flow, will enable the precise calculation of the fraction of metastable atoms incident on the ionizing surface. Knowing this quantity and the number of ions emitted from the surface allows for a straightforward calculation of the surface ionization efficiency of metastable atoms.

6.1 657.4 nm laser light source

The transition we aim to pump with this laser is specifically the ${}^1S_0 \to {}^3P_1$ intercombination transition in calcium. To summarize, this narrow transition has an Einstein coefficient of $A = 2300\,\mathrm{s}^{-1}$ for spontaneous emission and a frequency of 455.986 240 494 THz [138, 140]. Therefore, the lifetime τ of the $^3P_1$ state is

$$\tau = \frac{1}{A} = 0.43\,\mathrm{ms} \tag{6.1}$$

and the natural linewidth Δf_0 is [140]

$$\Delta f_0 = \frac{\Delta\omega_0}{2\pi} = \frac{A}{2\pi} = 374 \pm 9\,\mathrm{Hz}. \tag{6.2}$$

Since this transition is relatively narrow, the intensity required for saturating the transition is quite low and readily attainable with a standard laser diode. There are various types of laser diodes, but only the one we are currently using,[1] a Fabry-Perot laser diode consisting of an AlGaInP semiconductor, will be described.

Forward electrical bias across the laser diode produces a current through the active region between the n- and p-type cladding layers. This produces electron-hole pairs which then emit photons upon recombining. The wavelength of these photons is restricted by the (temperature-dependent) bandgap of the semiconducting material, which ranges between 1.81 eV and 2 eV for AlGaInP and encompasses the transition energy of 1.88 eV [181]. Optical feedback in the laser diode is achieved by cleaving the crystal along its crystal plane on two opposing sides of the diode. These cleaved planes function as reflectors due to the large difference in the refractive indices of the semiconductor material ($n = 3.49$ for AlGaInP [182, 183]) and the surrounding air – for this reason, such a laser diode is referred to as a Fabry-Perot laser diode. The cleaved facets form a short optical resonator cavity

---

[1] The laser diode was purchased from Thorlabs (part no.: L660P120) but manufactured by Oclaro (part no.: HL65051DG).

and the semiconducting material within the cavity functions as the gain medium in the laser [184]. In order to optimize output power, anti-reflective (AR) coatings are typically incorporated in the output facet of the laser diode (as we will see, this is a necessary property if the laser diode is to be coupled to an external cavity). The optical cavity of the laser diode can be characterized by three dimensions: height h, width w, and length l.

Our laser diode is fabricated such that the output beam is restricted to a single transverse mode (colloquially referred to as “single mode”). Since the light is emitted through a rectangular region in the output facet with dimensions h by w, the output beam will have a divergence angle $\theta_{||}$ in the plane parallel to the pn junction and a greater divergence angle $\theta_{\perp}$ in the plane orthogonal to the junction. For our laser diode, these divergence angles are temperature dependence and span ranges of $7^\circ \leq \theta_{||} \leq 13^\circ$ and $15^\circ \leq \theta_{\perp} \leq 21^\circ$. This temperature dependence is attributed to the thermal expansion of the laser diode. We collimate the light from the laser diode with an aspherical lens[2] with diameter of 9.24 mm, focal length of 6.24 mm, a numerical aperture (NA) of 0.42, and, most importantly, AR coating. The ellipsoidal and astigmatic nature of the laser beam is not an issue for our purposes, though a circular beam may be attained through the use of a pair of anamorphic prisms [185]. For optimal collimation, it is preferred to collimate the larger angle, $\theta_{\perp}$, and it is necessary that the NA of the aspherical lens exceed that

---

[2] Purchased from Thorlabs. Part no.: A100TM-B.

of the laser diode:

$$0.42 = \mathrm{NA}_{\mathrm{lens}} > \mathrm{NA}_{\mathrm{diode}} \approx \sin(21^\circ/2) = 0.18. \tag{6.3}$$

The longitudinal mode spacing is determined by the free spectral range of the diode cavity

$$\Delta\nu = \frac{c}{2nl}, \tag{6.4}$$

where n is the semiconductor group index of refraction and l is the cavity length of the laser diode. This mode spacing is temperature dependent through l. Furthermore, the longitudinal mode that will dominate within the cavity is the one with maximal gain [186].

By now, it should be apparent that the temperature of the laser diode has an outsized effect on its operation by affecting the bandgap of the semiconductor and the dimensions of the cavity. The injection current of also affects the laser wavelength, partly through a temperature effect and partly by changing the carrier density and thereby changing the index of refraction [185]. The combined sensitivity of the wavelength to the injection current is approximately $-3\,\mathrm{MHz/\mu A}$ [185, 187]. Due to its considerable temperature sensitivity, the laser diode must be externally temperature stabilized to minimize the effect of ambient temperature fluctuations. This is typically achieved with a thermoelectric element and diagnostic temperature sensor [188, 189]. In our current system, we use a thermoelectric cooler (TEC) that is integrated with a laser diode current driver interface in a commercial laser diode mount[3]. Considering the aforementioned frequency

---

[3] We use a Thorlabs temperature-controlled mount. Part no.: LDM56.

sensitivity to the injection current, it is necessary to use a current controller with a low root-mean-square noise on the order of $\lesssim 100\,\mathrm{nA}$ to minimize the effective linewidth of the laser [190]. This mount interfaced with a low noise temperature controller[4] and current controller[5].

There are two principal disadvantages associated with using only a solitary laser diode: it has a limited degree of tunability and a large linewidth. First, we require our laser diode to operate coherently at the frequency of the calcium intercombination transition $\nu = 455.986\,240\,\mathrm{THz}$. Since the laser diode frequency is subject to the temperature and current, the diode must be tuned through these parameters in order to lase at the desired wavelength. Second, once at the correct wavelength, the laser must efficiently interrogate the atomic vapor. In this regard, the large linewidth of the solitary diode, which is approximately 100 MHz, is counterproductive [191].

A greater degree of tunability and a reduction in the wavelength can be readily achieved by coupling the laser diode to a dispersive external cavity, a configuration referred to as an external cavity diode laser (ECDL). ECDLs exploit the considerable sensitivity of a laser diode to optical feedback, a consequence due in part to the low finesse and short length of the diode cavity [185]. When coupled to an external cavity, the linewidth is typically reduced to $\sim 100\,\mathrm{kHz}$ [189] and

---

[4] We use a laser diode temperature controller from Thorlabs. Part no.: TED200C.

[5] Since high precision spectroscopy is not a goal of this experiment and we do not aim to achieve ultimate laser linewidths $\lesssim 100\,\mathrm{kHz}$, we are using a laser diode current controller from Thorlabs with noise $< 2\,\mu\mathrm{A}$. Part no.: LDC205C.

may even be as low as 1 Hz [192] while enabling a mode-hop-free[6] tuning range on the order of 10 GHz [189, 193].

ECDLs employ a wavelength-selective element for optical feedback, such as a diffraction grating. Two common configurations for ECDLs using diffraction gratings are the Littman-Metcalf configuration and the Littrow configuration [194, 195, 196, 197]. The former uses an adjustable mirror to select the feedback wavelength and the latter uses an adjustable grating. The Littrow ECDL is more common and it is the configuration we have employed in our laser system.

For collimated, monochromatic light of wavelength λ incident at angle θ on a diffraction grating with grating constant d, the diffracted light exits the grating at angle θ' according to the grating equation [198]

$$n\lambda = d(\sin\theta + \sin\theta'), \tag{6.5}$$

where n is the diffraction order. In the Littrow configuration, the $n = 1$ mode is retroreflected to the laser diode and used to couple the external and diode cavities. The $n = 0$ mode provides the ECDL output power. Evidently, the grating must be oriented at the "Littrow angle" with respect to the laser diode (i.e., $\theta = \theta'$)

$$n\lambda = 2d\sin\theta. \tag{6.6}$$

The frequency given by Equation 6.6, $\nu_g = c/2d\sin\theta$, is the central frequency of the grating passband. The width of the passband is inversely proportional to the

---

[6] A continuous tuning of the laser frequency while operating in the same longitudinal mode. A mode hop refers to the stochastic jump between different longitudinal modes as the injection current, temperature, or ECDL parameters are modulated.

number of grating lines illuminated, $\Delta\nu = \nu_g/N$ [199]. Under ideal performance, only the longitudinal mode with the highest gain will lase with the external cavity. However, in reality, several modes may lie within the passband of the grating. Assuming negligible dispersion, the mode spacing in an ECDL is

$$\Delta\nu_{\text{mode}} = \frac{c}{2L_{\text{ext}}}, \tag{6.7}$$

where L_{ext} is the external cavity length [199]. When compared to the mode spacing of a solitary diode in Equation 6.4, it is evident that the mode spacing is diminished when coupling to an external cavity.

Using a diffraction grating in an ECDL creates a standing wave between the grating and the high reflectivity back facet of the laser diode, with nodes on each groove of the grating. The grating enables two means of tuning the laser frequency: displacing the grating in the direction parallel to the laser beam and rotating the grating about some pivot point on the plane of the back plane of the diffraction grating (see Figure 1 in [189]). The former tunes the frequency by modulating the external cavity length; the latter by finely selecting the frequency fed back to the diode [200]. The distance of the grating from the optimal pivot point L_g for a maximal mode hop free tuning range is related to the length of the external cavity L_{ext} and the Littrow angle θ [189]

$$L_g = L_{\text{ext}}\frac{\cos\theta}{\tan\theta}. \tag{6.8}$$

The mode hop free tuning range can be optimized by simultaneously changing the cavity length and rotating the grating [189, 193].

Despite having a superior output efficiency when compared to the Littman-Metcalf configuration, a disadvantage of a rudimentary Littrow ECDL is that the angle of the zeroth order output beam changes as the grating is rotated when tuning the frequency. This problem is frequently circumvented by incorporating a fixed planar mirror into the mount supporting the grating in order to reflect the zeroth order output beam in a direction parallel to the first order beam (i.e., the mirror, like the grating, is oriented at the Littrow angle with respect to the laser diode). In this manner, when the grating is rotated by some angle ϕ, the zeroth order beam is leaving the grating and incident on the mirror is deflected by 2ϕ. However, since the mirror rotates by the same amount in tandem with the grating, the output beam is deflected by -2ϕ such that the net angular displacement is zero [188]. The orientations of the grating and mirror used in our ECDL are shown in Figures 6.1 and 6.2.

In our ECDL, we use a dielectric planar mirror[7] with a reflectivity $\gtrsim 90\%$ at 657 nm and a UV holographic reflective grating[8] with 1800 grooves/mm. The length of the external cavity of our ECDL is $L_{\text{ext}} = 3.18\,\text{cm}$. The orientation of the grooves on the grating with respect to the laser diode is important [190, 201]. Diffraction gratings exhibit different efficiencies depending on whether the incident light is polarized parallel (p) or perpendicular (s) to the grating grooves. In a p-plane configuration, the efficiency of the grating is low. A lower grating efficiency results higher zeroth order output beam power at the expense of the first

---

[7] Mirror from Thorlabs. Part no.: BBSQ05-E02.

[8] Grating from Thorlabs. Part no.: GH13-18U.

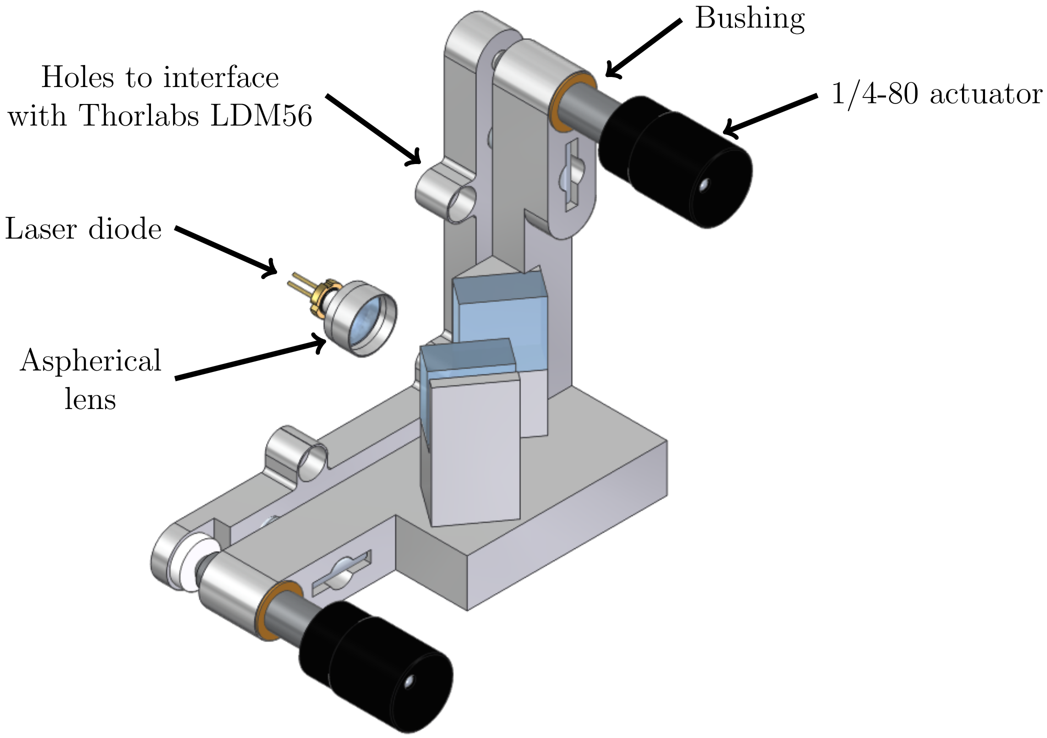

Figure 6.1: ECDL isometric view.

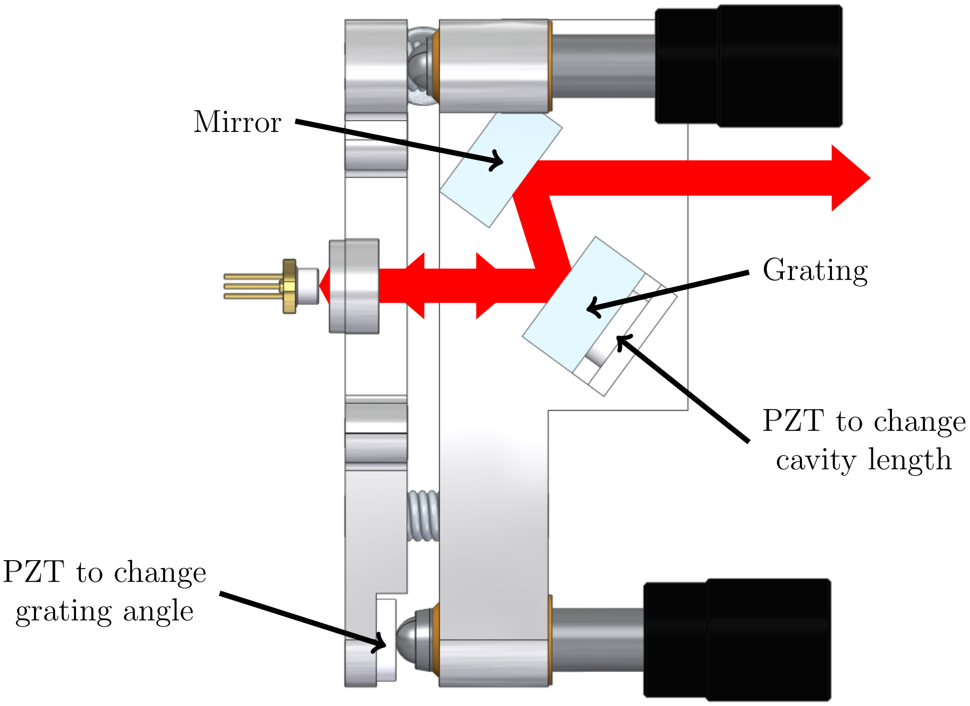

Figure 6.2: ECDL top view.

order diffraction reflectivity – this culminates in a broader linewidth due to poorer optical feedback to the diode but greater output power. Conversely, in an *s*-plane configuration, the higher efficiency of the grating results in a narrower linewidth at the expense of output power. Our UV grating has an efficiency slightly greater than 5% when oriented in the *p*-plane configuration.

The laser diode and the aspherical lens are both mounted on the commercial laser diode mount (not shown in the Figures). The mirror and grating are mounted on a homemade aluminum kinematic mount consisting of a back frame that interfaces with the laser diode mount and a stage that supports the optics. The stage is held onto the back frame by two springs[9] and coarsely adjusted by two 1/4-80, ball-tipped actuators[10] that pivot about a 0.375" ball bearing (not shown in the Figures). The actuators interface with threaded bushings[11] that have been press-fitted into the aluminum stage.

The ECDL can be coarsely aligned by adjusting the 1/4-80 actuators until the small reflection of the retroreflected first order beam from the aspherical lens is superimposed with the zeroth order beam some distance beyond the mirror. During this stage, at currents above the threshold current, the power output of the laser will increase abruptly once the internal diode cavity is coupled to the external cavity. Decreasing the injection current to slightly below the lasing threshold and readjusting the actuators until lasing is achieved will refine the coupling of the two

---

[9] Springs from Associated Springs Raymond. Part no.: E01200180500M. See `www.asraymond.com`.

[10] Actuators from Thorlabs. Part no.: FAS150.

[11] Bushings from Thorlabs. Part no.: F25SSN2P.

cavities. This procedure can be repeated until the ECDL is sufficiently aligned. The (temperature-dependent) threshold current can be calculated by measuring the output power of the laser as a function of the injection current, as shown in Figure 6.3. The sudden increase in output power for injection currents above the threshold indicates the onset of laser action. Extrapolating the linear data in the lasing regime to the point of zero power is a means of calculating the threshold current. The temperature and ECDL dependence of the threshold current is shown in Figure 6.4. As anticipated, the laser is more efficient at lower temperatures and when stabilized to an external cavity [185].

After aligning the ECDL, the vertical actuator (which pivots the grating on a plane normal to the plane established between the diode, grating, and mirror) should not be readjusted. Any coarse tuning of the laser frequency can be accomplished with the horizontal actuator by changing the angle of the grating with respect to the laser. The range of wavelengths accessible with the horizontal actuator at various temperatures is shown in Figure 6.5. Data also shown for the solitary diode without the external cavity and a previous iteration of the ECDL with a larger cavity length of 4.18 cm. In order to easily access the transition wavelength of 657.4 nm, we will cool the diode to about 8 °C.

As the actuators are only used for coarse tuning of the laser frequency, fine tuning can be accomplished with piezoelectric transducers (PZT). We incorporated two PZTs[12] each with a maximal displacements of 3.3 µm in our ECDL, one at the

---

[12] PZTs from Thorlabs. Part no.: PA25LEW.

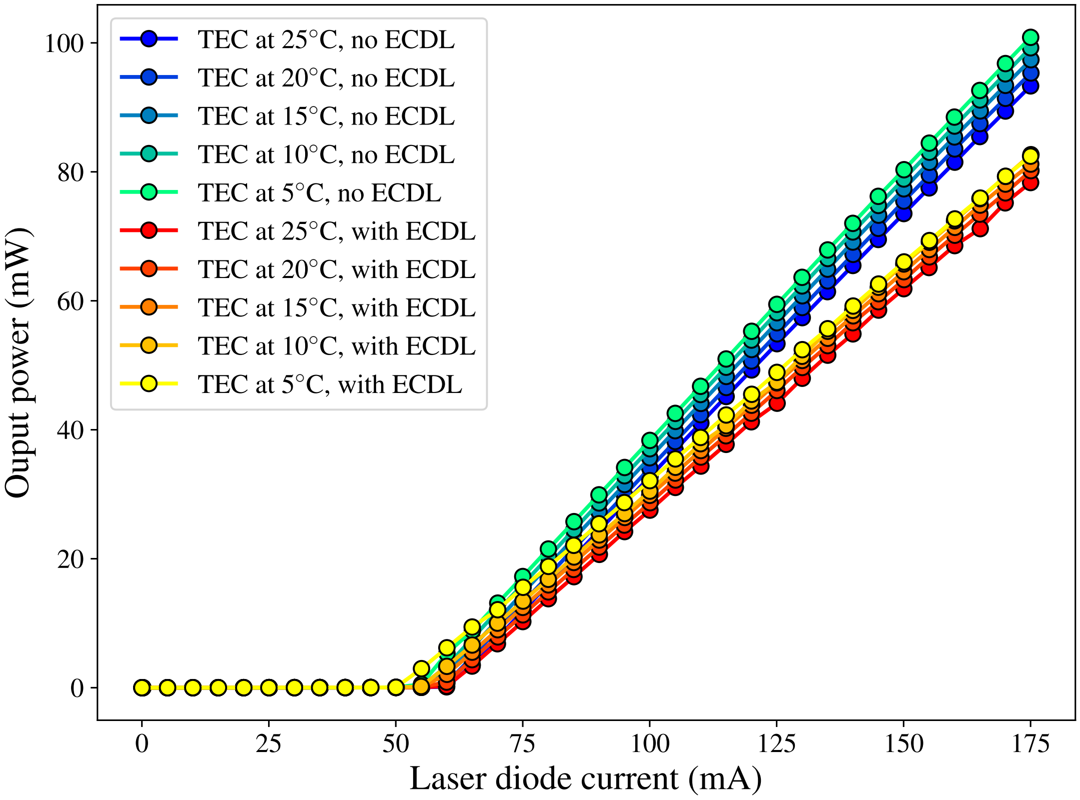

Figure 6.3: Output power as a function of current for laser diode at various temperatures, with and without the external cavity. The 7% efficiency of the diffraction grating and the reflectivity of the mirror account for the lower power output with the ECDL.

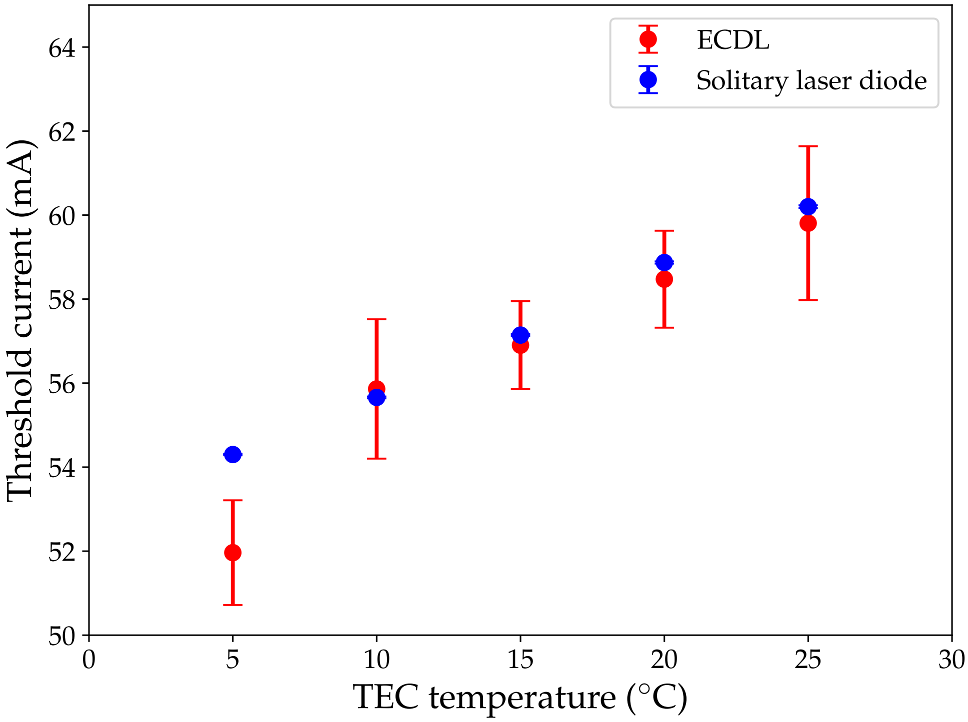

Figure 6.4: Threshold current with and without the external cavity extrapolated from the data in Figure 6.3.

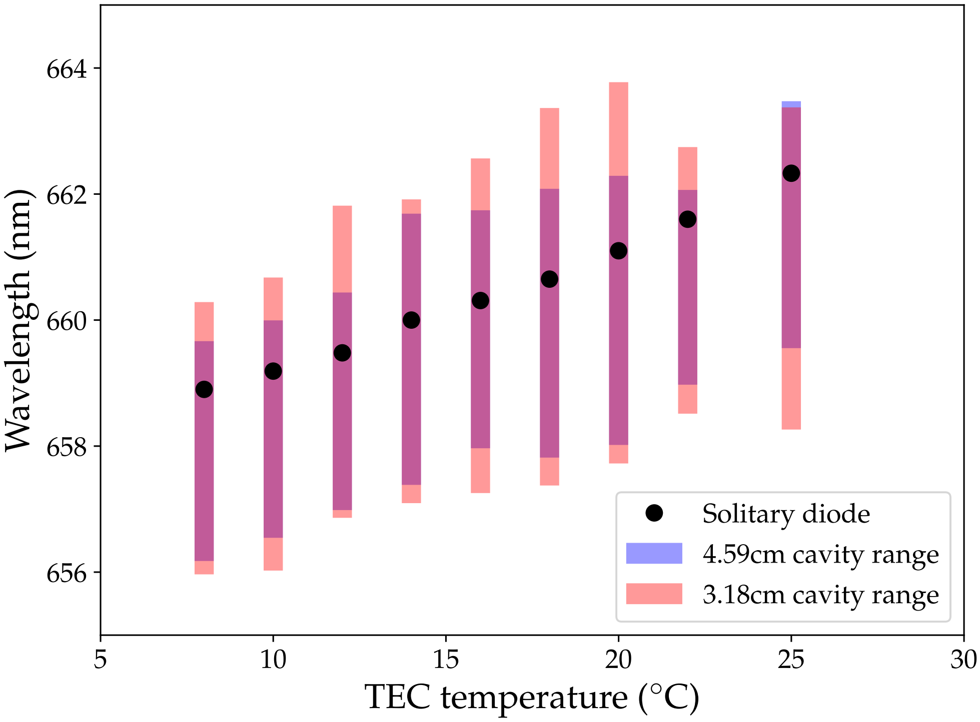

Figure 6.5: Range of wavelengths spanned by the ECDL at various temperatures. An earlier version of the ECDL had a longer cavity length of 4.59 cm. The current ECDL has a shorter cavity length of 3.18 cm and can operate a large range of wavelengths. Data is also shown for the temperature-dependent wavelength of the solitary diode. All measurements were performed at the same injection current of 100 mA.

base of the horizontal 1/4-80 actuator for modulating the angle of the grating and another behind the grating to modulate the cavity length. The former was held in place solely by the springs in the mount and the latter was glued[13] onto the grating and the mount. Likewise, the mirror was glued onto the aluminum mount. When the laser is operating on a single longitudinal mode, the PZT modulated the laser frequency by about $60 \pm 2\,\mathrm{MHz/V}$ and the PZT behind the grating modulated the laser frequency by $42 \pm 1\,\mathrm{MHz/V}$. These numbers were calculated by monitoring the laser frequency using a wavemeter[14] while applying a square signal to each individual PZT.

In addition to the tunability and power output of the ECDL, another property of great significance is the mode stability. This includes the dynamic mode stability as the laser frequency is continuously scanned. The mode hop free tuning range may be increased by scanning the PZTs and laser diode current simultaneously, or by shortening the cavity length, as we did by 1.4 cm in the latest iteration of our ECDL [189]. The static mode stability refers to the laser's ability to operate on a single longitudinal mode when the PZTs and injection current are unperturbed. The static mode stability can be improved by isolating the laser from environmental fluctuations in air pressure, temperature, and mechanical vibrations [189]. We have mitigated the effects of all of these parameters by hermetically sealing the ECDL in a plexiglass box with sound-absorbing padding[15] and supported

---

[13] The glue used to attach the mirror, grating, and one PZT was purchased from Thorlabs. Part no.: LOC312.

[14] WS-7 wavemeter from Toptica Photonics with a resolution up to 2 MHz.

[15] Sound-absorbing sheets from McMaster-Carr. Part no.: 9710T66.

on four sorbothane pads[16]. The ECDL is immediately followed by a Faraday optical isolator to minimize unwanted feedback. When constructing a homemade kinematic mount, as we have done for our ECDL, it may be easy to overlook the effect of the lubrication of the 1/4-80 actuators – we eventually learned that using a general purpose machining oil as a lubricant can be detrimental because it causes the actuators to slowly creep under the stress of the springs, thereby changing the orientation of the grating and the laser frequency. Using a more appropriate lubricant[17] significantly improved the performance of our ECDL. As a consequence of its isolation and proper lubrication, our ECDL can now operate on a single longitudinal mode without some external frequency stabilization for up to an hour.

6.2 Spectroscopy of the calcium intercombination transition

In order to efficiently pump calcium atoms to the $^3P_1$ state, the frequency of the ECDL must be stabilized to an appropriate external frequency reference. For this specific transition, considering its narrow linewidth, high finesse resonant cavities (and subsequent fine tuning using an acouto-optic modulator) [140] and saturated absorption signals [202, 185] have traditionally been used as frequency references. Since we lack an adequate resonant cavity, detecting and stabilizing to a saturated absorption signal is the most viable option.

---

[16] Vibration isolation pads from Thorlabs. Part no.: AV4.

[17] Such as Apiezon grease from Thorlabs. Part no.: GKZ8.

Considering calcium's low vapor pressure (see Figure 3.1), to vaporize sufficient quantities of calcium for spectroscopy, it must be heated to temperatures above 400 °C. Since this is exceeds the temperature rating of conventional viewports[18], exposed windows will eventually be coated and obstructed by the vapor. Groups have historically circumvented this issue with a buffer gas [203] or by detecting an absorption signal in the thermal beam itself [204, 205]. Both of these approaches have their own advantages and disadvantages: the former solves the problem of window-coating but suffers from pressure broadening of the signal; the latter does not require constructing an additional instrument, solves the problem of window-coating, but suffers from a low signal to noise ratio due to the short distance over which the laser interrogates the atomic beam. Two promising alternatives are unconventional vapor cell designs employing calcium fluoride windows to contain the vapor within a larger chamber [206] or two in-vacuum mirrors to redirect the laser and are directly exposed to the calcium vapor [207]. We have opted to design a vapor cell similar to the second example even though it inherently requires periodic replenishing of the calcium stock.

An image of the vapor cell and our corresponding setup for Doppler-free spectroscopy is shown in Figure 6.6. The main body of the cell is a custom-made 6" long 1.75" inner diameter stainless steel tube with small coaxial channels (a length of 5.875" and an inner diameter of 0.375") on both sides for confining the calcium vapor. The wall thickness throughout the tube is 0.0625". A 1"-long 1.33CF half nipple was laterally welded onto the main body of the cell to facilitate

---

[18] See Kurt J. Lesker `https://www.lesker.com`.

the refilling of the cell (not shown in Figure 6.6. The main body of the cell and the lateral flange were wrapped and heated by high temperature heater cables[19] and subsequently by thermal insulation tape[20]. Three thermocouples were inserted under the heater tape on three locations: the main body of the cell, one of the smaller coaxial channels, and the lateral flange.

The main body of the cell is sandwiched between two four-way CF crosses, each containing one aluminum post with a 45° degree cut and circular bore for mounting 1" silvered mirrors[21]. The aluminum posts were incorporated via rotatable flanges to facilitate the alignment of the laser prior to evacuating the cell. After inserting calcium granules, the cell was evacuated by a turbomolecular pump connected via a 90° all metal valve (not shown). The pressure is monitored by a thermocouple pressure gauge with a minimum reading of $\sim$ 20 mTorr.

The two overlapping and counter propagating pump and probe beams are split, directed through the cell, and subsequently discarded and detected with a photodiode[22], respectively. By design, the mirrors in the cell are continuously subject to the calcium vapor and eventually become entirely coated with calcium. For some duration throughout the coating process, the mirrors sustain a near total loss in reflectivity and equilibrate at a reflectivity of approximately 84% [207],

---

[19] Heaters from McMaster-Carr. Part no.: 4550T133.

[20] We ultimately used a basalt fabric insulation tape from McMaster-Carr instead of other fiberglass or ceramic alternatives since fewer particles became airborne during the assembly process. Part no.: 1727T12.

[21] Aluminum mirrors may be used as well, but dielectric coated mirrors should be avoided as they will contaminate the cell and coat the viewports when exposed to the hot calcium vapor.

[22] From Thorlabs. Part no.: PDA100A.

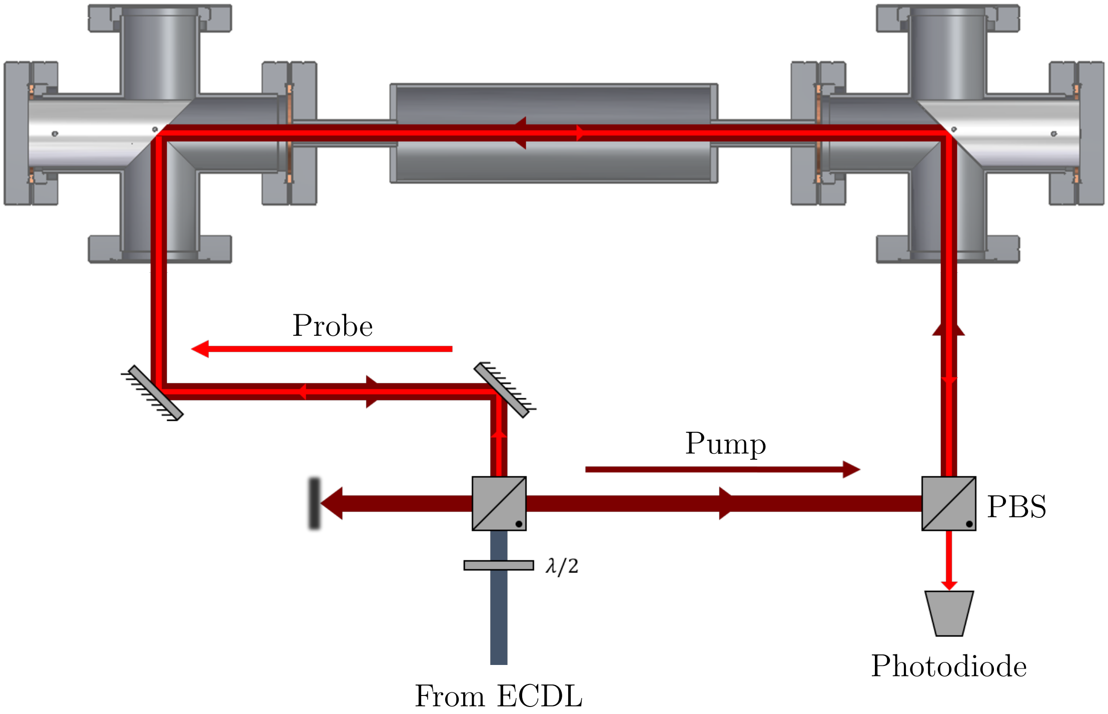

Figure 6.6: A simplified optical setup for Doppler-free spectroscopy on a calcium vapor cell (PBS: polarized beam splitter cube. $\lambda/2$: half-wave plate). The CAD image of the cell has been shortened for this figure, but the distance between the centers of the 45° mirrors is $\sim 58.1\,\text{cm}$. The flange attached laterally on the cell body for loading the calcium granules is not shown.

giving the cell (two mirrors and two viewports) an overall transmission of about 63%.

Similar to the ytterbium deposition on the mirror used to image the discharge onto a detector (see Section 5.2.2), a high calcium deposition rate on the 45° mirrors in the vapor cell resulted in a noticeably rough surface and greatly diminished reflectivity such that greater than 99% of the laser power was attenuated through the vapor cell. We have found that operating the cell at a temperature no greater than 550 °C produced a sufficiently dense calcium vapor while maintaining an adequately low deposition rate on the mirrors. At a cell temperature of 550 °C, the density of the calcium vapor is $n = p/k_BT = 4.5 \times 10^{19}$ atoms/m^3 and the flux of atoms through each tube is no greater than 5.3×10^{16} atoms/s.

As the calcium is vaporized, the velocity distribution of the atoms is Maxwellian [208]:

$$P(v) = \left(\frac{1}{\sqrt{\pi}\alpha}\right) \exp\left(-\frac{v^2}{\alpha^2}\right), \tag{6.9}$$

where $\alpha = \sqrt{2k_BT/m}$, $m = 6.642 \times 10^{-26}$ kg is the mass of a calcium atom, T is the cell temperature. For atoms with a finite velocity component in the direction of the laser beam, the laser frequency will be Doppler shifted from its rest-frame frequency of f_0 by

$$f = f_0\left(1 \pm \frac{\vec{v} \cdot \hat{r}}{c}\right), \tag{6.10}$$

where $\vec{v}$ is the atom velocity and $\hat{r}$ is the propagation direction of the interrogating laser [209]. For an ensemble with a velocity distribution given by Equation 6.9, the spectral lineshape is a convolution of the natural lineshape of individual particles and the Doppler shifted Maxwellian distribution, resulting in a "Doppler broadening" of the absorption profile of a laser propagating through the vapor. The characteristics spectral width (FWHM) of the Doppler-broadened profile is given by [208]:

$$\Delta f_{\text{Doppler}} = 2f_0\sqrt{\frac{2\ln(2)k_BT}{mc^2}}. \tag{6.11}$$

At a vapor cell temperature of 550 °C, the intercombination line in calcium has a Doppler width of $\Delta f_{\text{Doppler}} = 1.48\,\text{GHz}$, nearly seven orders of magnitude greater than the natural linewidth of the transition. Finding the true frequency of the transition within this broad profile can be readily accomplished with a technique known as Doppler-free or saturated absorption spectroscopy.

As shown in Figure 6.6, saturated absorption spectroscopy requires two superimposed and counter propagating laser beams at different intensities (the probe beam is the low intensity beam and the pump beam is the high intensity beam) to traverse the atomic vapor. As the laser frequency is modulated, the absorption of the probe beam is monitored by an appropriate photodetector. Without the pump beam simultaneously interacting with the vapor, if the probe beam frequency is scanned over a range exceeding $\Delta f_{\text{Doppler}}$ in the vicinity of f_0, the Doppler broadened absorption profile can be resolved, as shown in Figure 6.7a.

Although they are both at the same frequency, because they are propagating in opposite directions, the pump and probe beam will address different velocity classes within the distribution in Equation 6.9. However, when the ECDL frequency is on resonance, both beams address the same atoms with $\vec{v}\cdot\hat{r} = 0$. For a two-state system such as this transition in calcium, when the ECDL frequency

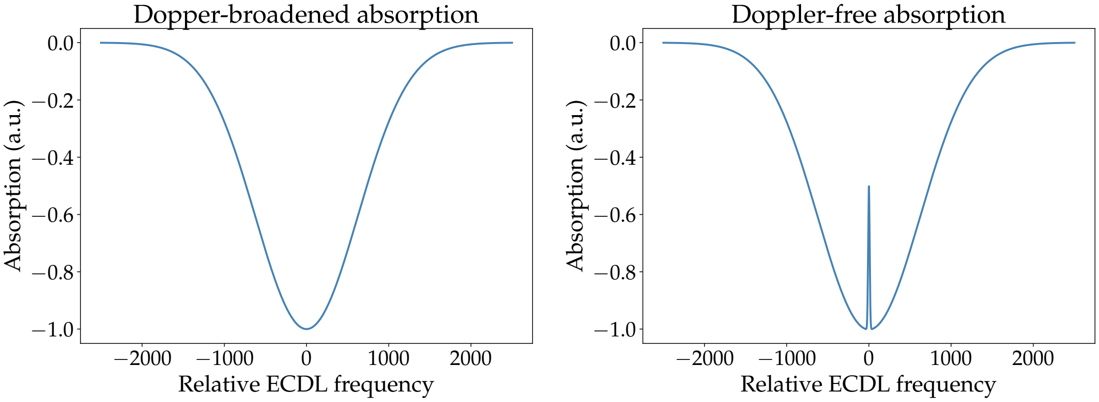

(a)

(b)

Figure 6.7: Calculated probe beam absorption profiles without (a) and with (b) the pump beam for a cell temperature of 550 °C. As the Doppler shift is the dominant broadening mechanism, without the pump beam, the FWHM of the absorption profile is given by Equation 6.11. When the intense pump beam is incorporated, the FWHM of the Lamb dip can theoretically be as low as the natural linewidth of the transition.

is f_0, the more intense pump beam will excite a majority of the atoms, which will no longer interact with the probe (thereby saturating the transition), leading to a sharply diminished absorption of the probe beam near resonance, as shown in Figure 6.7b. This saturated absorption spectrum in known as the Lamb dip and will have a FWHM equal to the natural linewidth Γ of the transition, barring the effect of additional broadening mechanisms that may exceed Γ.

In the case of our setup, the only relevant broadening mechanisms are pressure broadening and power broadening. The former was shown to scale linearly as

$$\Delta f_{\text{pressure}} = \Delta f_0 + B, \tag{6.12}$$

where $B \approx 11\,\text{MHz/Torr}$ at $600\,\text{K}$ for this transition [203]. The power-broadened linewidth scales as

$$\Delta f_{\text{power}} = \Delta f_0 \sqrt{1 + I/I_{\text{sat}}}, \tag{6.13}$$

where I is the laser intensity and I_{sat} is the saturation intensity of the transition [209]. The contributions from pressure and power broadening are not expected to be very significant for pressures ¡20 mTorr or for laser powers less than 100 mW [203]. Since the linewidth of our laser is certainly not less than the natural linewidth of the intercombination transition, the Doppler-free spectrum should have a width determined by the linewidth of the laser. This is readily apparent in the saturated absorption spectrum in Figure 6.8.

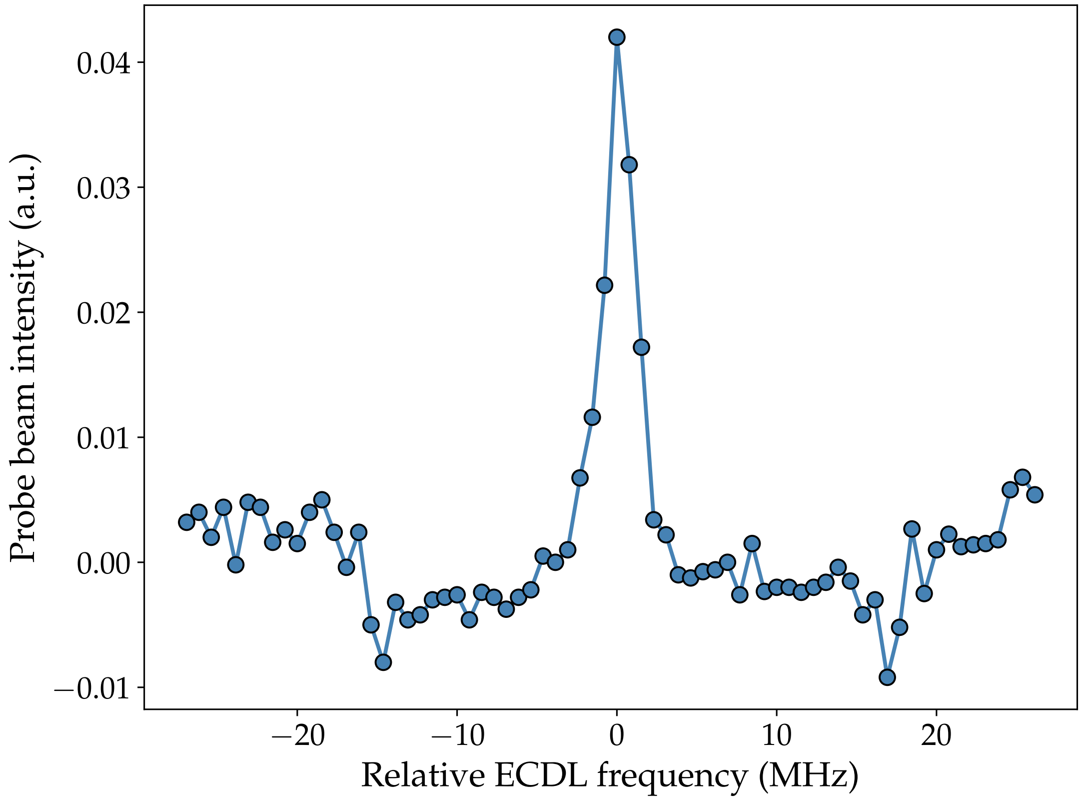

Figure 6.8: Oscilloscope trace of the saturated absorption spectrum of the calcium $^1S_0 \to {}^3P_1$ intercombination transition. The natural linewidth of this transition is approximately 400 Hz and the FWHM of this Lamb dip is approximately 2.2 MHz. This discrepancy is due to the fact that the laser linewidth is significantly broader than 400 Hz.

Appendix

Appendix 1

Origin of the Saha-Langmuir Equation

In thermodynamic equilibrium, at temperature T, the number of atoms in a particular atomic state, n_i, follows a Boltzmann distribution:

$$\frac{n_i}{n} = \frac{g_i}{Z(T)} \exp(-E_i/k_B T), \tag{1.1}$$

where n is the total number of atoms, g_i is the statistical weight of the i^{th} atomic state, E_i is the energy difference between the i^{th} state and the ground state, and $Z(T)$ is the partition function for the atom. It follows that the Boltzmann distribution for an electron excited to the continuum with momentum between p and $p + dp$ is

$$\frac{dn^*}{n} = \frac{dg^*}{Z(T)} \exp\left(- \frac{I + p^2/2m_e}{k_B T}\right), \tag{1.2}$$

where I is the ionization energy of the atom and n^* denotes the number of ionized atoms with a statistical weight of dg^*. dg^* encompasses the statistical weight of the ion (i.e., the ground state of the ion) and the free electron, which can be determined by considering that in a quantum cell in phase space with a volume h^3, an electron can exist in one of two possible states. The number of cells available for a free electron with momentum between p and $p + dp$ is $V(4\pi p^2)dp/h^3$, where $V = 1/n_e$ is the volume in space available for a free electron and n_e is the free electron density. Eq. 1.2 then becomes

$$\begin{aligned}\frac{n^*}{n} &= \frac{g^*}{Z(T)}\frac{8\pi}{n_e h^3}e^{-I/k_BT}\int_0^\infty p^2 \exp\left(- \frac{p^2}{2m_e k_B T}\right)dp \\ &= \frac{2}{n_e}\frac{g^*}{Z(T)}\left(\frac{2\pi m_e k_B T}{h^2}\right)^{3/2} \exp\big(- I/k_BT\big)\end{aligned} \tag{1.3}$$

The final result in Equation 1.3 is the Saha equation which quantifies the ionized fraction of an element in thermal equilibrium.

At equilibrium, adsorbates on a metal surface are fractionally ionized in the reaction $A_{ads} \leftrightharpoons A^+_{ads} + e^-$. Correspondingly, the number density of atoms, ions, and electrons are related by Equation 1.3, which can be rewritten as

$$\frac{n_i n_e}{n_a} = \frac{g_i g_e}{g_a}\left(\frac{2\pi m_e k_B T}{h^2}\right)^{3/2} \exp(-I/k_BT). \tag{1.4}$$

Here, the ion and atom number densities and statistical weights have been changed to n_i, g_i and n_a, g_a, respectively, and $g_e = 2$. The number density of electrons in the metal surface can be found by computing

$$n_e = \int_0^\infty f(E)g(E)dE, \tag{1.5}$$

where $f(E)$ is the Fermi distribution function and $g(E) = \frac{1}{2\pi^2}\left(\frac{2m}{\hbar^2}\right)^{3/2}\sqrt{E}$ is the three dimensional density of states. It follows that the electron number density is found to be [210, 91]

$$n_e = g_e\left(\frac{2\pi m_e k_B T}{h^2}\right)^{3/2} \exp(-\Phi/k_BT), \tag{1.6}$$

where Φ is the work function of the metal surface. Incorporating Equation 1.6 into Equation 1.3 yields the Saha-Langmuir equation for the degree of ionization, α, of an adsorbate on a metal surface:

$$\alpha = \frac{n_i}{n_a} = \frac{g_i}{g_a} \exp[(\Phi - I)/k_B T] \tag{1.7}$$

Bibliography

[1] R. Muller and H.W. Wassmuth. Desorption kinetics of alkaline earth adparticles on tungsten with variation of the oxygen surface coverage. *Surf. Sci.*, 34:249–267, 1973.

[2] G. Moore and H. Allison. Adsorption of strontium and of barium on tungsten. *J. Chem. Phys.*, 23(9):1609–1621, 1955.

[3] T. Madey, A. Petrauskas, and E. Coomes. Thermal desorption of Sr from W. *J. Chem. Phys.*, 42(2):479–485, 1965.

[4] H. Utsugi and R. Gomer. Field desorption of barium from tungsten. *J. Chem. Phys.*, 37(8):1706–1719, 1962.

[5] I. Sobelman. *Atomic Spectra and Radiative Transitions.* Springer-Verlag Berlin Heidelberg, 2 edition, 1977.

[6] V. Shevelko. *Atoms and their spectroscopic properties.* Springer-Verlag Berlin Heidelberg, 1st edition, 1997.

[7] E. Bergmann, P. Bopp, C. Dorsch, and Et. al. Nuclear charge distribution of eight Ca-nuclei by laser spectroscopy. *Z. Phys. A.*, 294:319–322, 1980.

[8] K. Pandey, A. Singh, P. Kiran Kumar, and Et. al. Isotope shifts and hyperfine structure in the 555.8-nm 1S0 - 3P1 line of Yb. *Phys. Rev. A* -

At. Mol. Opt. Phys., 80(2):1–6, 2009.

[9] R. Gomer. *Field Emission and Field Ionization.* Harvard University Press, 1993.

[10] J. Hölzl and F. Schulte. Work function of metals. *Solid Surf. Phys.*, 85:1, 1979.

[11] H. Pauly. *Atom, molecule, and cluser beams I.* Springer-Verlag Berlin Heidelberg, 1st edition, 2000.

[12] O. Zatsarinny, K. Bartschat, L. Bandurina, and Et Al. Electron-impact excitation of calcium. *J. Phys. B At. Mol. Opt. Phys.*, 40(20):4023–4031, 2007.

[13] J. Griffiths. A brief history of mass spectrometry. *Anal. Chem.*, 80(15):5678–5683, 2008.

[14] W. Lotz. Electron-impact ionization cross-sections and ionization rate coefficients for atoms and ions from hydrogen to calcium. *Zeitschrift fur Phys.*, 216(3):241–247, 1968.

[15] C. Dass. *Fundamentals of contemporary mass spectrometry.* John Wiley & Sons, Incorporated, 1 edition, 2007.

[16] M. Bart. *Electron impact ionization: measurements of absolute cross-sections and cross-beam studies.* PhD thesis, University of Canterbury, 2003.

[17] A. Crowe and J. W. McConkey. Dissociative ionization by electron impact. I. Protons from H2. *J. Phys. B At. Mol. Phys.*, 6(10):2088–2107, 1973.

[18] M. DeKieviet, M. Dürr, S. Epp, F. Lang, and M. Theis. Source for atomic beams of metastable gases: Design and performance. *Rev. Sci. Instrum.*, 75(2):345–348, 2004.

[19] K. Kuhnke, K. Kern, R. David, and G. Gomsa. High efficiency molecular-beam ionization detector with short ionization region. *Rev. Sci. Instrum.*, 65:3458, 1994.

[20] M. Klaiber and J. Briggs. Crossover from tunneling to multiphoton ionization of atoms. *Phys. Rev. A*, 94(5):1–8, 2016.

[21] V. S. Letokhov. *Laser photoionization spectroscopy.* Academic Press, Inc., 1987.

[22] M. Ammosov, N. Delone, and V. Krainov. Tunnel ionization of complex atoms and of atomic ions in an alternating electromagnetic field. *Sov. Phys. JETP*, 64:1191, 1986.

[23] P. B. Corkum, N. H. Burnett, and F. Brunel. Above-threshold ionization in the long-wavelength limit. *Phys. Rev. Lett.*, 62(11):1259–1262, 1989.

[24] M. Protopapas, C. Keitel, and P. Knight. Atomic physics with super-high intensity lasers. *Reports Prog. Phys.*, 60:389–486, 1997.

[25] K. Motomura, H. Fukuzawa, S. Son, and Et Al. Sequential multiphoton multiple ionization of atomic argon and xenon irradiated by x-ray free-electron laser pulses from SACLA. *J. Phys. B At. Mol. Opt. Phys.*, 46(16), 2013.

[26] D. Lucas, A. Ramos, J. Home, M. McDonnell, S. Nakayama, J.-P. Stacey, S. Webster, D. Stacey, and A. Steane. Isotope-selective photoionization for calcium ion trapping. *Phys. Rev. A*, 69(1):012711, 2004.

[27] S. Augst, D. Meyerhofer, D. Strickland, and S. Chin. Laser ionization of noble-gases by Coulomb-barrier suppression. *J. Opt. Soc. Am. B-Optical Phys.*, 8(4):858–867, 1991.

[28] R. Freeman and P. Bucksbaum. Investigations of above-threshold ionization using subpicosecond laser pulses. *J. Phys. B At. Mol. Opt. Phys.*, 24(2):325, 1991.

[29] M. Kaminsky. *Atomic and ionic impact phenomena on metal surfaces.* Academic Press, Inc., 1965.

[30] R. Delhuille, A. Miffre, E. Lavallette, M. Büchner, C. Rizzo, G. Trénec, J. Vigué, H. J. Loesch, and J. P. Gauyacq. Optimization of a Langmuir-Taylor detector for lithium. *Rev. Sci. Instrum.*, 73(6):2249, 2002.

[31] M. J. Dresser. The Saha-Langmuir equation and its application. *J. Appl. Phys.*, 39(1):338–339, 1968.

[32] J. Dillon. *Gaseous conductors: theory and engineering applications.* Dover Publications, 2nd edition, 1958.

[33] D. Alpert. Initiation of electrical breakdown in ultrahigh vacuum. *J. Vac. Sci. Technol.*, 1(2):35, 1964.

[34] D. Davies. The initiation of electrical breakdown in vacuum—a review. *J. Vac. Sci. Technol.*, 10(1):115–121, 1973.

[35] J. Dutton, S.C. Haydon, and F. Llewellyn Jones. Electrical breakdown of gases. II. Spark mechanism in nitrogen. *Proc. R. Soc. London. Ser. A.*, 213(1113):203–214, 1952.

[36] E. Müller. Work function of tungsten single crystal planes measured by the field emission microscope. *J. Appl. Phys.*, 26(6):732–737, 1955.

[37] A. Modinos. *Field, thermionic, and secondary electron emission spectroscopy.* Plenum Publishing Corporation, New York, NY, 1st edition, 1984.

[38] C. Duke and M. Alferieff. Field emission through atoms adsorbed on a metal surface. *J. Chem. Phys.*, 46(3):923–937, 1967.

[39] K. O'Donnell, A. Fahy, M. Barr, W. Allison, and P. Dastoor. Field ionization detection of helium using a planar array of carbon nanotubes. *Phys. Rev. B*, 85(11):113404, 2012.

[40] K. O'Donnell, A. Fahy, L. Thomsen, D. O'Connor, and P. Dastoor. Field ionization detectors: a comparative model. *Meas. Sci. Technol.*, 22(1):015901, 2011.

[41] X. Liu and Jo. Orloff. Analytical model of a gas phase field ionization source. *J. Vac. Sci. Technol. B Microelectron. Nanom. Struct.*, 23(6):2816, 2005.

[42] H.-D. Beckey. *Field Ionization Mass Spectroscopy.* Pergamom Press, Oxford, 1st edition, 1971.

[43] D. Riley, M. Mann, D. MacLaren, P. Dastoor, and W. Allison. Helium detection via field ionization from carbon nanotubes. *Nano Lett.*, 3(10):1455–1458, 2003.

[44] M. Southon and D. Brandon. Current-voltage characteristics of the helium field-ion microscope. *Philos. Mag.*, 8(88):579–591, 1963.

[45] E. Muller and K. Bahadur. Field ionization of gases at a metal surface and the resolution of the field ion microscope. *Phys. Rev.*, 102(3):624–631, 1956.

[46] H. Karaagac and M. Saif Islam. Enhanced field ionization enabled by metal induced surface states on semiconductor nanotips. *Adv. Funct. Mater.*, 24(15):2224–2232, 2014.

[47] T. Mazur. *Magnetically activated and guided isotope separation.* PhD thesis, University of Texas at Austin, 2014.

[48] F. Stienkemeier, M. Wewer, F. Meier, and H . Lutz. Langmuir-Taylor surface ionization of alkali (Li, Na, K) and alkaline earth (Ca, Sr, Ba) atoms attached to helium droplets. *Rev. Sci. Instrum.*, 71(9):3480–3484, 2000.

[49] E. Sloth. *Effect of anionic constituents on the surface ionization of lithium salts*. PhD thesis, Illinois Institute of Tehcnology, 1969.

[50] A.G. Borisov, D. Teillet-Billy, J.P. Gauyacq, H. Winter, and G. Dierkes. Resonant charge transfer in grazing scattering of alkali-metal ions from an AI(111) surface. *Phys. Rev. B - Condens. Matter Mater. Phys.*, 54(23):17166–17174, 1996.

[51] R. W. Gurney. Theory of electrical double layers in adsorbed films. *Phys. Rev.*, 47(6):479–482, 1935.

[52] J. Los and J. Geerlings. Charge exchange in atom-surface collisions. *Phys. Rep.*, 190(3):133–190, 1990.

[53] W. Sesselmann, B. Woratschek, J. Kuppers, G. Ertl, and H. Haberland. Interaction of metastable noble-gas atoms with transition-metal surfaces: Resonance ionization and Auger neutralization. *Phys. Rev. B*, 35(4):1547–1559, 1987.

[54] J. Gadzuk. Theory of atom-metal interactions. *Surf. Sci.*, 6:133–158, 1967.

[55] M. Dresser. *An experimental investigation of surface ionization.* PhD thesis, Iowa State University, 1964.

[56] L.N. Dobretsov. *Elektronen-und ionenemission.* VEB-Verlag Technik, Berlin, 1954.

[57] K. Wandelt. *Surface and interface science*, volume 5. Wiley Blackwell, feb 2015.

[58] M. Scheer, R. Klein, and J. McKinley. Surface lifetimes of alkali metals on molybdenum. *J. Chem. Phys.*, 55(7):3577–3584, 1971.

[59] L. Schmidt and R. Gomer. Neutral and ionic desorption of cesium from tungsten. *J. Chem. Phys.*, 43(6):2055–2063, 1965.

[60] L. Schmidt and R. Gomer. Adsorption of potassium on tungsten. *J. Chem. Phys.*, 42(10):3573–3598, 1965.

[61] J. Frenkel. Theorie der Adsorption und verwandter Erscheinungen. *Z. Phys.*, 26(1):117–138, 1924.

[62] J. Frenkel. Über die elektrische Oberflächenschicht der Metalle. *Zeitschrift für Phys.*, 51(3-4):232–238, 1928.

[63] R. Wilmoth. *Measurement of surface stay times for physical adsorption of gases.* PhD thesis, University of Virginia, 1973.

[64] M. Scheer and J. Fine. Surface ionization of niobium. *J. Chem. Phys.*, 42(10):3645–&, 1965.

[65] I. Langmuir and K.H. Kingdon. Thermionic effects caused by vapours of alkali metals. *Proc. R. Soc. London. Ser. A.*, 107(741):61–79, 1925.

[66] M. Dresser and D. Hudson. Surface ionization of some rare earths on tungsten. *Phys. Rev.*, 137:673, 1965.

[67] S. Datz and E. Taylor. Ionization on platinum and tungsten surfaces. I. The alkali metals. *J. Chem. Phys.*, 25(3):389–394, 1956.

[68] S. Datz and E. Taylor. Ionization on platinum and tungsten surfaces. II. The potassium halides. *J. Chem. Phys.*, 25(3):395–397, 1956.

[69] K.W. Kolasinski. *Surface science: foundations of catalysis and nanoscience.* John Wiley & Sons, Ltd, 3rd edition, 2012.

[70] J. A. Becker and C. D. Hartman. Field emission microscope and flash filament techniques for the study of structure and adsorption on metal surfaces. *J. Phys. Chem.*, 57(2):153–159, 1953.

[71] H. Hagstrum. Instrumentation and experimental procedure for studies of electron ejection by ions and ionization by electron impact. *Rev. Sci. Instrum.*, 24(12):1122–1142, 1953.

[72] H. Hagstrum. Effect of monolayer adsorption on the ejection of electrons from metals by ions. *Phys. Rev.*, 104(6), 1956.

[73] K. Christmann. *Introduction to surface physical chemistry.* Springer-Verlag Berlin Heidelberg, 1 edition, 1991.

[74] E. Ehrlacher and J. Huennekens. Noble-gas broadening rates for barium transitions involving the metastable 6s5d 3DJ levels. *Phys. Rev. A*, 46(5):2642–2648, 1992.

[75] H. Margenau and W. G. Pollard. The forces between neutral molecules and metallic surfaces. *Phys. Rev.*, 60(2):128–134, 1941.

[76] S. K. Lyo and R. Gomer. Theory of Chemisorption. In R. Gomer, editor, *Interact. Met. Surfaces*, pages 41–62. Springer-Verlag Berlin Heidelberg, 1 edition, 1975.

[77] W. Heitler and F. London. Wechselwirkung neutraler Atome und homoopolare Bindung nach der Quantenmechanik. *Z. Phys.*, 44:455–472, 1927.

[78] A. R. Miller. The variation of the dipole moment of adsorbed particles with the fraction of the surface covered. *Math. Proc. Cambridge Philos. Soc.*, 42(3):292–303, 1946.

[79] M. Boudart. Heterogeneity of metal surfaces. *J. Am. Chem. Soc.*, 74(14):3556–3561, 1952.

[80] A. A. Holscher. Surface potentials of nitrogen on individual crystal faces of tungsten. *J. Chem. Phys.*, 41(2):579–580, 1964.

[81] T. A. Delchar and G. Ehrlich. Chemisorption on single-crystal planes: Nitrogen on tungsten. *J. Chem. Phys.*, 42(8):2686–2702, 1965.

[82] A. Michaelides, P. Hu, M. H. Lee, A. Alavi, and D. A. King. Resolution of an Ancient Surface Science Anomaly: Work Function Change Induced by N Adsorption on W(100). *Phys. Rev. Lett.*, 90(24):4, 2003.

[83] R. Gomer and J. Hulm. Adsorption and diffusion of oxygen on tungsten. *J. Chem. Phys.*, 27(6):1363–1376, 1957.

[84] R. Gomer. Scattering lengths of inert gases for electrons of negative energy. Field emission through dielectrics. *J. Chem. Phys.*, 29(2):443–444, 1958.

[85] R. Gomer. Adsorption and diffusion of argon on tungsten. *J. Phys. Chem.*, 63(4):468–472, 1959.

[86] Y.C. Chen, J.E. Cunningham, and C.P. Flynn. Dependence of rare-gas-adsorbate dipole moment on substrate work function. *Phys. Rev. B*, 30(12):7317–7319, 1984.

[87] M D Scheer and J Fine. Kinetics of Desorption .3. Rb+,K+, and Na+ on Rhenium. *J. Chem. Phys.*, 39(7):1752, 1963.

[88] M. Scheer and J. Fine. Kinetics of desorption. II. Cs+ and Ba+ from rhenium. *J. Chem. Phys.*, 38(2):307–309, 1963.

[89] T. A. Flaim and P. D. Ownby. Adsorbate-induced work function changes. *Surf. Sci.*, 32:519–526, 1972.

[90] H. Kawano, T. Takahashi, Y. Tagashira, H. Mine, and M. Moriyama. Work function of refractory metals and its dependence upon working conditions. *Appl. Surf. Sci.*, 146(1):105–108, 1999.

[91] C. Herring and M. H. Nichols. Thermionic emission. *Rev. Mod. Phys.*, 21(2), 1949.

[92] H. Daley, A. Yahiku, and J. Perel. K+, Na+, and Li+ Desorption from oxygenated tungsten. *J. Chem. Phys.*, 52(7):3577–3579, 1970.

[93] M. P. Marder. *Condensed Matter Physics.* John Wiley & Sons, Incorporated, 2nd edition, 2010.

[94] N. Ashcroft and N. Mermin. *Solid State Physics.* Holt, Rinehart and Winston, 1976.

[95] E. Wigner and J. Bardeen. Theory of the work functions of monovalent metals. *Phys. Rev.*, 48, 1935.

[96] J. Bardeen. Theory of the work function. II. the surface double layer. *Phys. Rev.*, 49(9):653–663, 1936.

[97] G. Smith. Thermionic and surface properties of tungsten crystals. *Phys. Rev.*, 94(2):295–308, 1954.

[98] A. R. Hutson. Velocity analysis of thermionic emission from single-crystal tungsten. *Phys. Rev.*, 98(4):889–901, 1955.

[99] A. A. Brown, L. J. Neelands, and H. E. Farnsworth. Thermionic work function of the (100) face of a tungsten single crystal. *J. Appl. Phys.*, 21(1):1–4, 1950.

[100] M. H. Nichols. The thermionic constants of tungsten as a function of crystallographic direction. *Phys. Rev.*, 57:297–603, 1940.

[101] G. Haas and R. Thomas. Distribution of crystal orientation and work function in tungsten ribbons. *J. Appl. Phys.*, 40(10):3919–3924, 1969.

[102] J. Potter. Temperature dependence of the work function of tungsten from measurement of contact potentials by the Kelvin method. *Phys. Rev.*, 58:623–632, 1940.

[103] J. R. Werning. *Thermal ionization at hot metal surfaces.* PhD thesis, University of California, Berkeley, 1958.

[104] F. L. Reynolds. Ionization on tungsten single-crystal surfaces. *J. Chem. Phys.*, 39(4):1107–1114, 1963.

[105] L.N. Dobrezow. Electron and ion emission of thoriated wolfram in sodium vapor. *J. Exp. Theor. Phys.*, 17:301, 1947.

[106] H. Hotop. Detection of metastable atoms and molecules. In F.B. Dunning and R.G. Hulet, editors, *At. Mol. Opt. Phys. Atoms Mol. Vol. 29B*, chapter 11, pages 191–215. Academic Press, 1996.

[107] R. Carmina Monreal. Auger neutralization and ionization processes for charge exchange between slow noble gas atoms and solid surfaces. *Prog. Surf. Sci.*, 89(1):80–125, 2014.

[108] M.A. Cazalilla, N. Lorente, R. Diez Muno, J.P. Gauyacq, D. Teillet-Billy, and P.M. Echenique. Theory of Auger neutralization and deexcitation of slow ions at metal surfaces. *Phys. Rev. B*, 58(20):13991–14006, 1998.

[109] R. Cortenraad, A. W. Denier van der Gon, H. H. Brongersma, S. N. Ermolov, and V. G. Glebovsky. Work function dependent neutralization of low-energy noble gas ions. *Phys. Rev. B*, 65(19):195414, 2002.

[110] R N Varney. Metastable atoms and molecules. III. Metastable impacts on surfaces of various work functions. *Phys. Rev.*, 175:98–102, 1968.

[111] J. Roussel and C. Boiziau. Interaction of metastable thermal helium atoms with a surface. Observation of the creation of He+ ions. *J. Phys.*, 38(7):757–760, 1977.

[112] Y. Harada, S. Masuda, and H. Ozaki. Electron spectroscopy using metastable atoms as probes for solid surfaces. *Chem. Rev.*, 97(6):1897–1952, 1997.

[113] B. Auschwitz and K. Lacmann. The ionization of excited sodium atoms on a tungsten surface. *Chem. Phys. Lett.*, 113(2):9–12, 1985.

[114] N. N. Greenwood and A. Earnshaw. *Chemistry of the Elements*. Butterworth-Heinemann, 2nd edition, 1997.

[115] S. Hluchan and K. Pomerantz. Calcium and calcium alloys. In *Ullmann's Encycl. Ind. Chem.*, page 483. Wiley, 1st edition, 2006.

[116] Tony Oates. Lime and Limestone. In *Ullmann's Encycl. Ind. Chem.*, pages 1–32. Wiley-VCH Verlag GmbH & Co. KGaA, Weinheim, Germany, 7th edition, jun 2000.

[117] E. G.R. Ardagh, A. D. Barbour, G. E. McClellan, and E. W. McBride. Distillation of acetate of lime. *Ind. Eng. Chem.*, 16(11):1133–1139, 1924.

[118] N. Hinkley, J. A. Sherman, N. B. Phillips, M. Schioppo, N. D. Lemke, K. Beloy, M. Pizzocaro, C. W. Oates, and A. D. Ludlow. An atomic clock with 10ˆ-18 instability. *Science*, 341:1215, 2013.

[119] P. Lacovara, H. Choi, C. Wang, R. Aggarwal, and T. Fan. Room-temperature diode-pumped Yb: YAG laser. *Opt. Lett.*, 16(14):1089–1091, 1991.

[120] J. Emsley. The Elements. In *Oxford Chemsitry Guid.* Oxford University Press, New York, NY, 1995.

[121] *Handbook of chemistry and physics.* Chemical Rubber Company, Boca Raton, FL, 61st edition, 1981.

[122] K. J. Ross and B. Sonntag. High temperature metal atom beam sources. *Rev. Sci. Instrum.*, 66(9):4409–4433, 1995.

[123] S.-Z. Hu, Z.-H. Zhou, and B.E. Robertson. Consistent approaches to van der Waals radii for the metallic elements. *Z. Krist.*, 224(224):375–383, 2009.

[124] M. Miyabe, C. Geppert, M. Kato, M. Oba, I. Wakaida, K. Watanabe, and K. Wendt. Determination of ionization potential of calcium by high-resolution resonance ionization spectroscopy. *J. Phys. Soc. Japan*, 75(3):1–10, 2006.

[125] M. Aymar, A. Debarre, and O. Robaux. Highly excited levels of neutral ytterbium. II. Multichannel quantum defect analysis of odd- and even-parity spectra. *J. Phys. B At. Mol. Phys.*, 13(6):1089–1109, 1980.

[126] W. Meggers and J. Tech. The first spectrum of ytterbium (Yb I). *J. Res. Natl. Bur. Stand.*, 83(February 1978):13–70, 1978.

[127] Y. Takasu, K. Maki, K. Komori, T. Takano, K. Honda, and M. Kumakura. Spin-singlet Bose-Einstein condensation of two-electron atoms. *Phys. Rev. Lett.*, 91(4):040404, 2003.

[128] I. Sobelman, L. Vainshtein, and E. Yukov. *Excitation of atoms and broadening of spectral lines.* Springer-Verlag Berlin Heidelberg, 2nd edition, 1995.

[129] G. Herzberg. *Atomic spectra and atomic structure.* Dover Publications, New York, NY, 2nd edition, 1944.

[130] R. Hilborn. Einstein coefficients, cross sections, f-values, dipole moments, and all that. *Am. J. Phys.*, 50(11):982–986, 2005.

[131] R. Santra, K. Christ, and C. Greene. Properties of metastable alkaline-earth-metal atoms calculated using an accurate effective core potential. *Phys. Rev. A - At. Mol. Opt. Phys.*, 69(4):1–10, 2004.

[132] S. Porsev, A. Derevianko, and E. Fortson. Possibility of an optical clock using the 6 1S0 - 3P0 transition in 171, 173 Yb atoms held in an optical lattice. *Phys. Rev. A - At. Mol. Opt. Phys.*, 69(2):4, 2004.

[133] N. Beverini, F. Giammanco, E. Maccioni, F. Strumia, and G. Vissani. Measurement of the calcium 1P1-1D2 transition rate in a laser-cooled atomic beam. *J. Opt. Soc. Am.*, 6(11):2188–2193, 1989.

[134] J. Cho, H. Lee, S. Lee, J. Ahn, W. Lee, D. Yu, S. Lee, and C. Park. Optical repumping of triplet-P states enhances magneto-optical trapping of ytterbium atoms. *Phys. Rev. A - At. Mol. Opt. Phys.*, 85(3):4–7, 2012.

[135] S. Dörscher. *Creation of ytterbium quantum gases with a compact 2D-/3D-MOT setup.* PhD thesis, University of Hamburg, 2013.

[136] S. Porsev, Y. Rakhlina, and M. Kozlov. Electric-dipole amplitudes, lifetimes, and polarizabilities of the low-lying levels of atomic ytterbium. *Phys. Rev. A*, 60(4):2781–2785, 1999.

[137] T. Kurosu and F. Shimizu. Laser cooling and trapping of calcium and strontium. *Jpn. J. Appl. Phys.*, 29(11):L2127–L2129, 1990.

[138] L. Pasternack, D. M. Silver, D. R. Yarkony, and P. J Dagdigian. Experimental and theoretical study of the Ca I 4s3d 1D - 4s2 1S and 4s4p 3P1 - 4s2 1S forbidden transitions. *J. Phys. B At. Mol. Phys.*, 13:2231–2241, 1980.

[139] T. Loftus, J. R. Bochinski, and T. W. Mossberg. Magnetic trapping of ytterbium and the alkaline earths. *Phys. Rev. A*, 66:013411, 2002.

[140] C. Degenhardt, H. Stoehr, C. Lisdat, G. Wilpers, H. Schnatz, B. Lipphardt, T. Nazarova, P. Pottie, U. Sterr, J. Helmcke, and F. Riehle. Calcium op-

tical frequency standard with ultracold atoms: Approaching 10ˆ15 relative uncertainty. *Phys. Rev. A - At. Mol. Opt. Phys.*, 72(6):1–17, 2005.

[141] A. Kramida, Yu. Ralchenko, J. Reader, and NIST ASD Team. NIST Atomic Spectra Database (ver. 5.6.1), 2018.

[142] M. Pizzocaro, P. Thoumany, B. Rauf, F. Bregolin, and D. Calonico. Absolute frequency measurement of the 1S0 – 3P0 transition of 171 Yb. *Metrologia*, 54:102–112, 2017.

[143] J. L. L. Morgan, J. L. Skulan, G. W. Gordon, S. J. Romaniello, S. M. Smith, and A. D. Anbar. Rapidly assessing changes in bone mineral balance using natural stable calcium isotopes. *Proc. Natl. Acad. Sci.*, 109(25):9989–9994, 2012.

[144] P. B. Moser-Veillon, A. R. Mangels, N. E. Vieira, A. L. Yergey, K. Y. Patterson, A. D. Hill, and C. Veillon. Calcium fractional absorption and metabolism assessed using stable isotopes differ between postpartum and never pregnant women. *J. Nutr.*, 131(9):2295–2299, 2018.

[145] A. Dash, M. Pillai, and F. Knapp. Production of 177-Lu for targeted radionuclide therapy: available options. *Nucl. Med. Mol. Imaging (2010).*, 49(2):85–107, 2015.

[146] R. Bhardwaj, A. Van Der Meer, S. K. Das, M. De Bruin, J. Gascon, H. T. Wolterbeek, A. G. Denkova, and P. Serra-Crespo. Separation of nuclear

isomers for cancer therapeutic radionuclides based on nuclear decay aftereffects. *Sci. Rep.*, 7:1–8, 2017.

[147] F. Avignone, S. Elliott, and J. Engel. Double beta decay, Majorana neutrinos, and neutrino mass. *Rev. Mod. Phys.*, 80(2):481–516, 2008.

[148] Y. Iwata, N. Shimizu, T. Otsuka, Y. Utsuno, J. Menéndez, M. Honma, and T. Abe. Large-scale shell-model analysis of the neutrinoless $\beta\beta$ decay of Ca 48. *Phys. Rev. Lett.*, 116(11):1–6, 2016.

[149] A. Mollema. *Laser cooling, trapping and spectroscopy of calcium isotopes.* PhD thesis, University of Groningen, 2008.

[150] W.H. King. *Isotope shifts in atomic spectra.* Plenum Publishing Corporation, New York, NY, 1st edition, 1984.

[151] S. Svanberg. *Atomic and molecular spectroscopy. Basic aspects and practical applications.* Springer-Verlag Berlin Heidelberg, 3st edition, 2001.

[152] R. Senaratne, S. Rajagopal, Z. Geiger, K. Fujiwara, V. Lebedev, and D. Weld. Effusive atomic oven nozzle design using an aligned microcapillary array. *Rev. Sci. Instrum.*, 86(2), 2014.

[153] N. Ramsey. *Molecular beams.* Oxford University Press, 1st edition, 1956.

[154] H. C. W. Beijerinck and N. F. Verster. Velocity distribution and angular distribution of molecular beams from multichannel arrays. *J. Appl. Phys.*, 46(5):2083–2091, 1975.

[155] J. Giordmaine and T. Wang. Molecular beam formation by long parallel tubes. *J. Appl. Phys.*, 31(463), 1960.

[156] C. A. Flory and L. S. Cutler. Integral equation solution of low-pressure transport of gases in capillary tubes. *J. Appl. Phys.*, 73(4):1561–1569, 1993.

[157] D. Olander and V. Kruger. Molecular beam sources fabricated from multichannel arrays. III. The exit density problem. *J. Appl. Phys.*, 41(7):2769–2776, 1970.

[158] J. H. Moore, C. C. Davis, and M. A. Coplan. *Building scientific apparatus.* Cambridge University Press, 2nd edition, 1991.

[159] C. J. Bowers, D. Budker, E. D. Commins, D. DeMille, S. J. Freedman, A. T. Nguyen, S. Q. Shang, and M. Zolotorev. Experimental investigation of excited-state lifetimes in atomic ytterbium. *Phys. Rev. A - At. Mol. Opt. Phys.*, 53(5):3103–3109, 1996.

[160] N. Braithwaite. Introduction to gas discharges. *Plasma Sources Sci. Technol.*, 9:517–527, 2000.

[161] R. K. Marcus and J. A. C. Broekaert. Introduction. In R. K. Marcus and J. A. C. Broekaert, editors, *Glow Disch. plasmas Anal. Spectrosc.*, pages 1–14. John Wiley & Sons, Ltd, 2003.

[162] M. A. Lieberman and A. J. Lichtenberg. *Principles of plasma discharges and materials processing.* John Wiley & Sons, Inc., Hoboken, New Jersey, 2nd edition, 2005.

[163] A. Bogaerts, E. Neyts, R. Gijbels, and J. Van der Mullen. Gas discharge plasmas and their applications. *Spectrochim. Acta - Part B At. Spectrosc.*, 57(4):609–658, 2002.

[164] B. R. F. Kendall and E. Drubetsky. Starting delays in cold-cathode gauges at low pressures. *J. Vac. Sci. Technol. A Vacuum, Surfaces, Film.*, 14(3):1292–1296, 2002.

[165] S. Wissel, A. Zwicker, J. Ross, and S. Gershman. The use of dc glow discharges as undergraduate educational tools. *Am. J. Phys.*, 81(9):663–669, 2013.

[166] A. Bogaerts and R. Gijbels. Modeling of metastable argon atoms in a direct-current glow discharge. *Phys. Rev. A*, 52(5):3743–3751, 1995.

[167] R. Franklin. *Plasma phenomena in gas discharges.* Oxford University Press, 1st edition, 1976.

[168] G. Giusfredi, A. Godone, E. Bava, C. Novero, and E. Sava. Metastable atoms in a Mg beam: Excitation dynamics and velocity distribution. *J. Appl. Phys. J. Chem. Phys. Phys. Plasmas Rev. Sci. Instrum. J. Appl. Phys. Rev. Sci. Instrum*, 63(116):1279–164306, 1988.

[169] H. Griem. *Principles of plasma spectroscopy.* Cambridge University Press, 1st edition, 1997.

[170] R. D. Rundel, F. B. Dunning, and R. F. Stebbings. Velocity distributions in metastable atom beams produced by coaxial electron impact. *Rev. Sci. Instrum.*, 45(1):116–119, 1974.

[171] R. Freund and W. Klemperer. Molecular beam time-of-flight measurements for the study of metastable and repulsive electronic states. *J. Chem. Phys.*, 47(8):2897–2904, 1967.

[172] J. V. B. Gomide, G. A. Garcia, F. C. Cruz, A. J. Polaquini, M. P. Arruda, D. Pereira, and A. Scalabrin. Construction of an atomic beam system and efficient production of metastable states. *Brazilian J. Phys.*, 27(2):266–275, 1997.

[173] G. Giusfredi, P. Minguzzi, F. Strumia, and M. Tonelli. Atomic beam measurement of the lifetime of the 3P1 metastable states of Mg and Ca. *Z. Phys.*, 274:279–287, 1975.

[174] A. Fox. Effect of temperature on stress relaxation of several metallic materials. In E. Kula and V. Weiss, editors, *Residual Stress Stress Relax.*, pages 181–203. Springer US, Boston, MA, 1982.

[175] O. W. Richardson. The emission of electrons from tungsten at high temperatures: An experimental proof that the electric current in metals is carried by electrons. *Science*, 38(967):57–61, 1913.

[176] C. Lu and O. Lewis. Investigation of film-thickness determination by oscillating quartz resonators with large mass load. *J. Appl. Phys.*, 43(11):4385–

4390, 1972.

[177] J.G. Miller and D.J. Bolef. Acoustic wave analysis of the operation of quartz-crystal film-thickness monitors. *J. Appl. Phys.*, 39:5815, 1968.

[178] STM-2 USB Rate/Thickness Monitor Operating Manual, 2016.

[179] H.E. Bennett and J.O. Porteus. Relation between surface roughness and specular reflectance at normal incidence. *J. Opt. Soc. Amercia*, 51(2):123–129, 1961.

[180] C. D. Child. Discharge from hot CaO. *Phys. Rev. (Series I)*, 32:492–511, 1911.

[181] F. Kish and R. Fletcher. AlGaInP light-emitting diodes. In G. Stringfellow and M. George Craford, editors, *High Bright. Light Emit. diodes*, pages 149–226. Academic Press, Ltd., 1997.

[182] Xi. Lin, D. Liu, G. Lin, Q. Zhang, N. Gao, D. Zhao, R. Jia, Z. Zuo, and X. Xu. Periodic indentation patterns fabricated on AlGaInP light emitting diodes and their effects on light extraction. *RSC Adv.*, 4(108):63143–63146, 2014.

[183] AZoM. Aluminium Gallium Indium Phosphide (AlGaInP) Semiconductors, 2013.

[184] B. Saleh and M. Teich. *Fundamentals of Photonics.* John Wiley & Sons, Incorporated, 2nd edition, 2013.

[185] C. Wieman and L. Hollberg. Using diode lasers for atomic physics. *Rev. Sci. Instrum.*, 62:1–20, 1991.

[186] Ian Norris. *Laser cooling and trapping of neutral calcium atoms.* PhD thesis, University of Strathclyde, 2009.

[187] H. Talvitie, A. Pietiläinen, H. Ludvigsen, and E. Ikonen. Passive frequency and intensity stabilization of extended-cavity diode lasers. *Rev. Sci. Instrum.*, 68(1):1–7, 1997.

[188] C. J. Hawthorn, K. P. Weber, and R. E. Scholten. Littrow configuration tunable external cavity diode laser with fixed direction output beam. *Rev. Sci. Instrum.*, 72(12):4477–4479, 2001.

[189] S. Saliba, M. Junker, L. Turner, and R. Scholten. Mode stability of external cavity diode lasers. *Appl. Opt.*, 48(35):6692–700, 2009.

[190] S. Saliba and R. Scholten. Linewidths below 100 kHz with external cavity diode lasers. *Appl. Opt.*, 48(36):6961, 2009.

[191] C. Henry. Theory of linewidth of semiconductor lasers. *IEEE J Quantum Electron*, QE-18(2):259–264, 1982.

[192] H. Stoehr, F. Mensing, J. Helmcke, and U. Sterr. Diode laser with 1 Hz linewidth. *Opt. Lett.*, 31(6):736–738, 2006.

[193] G. Wysocki, R. F. Curl, F. K. Tittel, R. Maulini, J. M. Bulliard, and J. Faist. Widely tunable mode-hop free external cavity quantum cascade laser for

high resolution spectroscopic applications. *Appl. Phys. B Lasers Opt.*, 81(6):769–777, 2005.

[194] L. Ricci, M. Weidemüller, T. Esslinger, A. Hemmerich, C. Zimmermann, V. Vuletic, W. König, and T. W. Hänsch. A compact grating-stabilized diode laser system for atomic physics. *Opt. Commun.*, 117(5-6):541–549, 1995.

[195] A. S. Arnold, J. S. Wilson, and M. G. Boshier. A simple extended-cavity diode laser. *Rev. Sci. Instrum.*, 69(3):1236–1239, 1998.

[196] T. Hof, D. Fick, and H. Jänsch. Application of diode lasers as a spectroscopic tool at 670 nm. *Opt. Commun.*, 124(3):283–286, 1996.

[197] K. C. Harvey and C. J. Myatt. External-cavity diode laser using a grazing-incidence diffraction grating. *Opt. Lett.*, 16(12):910, 1991.

[198] E. Hecht. *Optics*. Addison-Wesley Publishing Company, Inc., 2nd edition, 1989.

[199] W. R. Trutna and L. F. Stokes. Continuously tuned external cavity semiconductor laser. *J. Light. Technol.*, 11(8):1279–1286, 1993.

[200] L. Levin. *Mode-hop-free electro-optically tuned diode laser*. PhD thesis, Lund University, 2002.

[201] H. Loh, Y. Lin, I. Teper, M. Cetina, Jo. Simon, J. Thompson, and V. Vuletić. Influence of grating parameters on the linewidths of external-cavity diode lasers. *Appl. Opt.*, 45(36):9191, 2006.

[202] G. Bjorklund. Frequency-modulation spectroscopy: a new method for measuring weak absorptions and dispersions. *Opt. Lett.*, 5(1):15–17, 1980.

[203] J. Rohe-Hansen and V. Helbig. Pressure broadening of the calcium 657 . 3 nm line by helium , neon and argon. *J. Phys. B At. Mol. Opt. Phys.*, 25:71–82, 1992.

[204] P. Kersten, F. Mensing, U. Sterr, and F. Riehle. A transportable optical calcium frequency standard. *Appl. Phys. B Lasers Opt.*, 68(1):27–38, 1999.

[205] J. Taylor, B. Hemingway, J. Hanssen, T. Swanson, and S. Peil. Vapor-cell frequency reference for short-wavelength transitions in neutral calcium. *J. Opt. Soc. Am. B*, 35(7):1557, 2018.

[206] C. Erickson, B. Neyenhuis, and D. Durfee. High-temperature calcium vapor cell for spectroscopy on the 4s2 1S0 - 4s4p 3P1 intercombination line. *Rev. Sci. Instrum.*, 76(12):1–5, 2005.

[207] M. Huang, M. Lu, and J. Shy. A calcium vapor cell for atomic spectroscopy. *Rev. Sci. Instrum.*, 73(11):3747, 2002.

[208] J. Bergquist. Doppler-free spectroscopy. In F. Dunning and R. Hulet, editors, *At. Mol. Opt. Phys. Atoms Mol. Vol. 29B*, chapter 13, pages 255–272. Academic Press, 1996.

[209] H. Metcalf and P. van der Straten. *Laser cooling and trapping.* Springer-Verlag New York, Inc., 1999.

[210] M. Copley and T. Phipps. The surface ionization of potassium on tungsten. *Phys. Rev.*, 48:960–968, 1935.